CHara ARray Integrated Optics Testbench (CHARIOT) for ultrafast laser written astrophotonic beam combiners

Master thesis

for obtaining the degree
Master of Science (M.Sc.)

Humboldt-Universität zu Berlin
Faculty of Mathematics and Natural Sciences
Department of Physics
AG Theoretische Optik & Photonik

in cooperation with
Leibniz-Institut für Astrophysik Potsdam (AIP)
&
Center for High Angular Resolution Astronomy (CHARA) Array
by Georgia State University (GSU)

submitted by Alyssa Valerie Mayer

primary examiner Prof. Dr. Kurt Busch
secondary examiner Dr. Aline N. Dinkelaker

date of submission 30th September 2024
last updated 22nd April 2025

Table of Contents

List of Figures

List of Tables

Abstract

Astrophotonic beam combiners for stellar interferometry offer significant advantages compared to free-space optics as they can reduce the size of astronomical instrument and increase its stability against vibrations and thermal effects. This thesis contributes to the development of CHARIOT (CHara ARray Integrated Optics Testbench), a future instrument designed to verify such components in laboratory- and on-sky tests at the CHARA Array. Two CHARIOT beam paths were precisely aligned to combine light from two telescopes in the array. For that, the Optical Path Difference (OPD) was corrected with an accuracy of $\sim 4.8\,\mathrm{mm}$, representing one-thousandth of the total beam path length of $\sim 5\,\mathrm{m}$. Laboratory tests demonstrated the ability to generate interference fringes with a calibration light source in the near-infrared using wavelength filters with different bandwidths in the astronomical K-band. In on-sky tests, CHARIOT's first fringes with starlight were achieved in May 2024. Before CHARIOT can be available to the interferometry community, further modifications are necessary, including plug-and-play interfaces and motorized mirrors. To enable future fabrication of astrophotonic beam combiners at the Leibniz Institute for Astrophysics in Potsdam (AIP), the initial parameter space for an Ultrafast Laser Inscription (ULI) system is explored. This technique is based on local refractive index changes produced by focusing a femtosecond laser into glass substrates. All experimental results revealed on-axis negative refractive index changes, which are surrounded by off-axis stress fields with positive refractive index change regions. Thus, in order to produce waveguides, different options must be explored, e.g. the utilization of the multiscan technique, writing in different materials or implementing beam shaping optics. Once a suitable parameter set is identified, the full process of design, fabrication, and characterization of ULI-written astrophotonic beam combiners can be carried out in-house at AIP and verified using the CHARIOT instrument in the future.

Zusammenfassung

In der stellaren Interferometrie bieten astrophotonische Strahlkombinierer im Vergleich zu Freistrahloptiken erhebliche Vorteile aufgrund ihrer Kompaktheit und Stabilität gegenüber Vibrationen und thermische Effekte. Die vorliegende Arbeit leistet einen Beitrag zur Entwicklung von CHARIOT (CHara ARray Integrated Optics Testbench), einem Instrument, das zukünftig zur Prüfung solcher Komponenten in Labor- und On-Sky-Tests eingesetzt werden soll. Zwei Strahlpfade von CHARIOT wurden präzise ausgerichtet um Licht von zwei Teleskopen zu überlagern. Dabei wurden optische Pfaddifferenzen (OPD) mit einer Genauigkeit von $\sim 4.8\,\mathrm{mm}$ ausgeglichen, was einem Tausendstel der gesamten Pfadlänge von $\sim 5\,\mathrm{m}$ entspricht. In Labortests konnte nahinfrarotes Licht im astronomischen K-band mit unterschiedlichen Bandbreiten durch die Nutzung verschiedener Filter interferiert werden. Das CHARIOT Instrument erzeugte im Mai 2024 zum ersten Mal Interferenzmessungen mit Sternenlicht. Damit CHARIOT der Interferometrie-Gemeinschaft zur Verfügung gestellt werden kann, sind weitere Modifikationen erforderlich. Dies beinhaltet zum Beispiel das Hinzufügen von Schnitstellen zum einfachen Austausch von astrophotonischen Komponenten sowie motorisierte Spiegel. Um zukünftig astrophotonische Strahlkombinierer am Leibniz-Institut für Astrophysik in Potsdam (AIP) herzustellen, umfasst ein weiterer Teil dieser Arbeit das experimentelle Untersuchen des Parameterraums für ein System zum Herstellen von Strahlkombinierern mit Ultrakurzpuls-Laserinskription (ULI). Diese Technik beruht auf lokalen Brechnungsindexänderungen durch das Fokussieren eines Femtosekundenlasers in Glassubstrate. Alle experimentellen Ergebnisse zeigten negative Brechungsindexänderungen im Laserfokus, die von Bereichen mit positiven Brechungsindexänderungen umgeben sind. Für die Herstellung von Wellenleitern müssen daher verschiedene Möglichkeiten erforscht werden. Diesbezüglich sind insbesondere das Schreiben von komplexen Strukturen mit mehreren Reihen und Ebenen, das Nutzen verschiedener Materialien sowie die Implementierung von Strahlformungsoptiken von Interesse. Sobald ein geeigneter Parametersatz identifiziert ist, kann der gesamte Prozess des Entwurfs, der Herstellung und der Charakterisierung von ULI-geschriebenen astrophotonischen Strahlkombinierern am AIP durchgeführt und mit dem zukünftigen CHARIOT-Instrument verifiziert werden.

1 Introduction

In modern astronomy, high angular resolution imaging of science targets is the key to studying astrophysical questions related to e.g. stellar dynamics, formation of planets or exoplanet detection. It is the prerequisite for resolving the smallest structures of those scientific targets in order to gain a comprehensive understanding of them. In general, sub-milliarcsecond (sub-mas) resolutions are required to investigate targets, such as the spotty surfaces of stars and protoplanetary disks, where the formation of planets occur. Even the largest telescopes do not have sufficient resolution for resolving these kinds of science targets. Single telescopes are limited by their aperture diameter. This limit can be overcome by combining several telescopes in an interferometric array. The angular resolution in interferometric arrays is determined by the distance between telescopes — called baseline — instead of the size of the individual telescopes. Thus, with larger baselines it is possible to achieve higher angular resolutions, which in turn allows resolving smaller structures of the investigated science targets. The longest optical direct interferometer in the world is the Center for High Angular Resolution Astronomy (CHARA) Array of the Georgia State University (GSU) located on Mount Wilson in California, USA. Here, the term "optical" means that beam redirection and combination is performed with optical components for wavelengths ranging from the visible to mid-infrared wavelength regimes. In the context of this thesis, near-infrared (NIR) wavelengths are discussed. The term "direct" describes the type of interferometric array where the starlight's electric fields from separated telescopes are directly interfered with each other. The image reconstruction via combination of different baselines is available generally for two types of beam combiners: free-space beam combiners using bulk optics and astrophotonic beam combiners, which are either fiber combiners or beam combiner chips with 2D or 3D structures. Free-space bulk optics beam combiners increase immensely in size when combining a large number of telescopes. Contrary to that, astrophotonic beam combiners are inherently small with footprints on the cm-scale, lightweight, and stable to vibrations and thermal effects. Thus, a range of different astrophotonic beam combiners are developed for the implementation in interferometric instruments. Fabricating astrophotonic beam combiner chips can be achieved with different methods. The best-established technique is photolithography, which can fabricate 2D structures. Having a beam combiner design limited to 2D results in many cross-overs, which leads to unwanted crosstalk between the waveguides. This can be avoided in 3D beam combiner designs. Ultrafast Laser Inscription (ULI) is a technique that allows the fabrication of 3D structures. In this technique, a femtosecond pulsed laser is focused into a glass substrate, which is translated in 3D to write waveguides. This technique relies on refractive index

changes due to nonlinear light-matter interactions and is not yet as established in the industry as photolithography. A reason for that is the large parameter space, which needs to be explored for each individual ULI system in order to find a suitable set of parameters for waveguide writing. At the Leibniz Institute for Astrophysics in Potsdam (AIP) a customized commercially available ULI system was procured in order to close the gap in the chain of developing astrophotonic beam combiners. So far, design and characterization of beam combiners could be completed at AIP, while fabrication was performed by project partners. In the future, design, fabrication with the ULI system and characterization is planned to be performed in house at AIP. This will allow faster iterative developments.

Another crucial part of developing novel astrophotonic beam combiners is performing laboratory and on-sky tests in real interferometric environments. The collaborative NAIR-2 / APREXIS project, undertaken by the AIP, the University of Cologne, the Heriot-Watt University, the Durham University, and the GSU CHARA Array, has resulted in the development of a new instrument: the CHara ARay Integrated Optics Testbench (CHARIOT). The CHARIOT instrument has two goals. Its initial goal is the verification of an achromatic fiber-connectorized K-band ULI-written beam combiner in on-sky tests as part of the NAIR-2 / APREXIS project. CHARIOT's long term goal is to establish a fully characterized 4-beam (nulling[1]) beam combiner instrument covering the J-, H-, and K-bands at the CHARA Array accessible for the worldwide interferometry community. Note that astronomical transmission bands are often used in the astronomy community to describe in which wavelength regime observations are performed. An overview of astronomical transmission bands in the visible and NIR is given in *Tab.* 1. Further information about these and other wavelength bands can be found in [2]. As part of the work for this thesis, it was possible to complete a two-month Erasmus+ internship from mid-October to mid-December in 2023 at the CHARA Array. During this internship, available components were utilized to complete the optical alignment of the 2-beam CHARIOT setup including fiber-coupling with a visible red laser. Another month-long research trip to the CHARA Array in April 2024 was partly funded by the Fizeau Exchange Visitors Program by the European Interferometry Initiative (Eii). The main tasks of this research trip were the alignment of a preliminary output optics subsystem including the implementation of a new science camera (C-RED One camera), accomplishing fiber-coupling with a NIR light source and the performance of laboratory and on-sky tests with the implemented beam combiner. Initial results of CHARIOT were

[1]Nulling interferometry enables observations of faint objects nearby bright stars, such as planets, by introducing a π phase shift in one of the incoming beams, and thus creating a dark "white light fringe" [1, 2]. It should be noted that one of CHARIOT's long-term objectives is to facilitate nulling interferometry. However, until this goal can be achieved, it is necessary to implement a series of other upgrades.

Table 1: Overview of astronomical transmission bands in the visible and NIR. Information about the bands central wavelength λ_c and bandwidth $\Delta\lambda$ given in this table can be found in [2]. The definition of *K'* depends on the specific wavelength filter and generally has a smaller bandwidth within the K-band. The values for *K'* are from the filter in [3].

Astronomical Transmission Band	Central Wavelength λ_c	Bandwidth $\Delta\lambda$
V	$0.55\,\mu$m	$0.09\,\mu$m
R	$0.70\,\mu$m	$0.22\,\mu$m
I	$0.9\,\mu$m	$0.24\,\mu$m
J	$1.25\,\mu$m	$0.30\,\mu$m
H	$1.65\,\mu$m	$0.35\,\mu$m
K'	$2.16\,\mu$m	$0.32\,\mu$m
K	$2.2\,\mu$m	$0.4\,\mu$m

presented and published during the SPIE Astronomical Telescopes + Instrumentation 2024 conference in Yokohama, Japan and can be found in [4, 5]. The work on CHARIOT, in particular the optical alignment of the 2-beam CHARIOT redirection subsystem and some laboratory tests are the scope of this thesis. Due to laser servicing, the work on the ULI system got delayed. Thus, solely the initial exploration of the parameter space for the ULI system at AIP was performed as part of this thesis. The two parts of this thesis can be viewed as bracketing the topic of astrophotonic beam combiners, as the work on CHARIOT will facilitate the testing of astrophotonic beam combiners in the future, while at AIP, ULI-written beam combiners will be designed, fabricated, and possibly verified with CHARIOT in the future. The work presented in this thesis serves as the foundation for both objectives.

The thesis is organized as follows: In *Ch.* 2, stellar interferometry is motivated by selected science targets showing the importance of high angular resolutions. Moreover, the principles of stellar interferometry are clarified through an explanation of Young's double-slit experiment. The mathematical description of stellar interferometry is fundamentally based on the van Cittert-Zernike theorem, which is explained with the aid of a number of illustrative examples. In addition, different types of beam combinations are discussed, as well as atmospheric turbulence effects and important parts of image reconstruction. The CHARA Array, its beam combiner instruments and usable alignment system is described in *Ch.* 3. One of the main parts of this thesis is discussed in *Ch.* 4, where the 4-beam CHARIOT setup is presented, the optical alignment of 2-beam setup explained as well as some of the performed laboratory and on-sky tests. An introduction to astrophotonics can be found in *Ch.* 5 together with a brief description of different astrophotonic beam combiner designs and an introduction to ULI. In *Ch.* 6, the ULI system at AIP is presented as well

as a parameter literature study, a brief description of phase contrast microscopy and the initial results of the parameter exploration of the ULI system at AIP. The most important conclusions and an outlook on possible future work is summarized in *Ch.* 7.

2 Stellar Interferometry

The passion of every scientist is to understand the unknown. Early astronomers solely had their eyes to observe the night sky. Since then, tools and techniques for astronomers advanced greatly. Telescope sizes have increased immensely, starting with the first small-diameter apertures over 10 m-class telescopes to perhaps the largest optical telescope ever built — the Extremely Large Telescope (ELT) with a planned diameter of $\sim 39\,\mathrm{m}$ [6]. Additionally, advances were made in space-based telescopes with the Hubble Space Telescope (HST) [7] and its successor, the James Webb Space Telescope (JWST) [8]. All of these advances have made it possible to unravel mysteries of the universe. However, the angular resolution of even the largest telescopes — including the future ELT — is not sufficient to resolve the spotty surfaces of stars. Imaging protoplanetary disks to understand planet formation is not possible with single telescopes due to their angular resolution, which is limited by the diameter of the telescope. Such scientific goals require angular resolutions in the sub-milliarcsecond (mas) range. With current technologies, these high angular resolutions can be achieved with interferometric solutions, where the angular resolution is determined by the distance between telescopes — known as the baseline — rather than the diameter of individual apertures.

In the optical and infrared wavelength range, there are several such interferometric arrays. The world's longest direct interferometer is the CHARA Array consisting of six 1 m telescopes with a maximum baseline of $B_{max} = 331\,\mathrm{m}$ [9, 10]. See *Ch.* 3 for more information about the CHARA Array. The European Southern Observatory's (ESO) Very Large Telescope Interferometer (VLTI) consists of four 8 m Unit Telescopes (UTs) and four 1.8 m diameter Auxiliary Telescopes (ATs) with maximum baselines of $B_{max}^{UTs} = 130\,\mathrm{m}$ and $B_{max}^{ATs} = 200\,\mathrm{m}$ respectively. The VLTI hosts different beam combination instruments, including GRAVITY [11, 12] in the K-band ($\lambda^K = 2.2\,\mu\mathrm{m}$) and PIONIER [13, 14] in the H-band ($\lambda^H = 1.65\,\mu\mathrm{m}$) (see *Ch.* 1 and *Tab.* 1 for information on astronomical transmission bands). In 2020, the Nobel Prize in Physics was awarded half to Roger Penrose and half to Reinhard Genzel and Andrea Ghez for the discovery of a supermassive black hole Sagittarius A* at the center of our galaxy. The VLTI GRAVITY integrated optics instrument provided parts of the data analyzed for their discovery.

In this chapter, the technique of stellar interferometry in the NIR wavelength regime[2] is motivated by highlighting selected scientific targets. Furthermore, the interferometric technique is explained, including the basic principle with Young's double-slit

[2] In the field of astronomy, it is standard practice to refrain from specifying the wavelength. Consequently, when discussing the optical, visible, or near- and mid-infrared, the corresponding wavelength regimes are implied instead of specific wavelengths.

experiment, the van Cittert-Zernike theorem, and examples of different intensity distributions of science targets and their related functions that can be measured with interferometric arrays.

2.1 Science Targets

Stellar interferometry with its mas-angular resolutions enables observations of objects that could not be investigated otherwise. Measuring stellar diameters and reconstructing stellar surfaces with sufficient angular resolution is an area of research that seeks to understand mass loss processes [15–17], stellar evolution [18–20], and magnetic starspots [21]. Other interesting objects to investigate are exoplanets, black holes, and the inner regions of circumstellar disks where the formation of planets occurs. In this context, the term "inner regions of circumstellar disk" refers to areas within the radius of 1 Astronomical Unit (AU), which is approximately equal to 1.5×10^{11} m and represents the distance between the Earth and the Sun [1]. In addition, exozodiacal dust, also known as exozodi, which are hot and warm dust disks around stars in planetary systems, can only be observed with interferometric techniques [22–25]. One of the reason to observe exozodis is to understand the evolution of comets and their out-gassing and mass-loss processes. Another reason is that exozodis are very bright, extended sources of light and therefore add photon noise in observations of faint targets. Thus, the exozodiacal light could interfere with future space-based observations of exoplanets even with coronagraphs [26] to block out the light from host stars [25]. Hence, understanding and observing exozodis is crucial for future exoplanet observations. The CHARA/FLUOR [27] and later JouFLU [28] instrument (see *Ch.* 4.1 for more information about the decommissioned instruments) observed exozodiacal dust for the first time and led the way for later observations done for example with the VLTI/PIONIER instrument [25]. A recent review of optical and infrared interferometry can be found in [29] where science targets as the above-mentioned are discussed among other topics.
One impressive example of the scientific results obtained from interferometric measurements is the imaging of the surfaces of stars as shown in *Fig.* 1. For the image reconstruction of the surface of the magnetically active ζ Andromedae (ζ And) [30], data was collected in 2013 during 14 nights with the CHARA/MIRC-X [31, 32] instrument (see *Ch.* 3.2). Comparing the reconstructed image from 2013 and 2011 showed changing starspots on the surface of ζ And. The strong magnetic fields of such stellar objects cause starspots and can change the atmospheric structure of the star, which obstruct measurements of the stellar's mass and age as explained in detail together with their observations in 2011 and 2013 in [30]. Thus, interferometric techniques can confirm polar starspots as accomplished in [30]. Another science

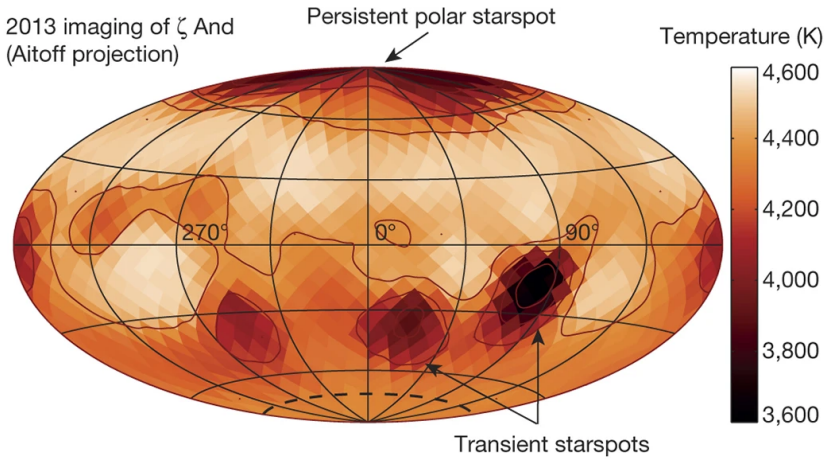

Figure 1: Reconstructed images of the surface of ζ Andromedae (ζ And) using data from 2013. Two starspots are marked as transient starspots after comparison to reconstructed images from 2011 of ζ And. Image is adapted and taken from [30].

target requiring high angular resolutions from interferometric arrays are protoplanetary disks — the birthing place of planets. An example of such a protoplanetary disk is found around the young Herbig Be star HD 190073 with possible evidence of a rotating sub-astronomical unit feature [33] shown in *Fig.* 2. The two images in *Fig.* 2 were taken in two epochs with a time period of 32 days between them and show a sub-astronomical unit feature rotating by 27° within that timespan. These images were obtained by combining data from two interferometric arrays — the CHARA Array using the MIRC-X [31, 32] and the VLTI using the PIONIER [13, 14] beam combiner instrument. By combining data from both interferometric arrays, it was possible to observe small and large scale structures around the young Herbig Be star HD 190073. Studying the inner regions of protoplanetary disks enables observations of processes not yet fully understood, including the interaction between the star and its surrounding dust, magnetic fields and the formation of new planets [33]. The observation of such small structures is only possible with the use of interferometric arrays, as the angular resolution of individual telescopes is inherently limited by their size. The differences between single aperture and telescope array observations will now be explained in the following section.

2.2 Principles of Stellar Interferometry

In this chapter, the principles of stellar interferometry are explained. Furthermore, the angular resolutions of single telescopes and interferometric arrays are compared and an explanation of the underlying concept is given by comparing stellar interferometry to Young's double slit experiment. These concepts and a description of the interferometric technique can be found in a variety of textbooks such as [1, 2, 34–39].

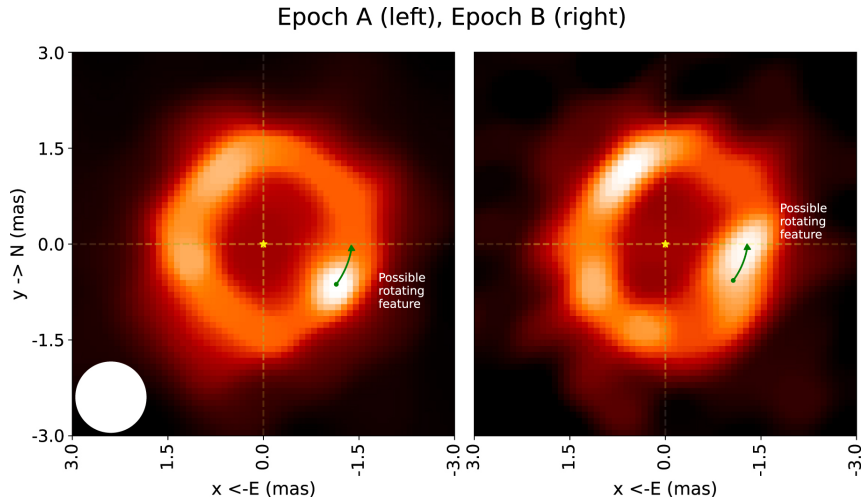

Figure 2: The protoplanetary disk, more specifically the inner region (within 1 AU) of the young Herbig Be star HD 190073, is reconstructed for two epochs using both the CHARA/MIRC-X [31, 32] and the VLTI/PIONIER [13, 14] instrument presented in [33]. In the center of both images, the star's position is depicted with a yellow asterisk, which is surrounded by a ring-like dust structure. A time period of 32 days passed between the measurement epochs A and B, in which this sub-astronomical unit feature moved by 27°. A white circle on the bottom left of the image of epoch A symbolizes the effective angular resolution of the CHARA Array, which is $\lambda/2B_{\mathrm{max}} = 0.55\,\mathrm{mas}$ in the H-band for a maximum baseline of $B_{\mathrm{max}} = 330\,\mathrm{m}$ [33]. The image is taken from [33].

As described in *Ch.* 2.1, high angular resolutions are crucial for investigating small structures of astronomical objects. According to classic diffraction theory, the diffraction-limited angular resolution is given by the Rayleigh criterion, which describes the distance at which two point sources are just resolvable. Hence, the angular resolution of a single telescope θ_{tel} is

$$\theta_{\mathrm{tel}} = 1.22\frac{\lambda}{D} \approx \frac{\lambda}{D}\,, \tag{1}$$

where λ is the observed central wavelength and D is the diameter of the telescope. Thus, for reaching mas in the H- and K-band a telescope diameter of several hundred meters is required [1, 34]. Such diameters are not feasible for single telescopes due to increasing costs, but also for physical reasons such as their weight and the loss of pointing ability with larger telescope diameters, even with segmented mirrors. Therefore, by introducing an interferometric approach, the angular resolution is not dependent on the individual telescope's diameter but their distance called baseline. Analogously to the angular resolution described in *Eq.* 1, the angular resolution of an interferometric array θ_{int} at which two equally bright stars are just resolvable can

be described by

$$\theta_{\text{int}} = \frac{\lambda}{2B} \approx \frac{\lambda}{B}\,, \tag{2}$$

where again λ is the observed central wavelength and B the baseline — or distance between telescopes [1, 34]. Hence, by combining two telescopes interferometrically, a virtual telescope with an aperture the size of the separation between both telescopes is achieved. Thus, with baselines of several hundred meters as it is possible with the CHARA Array and the VLTI, mas-resolutions are achievable for observing the above-mentioned science cases. Note that, for this thesis the approximated equations are used for all given angular diameters omitting the factors 1.22 and 1/2 when not otherwise stated. This is done for easier comparison as some telescopes and interferometric arrays either use the equations with or without the factors.
The principle of stellar interferometry can be described and understood by comparing its concept to Young's double slit experiment — originally executed with two pinholes in 1803 [1, 2]. A stellar interferometer measures the coherence function (complex visibility) of the science target, which can be related to its brightness distribution via the van Cittert-Zernike theorem (see *Ch.* 2.3). This relationship is similarly found in Young's double slit experiment, where light (electromagnetic plane waves) from a distant coherent point source illuminates a screen with two slits. At the slits, the light is diffracted and creates constructive and destructive interference. The resulting interference fringe pattern is then observed at a screen placed behind the slits, which shows an alternating bright and dark intensity distribution. A schematic of the experiment is shown in *Fig.* 3, where the fringe pattern of the double slit is depicted as a solid red line, and the envelope of the single slit diffraction pattern is visualized as a dotted line in the same plot. Here, the increase in angular resolution when going from a single slit to two slits separated by a distance is clearly shown. Now comparing Young's double slit experiment with stellar interferometry, the two slits are replaced by two light collecting apertures separated by the baseline. For stellar interferometry, the light sources are extended and incoherent, but at a great distance. This leads to approximately plane waves and partial coherence at the position of the telescopes. Depending on the telescope separation, the light source is either fully unresolved or partly resolved. A fully unresolved science target can be described as a coherent point source, as it is the case in Young's double slit experiment. Such coherent point sources create a fringe contrast of unity. The fringe contrast is known as the Michelson fringe visibility $V_{\text{Michelson}}$ given by

$$V_{\text{Michelson}} = \frac{I_{\text{max}} - I_{\text{min}}}{I_{\text{max}} + I_{\text{min}}}\,, \tag{3}$$

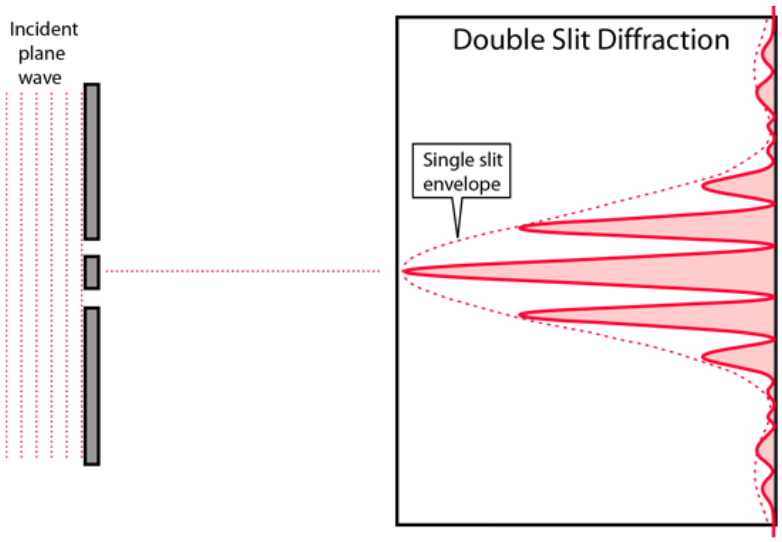

Figure 3: In this image, Young's double slit experiment is depicted. Plane waves illuminate a screen with two slits where the light is diffracted and forms constructive and destructive interference. Alternating bright and dark intensity variations known as a fringe pattern can be viewed on a second screen behind the double slit. Here, the double slit diffraction is shown as a plot as a solid red line whereas the envelope of the single slit diffraction is visualized as a dotted red line. Image is taken from [40]. Image Credit: HyperPhysics by Rod Nave, Georgia State University.

where $I_{\max}$ is the maximum value of the fringe intensity distribution and $I_{\min}$ is the minimum [34]. As mentioned above, for a fully coherent source, the Michelson fringe visibility is 1, while for an incoherent (fully resolved) light source, no fringes occur at all and the fringe visibility is 0. Hence, the Michelson fringe visibility gives values between $0 \leq V_{\text{Michelson}} \leq 1$. Values in between describe sources with partial coherence.

In stellar interferometry, the interference fringes for different baselines are measured, which include amplitude (fringe contrast) and phase information. The fringe contrast and phase changes with different baseline lengths. This is because larger sized features are already resolved for shorter baselines, while small features require longer baselines. As previously stated, the degree of coherence (incoherent, partial and full coherence) is associated with the ability to resolve these features. These measurements form the basis for stellar interferometry and allow the reconstruction of the brightness distribution of the science target. A mathematical description of the relationship between measured data and the physical properties of science target is given by the van Cittert-Zernike theorem (see *Ch.* 2.3.)

The basic principle of a stellar interferometer is shown in *Fig.* 4. As explained during the comparison with Young's double slit experiment, for stellar interferometry starlight from at least two telescopes separated by a baseline B is combined. In reality, the effective baseline B_{eff} is the correct value for the respective baseline,

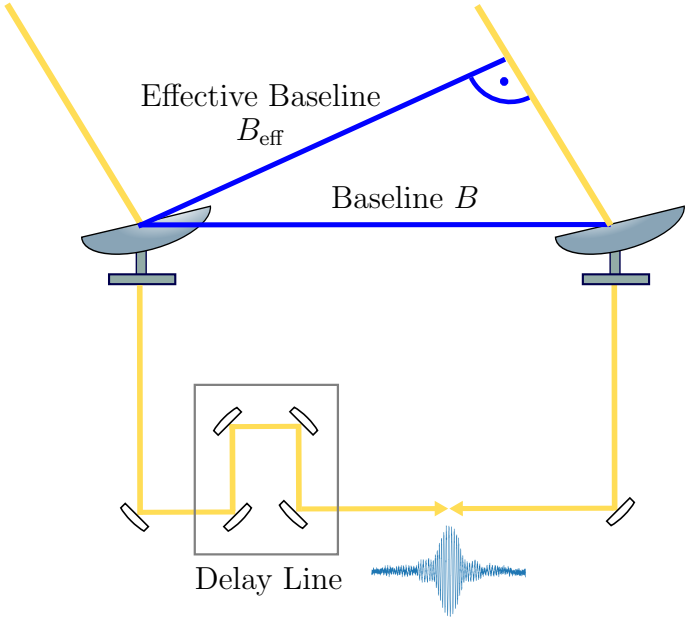

Figure 4: In this image, the basic principle of stellar interferometry is depicted. Similar to Young's double slit experiment, two telescopes or apertures collect light from a distant light source (e.g. a star). The distance between two telescopes is called baseline B. Note that in reality, the effective Baseline B_{eff} is the value needed for image reconstruction and determination of the angular resolution. During on-sky observations the effective baseline changes due to the Earth's rotation and with that the pointing angle of the telescopes. For simplicity reasons, the baseline B is used to derive the angular resolution in the context of this thesis. Once the starlight is collected, the path lengths have to be matched within the coherence length l_{coh} in order to be able to generate fringes. OPD correction is usually done with optical delay lines consisting of mirrors on movable platforms / translation stages. The beam combination is shown symbolically as two arrows facing each other where light would be combined. See *Ch.* 2.4 for different methods of beam combination. The fringe pattern example in this image is a real temporal fringe pattern measured at the CHARA Array with the 2-beam CHARIOT (see *Ch.* 4) and the STS (see *Ch.* 3.3.2) as a light source.

as gives the exact separation between the telescopes with respect to the incoming plane waves. The effective baselines B_{eff} varies during on-sky observations due to the Earth's rotation. Thus, for simplicity, the fixed baseline (distance between telescopes) B is used for all equations including the angular resolution and later for the measured visibility. In order to achieve interference fringes, the geometric delay also known as the Optical Path Difference (OPD) needs to be compensated within the coherence length l_{coh} described by

$$l_{\text{coh}} = \frac{\lambda^2}{\Delta\lambda}\,, \tag{4}$$

where λ is the central wavelength and $\Delta\lambda$ the bandwidth of the observed starlight [36]. Usually, the coherence length is only a fraction of the wavelength for the NIR regime. Hence, for interferometric arrays such as the VLTI and the CHARA Array, very precise delay lines are required in order to compensate the OPD to the required precision before the beams are combined to achieve fringes.
Similar to Young's experiment, the angular resolution is determined by the baselines utilized during the measurements. For better understanding and to provide examples, the angular resolutions and baselines for the H- and K-band instruments at CHARA and the VLTI are compared to the future ELT capabilities as well as to the Event Horizon Telescope (EHT) in *Fig.* 5. Note that the EHT is a radio telescope roughly the size of the Earth [41, 42]. Even though this radio interferometric array utilizes a different technique to combine light from greatly separated apertures and has different fundamental properties due to the longer wavelength, radio interferometry is a well-established field that has strongly influenced modern stellar interferometry in the optical and infrared with its great successes. The values for these facilities are summarized in *Tab.* 2. So far, solely the concept and basic principles of stellar interferometry were described. In the next part, the van Cittert-Zernike theorem will be described as a mathematical description of stellar interferometry.

2.3 Van Cittert-Zernike Theorem

At the core of the mathematical description of stellar interferometry lies the van Cittert-Zernike theorem describing the connection between the intensity distribution of the science target in the object plane to the measurable coherent flux in the baseline plane as a Fourier transform [2, 29, 34–37, 39]. For more detailed mathematical description of the van Cittert-Zernike theorem, please refer to [34–37, 39]. The so-called object plane and baseline plane are used to define coordinate systems, while their connection is described through the van Cittert-Zernike theorem. The coordinate systems are shown in *Fig.* 6. For describing the science target,

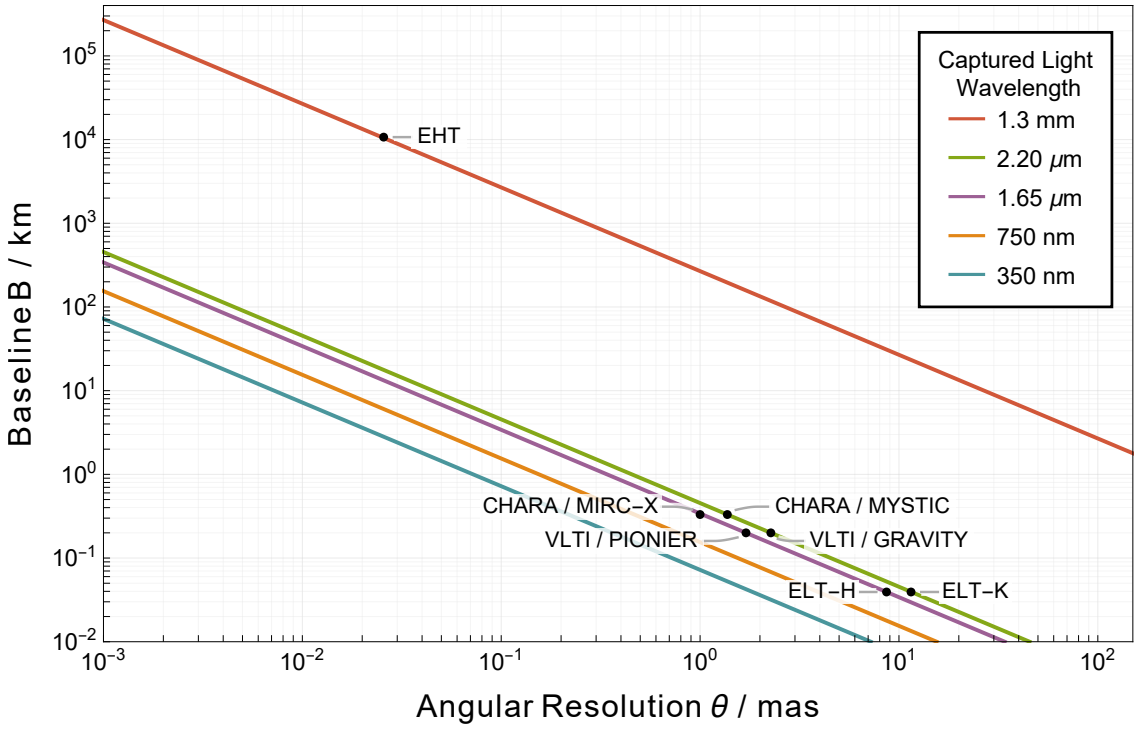

Figure 5: In this plot, the required baseline length for specific angular resolutions is depicted using the simplified equations in *Eqs.* 1 and 2. Included in this plot are lines in blue at 350 nm and orange at 750 nm to show the connection between baseline and angular resolution for visible wavelength. Further, the central wavelength of the H-band is shown in purple and the K-band in green. Another line in the radio regime is shown in red for a wavelength of 1.33 mm. Radio interferometry has relaxed requirements due to the longer wavelength, e.g. the coherence length is on the order of cm than on the order of nm – μm as is the case for optical and NIR wavelengths. Furthermore, in this plot the maximum baselines and highest achievable angular resolutions are marked for the CHARA MIRC-X and MYSTIC instruments, the VLTI PIONIER and GRAVITY instruments using the ATs, as well as the EHT, and the future ELT. The central wavelengths, maximum baselines and angular resolutions shown in this image are summarized in *Tab.* 2.

Table 2: An overview of the state-of-the-art interferometers and telescopes is summarized. Specifically, the maximum baselines and highest achievable angular resolutions are given for the EHT radio interferometer array and for the H- and K-band beam combiners instruments at the VLTI and CHARA. Furthermore, the maximum planned telescope diameter and highest expected angular resolutions in the H- and K-band is included for the future ELT (marked with a *), which is not commissioned yet. The angular resolution values are calculated with simplified versions of *Eqs.* 1 and 2 are used. The results are also depicted in *Fig.* 5.

Interferometer or Telescope	Wavelength λ	Maximum Baseline B or Diameter D	Angular Resolution θ_{int} or θ_{tel}
EHT [41, 42]	$\lambda = 1.3\,\text{mm}$	$B = 10700\,\text{km}$	$\theta_{\text{int}} = 25.6\,\mu\text{as}$
CHARA/MIRC-X [31, 32]	$\lambda = 1.65\,\mu\text{m}$	$B = 331\,\text{m}$	$\theta_{\text{int}} = 1.0\,\text{mas}$
CHARA/MYSTIC [43, 44]	$\lambda = 2.2\,\mu\text{m}$	$B = 331\,\text{m}$	$\theta_{\text{int}} = 1.4\,\text{mas}$
VLTI/PIONIER [13]	$\lambda = 1.65\,\mu\text{m}$	$B_{ATs} = 200\,\text{m}$ $B_{UTs} = 130\,\text{m}$	$\theta_{\text{int}}^{ATs} = 1.7\,\text{mas}$ $\theta_{\text{int}}^{UTs} = 2.6\,\text{mas}$
VLTI/GRAVITY [12, 45]	$\lambda = 2.2\,\mu\text{m}$	$B_{ATs} = 200\,\text{m}$ $B_{UTs} = 130\,\text{m}$	$\theta_{\text{int}}^{ATs} = 2.3\,\text{mas}$ $\theta_{\text{int}}^{UTs} = 3.5\,\text{mas}$
ELT* [6]	$\lambda^H = 1.65\,\mu\text{m}$ $\lambda^K = 2.2\,\mu\text{m}$	$D = 39.3\,\text{m}$	$\theta_{\text{tel}}^H = 8.7\,\text{mas}$ $\theta_{\text{tel}}^K = 11.5\,\text{mas}$

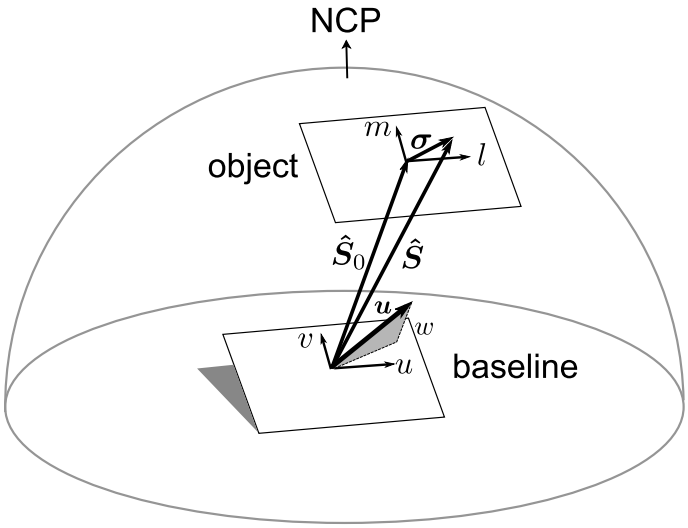

Figure 6: Coordinate system for describing the van Cittert-Zernike theorem. Due to the large distance between the science case in the object plane and the interferometric array in the baseline plane, it is sufficient to omit the z-component of both the object vector $\vec{\sigma} \equiv \boldsymbol{\sigma} = (l, m, n) \approx (l, m)$ and the baseline vector $\vec{u} \equiv \boldsymbol{u} \approx (u, v)$. The vectors $\hat{\boldsymbol{S}}_{\mathbf{0}}$ and $\hat{\boldsymbol{S}}$ connect the center of the baseline coordinate system to the center of the object plane as well as to the object vector $\vec{\sigma}$ respectively. Note that the component m is directed towards the North Celestial Pole (NCP). The image is taken from [34].

an object's brightness distribution $I(\vec{\sigma})$ is introduced in the coordinate system of the object $\vec{\sigma} = (l, m, n)$. Furthermore, to describe the function measurable with an interferometric array, the so-called coherent flux $F(\vec{u})$ is defined in the baseline coordinate system [34]. Note that the baseline vector is given in units of wavelength $\vec{u} = (u, v, w) = \frac{\vec{B}}{\lambda}$, where λ is the observed wavelength and $\vec{B}$ the baseline vector in the baseline plane. Compared to the large distance between baseline and object plane, the relatively small z-components of both vectors can be omitted for simplicity. Thus, by projecting the vectors into two-dimensional vectors within their coordinate system, the baseline and object planes are parallel to each other. Both planes are connected in their center via the vector $\hat{\boldsymbol{S}}_{\boldsymbol{0}}$ whereas the vector $\hat{\boldsymbol{S}}$ connects the center of the baseline plane to the object's vector position $\vec{\sigma}$ [34]. Now that the coordinate systems are well-defined, the van Cittert-Zernike theorem relates the so-called complex visibility given by

$$\mathcal{V}(\vec{u}) = \frac{\iint_{-\infty}^{+\infty} I(\vec{\sigma}) e^{-2\pi i \vec{\sigma}\vec{u}}\, dl\, dm}{\iint_{-\infty}^{+\infty} I(\vec{\sigma})\, dl\, dm} \tag{5}$$

$$\mathcal{V}(\vec{u}) = \frac{F(\vec{u}, \nu)}{F(\vec{0}, \nu)} \tag{6}$$

to the intensity distribution $I(\vec{\sigma})$ of a distant incoherent source via a Fourier transform [34]. Note that the complex visibility $\mathcal{V}$ is simply the coherent flux normalized by the object's intensity and is measurable with an interferometric array. Further, the complex visibility $\mathcal{V} = |\mathcal{V}|e^{i\phi}$ consists of the phase ϕ and the absolute value of the complex visibility. The latter is the amplitude $|\mathcal{V}| = V_{\text{Michelson}}$ of the complex visibility and known as the Michelson visibility (see *Eq.* 3) or fringe contrast [29, 34]. Measuring not only the amplitude or fringe contrast of the complex visibility, but also the phase is crucial for correlating intensity information to its position in the object's intensity distribution [29]. The van Cittert-Zernike theorem describes a distant incoherent scientific target as many point sources emitting sine waves that are incoherent with each other near the scientific target. Over large travel distances — as it is the case for stellar interferometry — the resulting wavefront is a superposition of all those light emitting point sources [29, 34, 36, 37]. Thus, the formation of partial coherence is often described by a mutual coherence function, which is also known as the "complex degree of coherence". The mutual coherence function is simply the normalized cross-correlation of two electric fields measured at two points in space-time. For further discussion of the mutual coherence function, please refer to [37]. Hence, an interferometric array is a tool of measuring the degree of partial coherence at two points in space-time.

In practice, by measuring the interference fringes (amplitude or fringe contrast and phase) for various baselines in the baseline or (u, v)-plane, the coherence function or

Table 3: Summary of selected objects' intensity distributions $I(\vec{\sigma})$ in the object plane and their corresponding complex visibility functions $\mathcal{V}(\vec{u})$ in the baseline plane analogous to the discussions presented in [34, 38]. θ_d describes the angular diameter of the star in case of a uniform disk whereas θ_d is the FWHM in case of a Gaussian intensity distribution of the observed science case.

Object Shape	Intensity Distribution $I(\vec{\sigma})$	Complex Visibility $\mathcal{V}(\vec{u})$
Point Source	$\delta(\vec{\sigma} - \vec{\sigma_0})$	$e^{2\pi i \vec{u}\vec{\sigma_0}}$
Uniform Disk	$\mathrm{rect}(\lvert\vec{\sigma}\rvert/\theta_d)$	$\frac{2J_1(\pi\lvert\vec{u}\rvert\theta_d)}{\pi\lvert\vec{u}\rvert\theta_d}$
Gaussian	$e^{-4\ln 2\lvert\vec{\sigma}\rvert^2/\theta_d^2}$	$e^{-\frac{(\pi\lvert\vec{u}\rvert\theta_d)^2}{4\ln 2}}$

complex visibility (both are related by a normalization factor) can be reconstructed. Once, this function is known for a sufficient amount of baselines or points in the (u, v)-plane, the intensity distribution of the science target can be derived by an inverse Fourier transformation [34–36, 39]. This explains the principle of image reconstruction in an ideal way. In reality atmospheric turbulences as well as other noise sources and a sparsely filled (u, v)-plane complicate the image reconstruction. Therefore, a detailed explanation of this part of stellar interferometry is not in the scope of this thesis.

Nevertheless, selected examples are discussed below to understand the relationship between the intensity distribution of a stellar object in the object plane and the measurable visibility function with an interferometric array in the baseline plane. Analogous to discussions presented in [34, 38], the intensity and visibility functions for point sources, uniform disks and Gaussian distributions are discussed in the following (see *Tab.* 3 and *Fig.* 7). In *Tab.* 3, the intensity distributions $I(\vec{\sigma})$ as a function of the object vector $\vec{\sigma}$ as well as their corresponding complex visibility $\mathcal{V}(\vec{u})$ depending on the baseline vector $\vec{u}$ are summarized. For the uniform disk shape, θ_d describes the angular diameter, while for a Gaussian shape θ_d is the Full Width at Half Maximum (FWHM) of the Gaussian intensity distribution of the observed science target. The object's intensity distributions are depicted in *Fig.* 7 (top) for a point source, two sizes of uniform disks to explain the angular diameter dependency of the visibility function and on example of a Gaussian disk. In *Fig.* 7 (bottom), the complex visibilities corresponding to the examples for the intensity distributions are shown in a plot in the same colors. In *Fig.* 7, the first example denoted in green is a point source. Its intensity distribution is a delta function and is symbolized as a dot. When taking the Fourier transform of a delta function, the resulting visibility function is unity for all baselines (see *Fig.* 7 (bottom)). Hence, the source is completely unresolved and fully coherent. In reality, stellar objects are extended sources

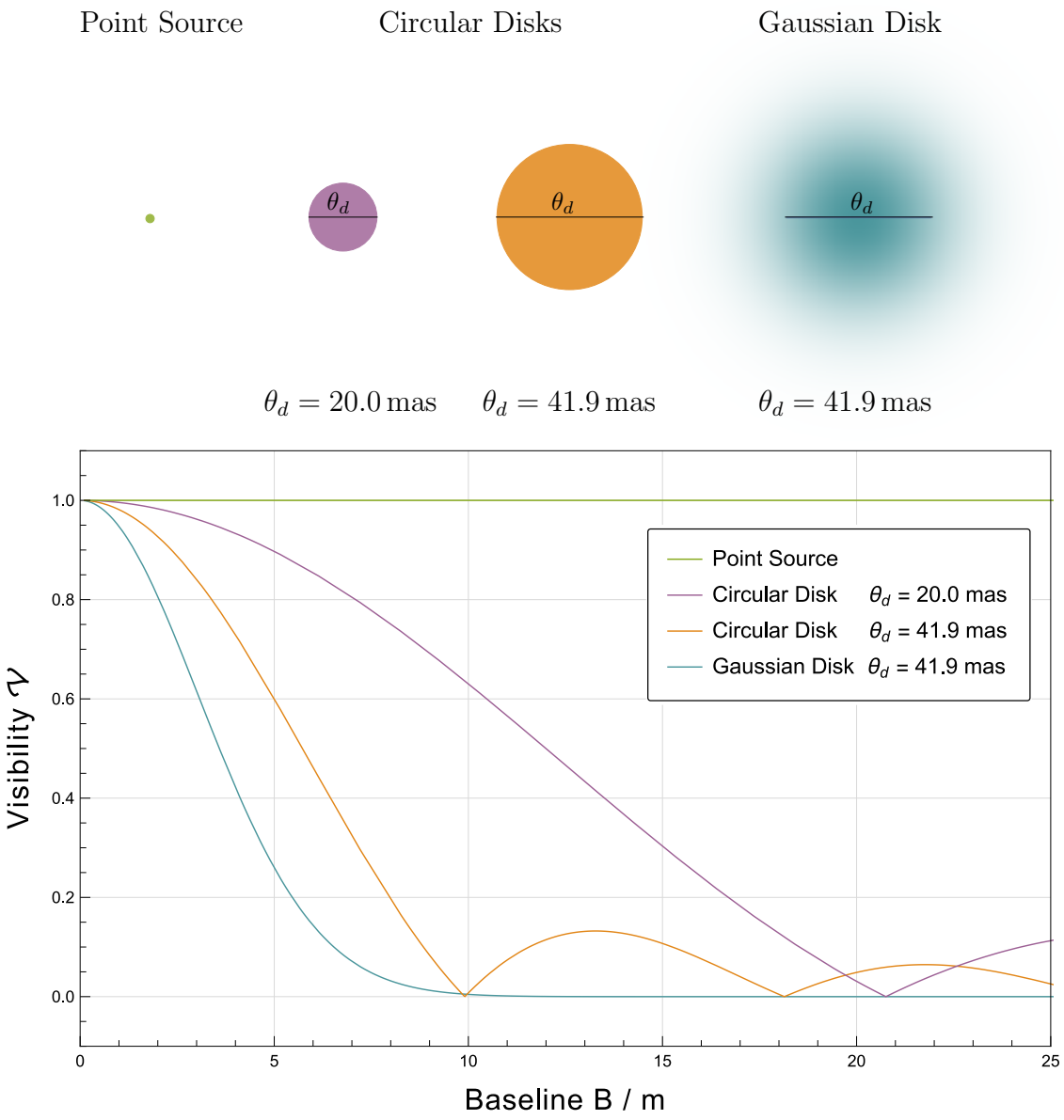

Figure 7: The intensity distributions for a point source, two sizes of uniform disks to show the angular diameter dependency as well as a Gaussian shape are depicted at the top. The functions for both intensity distributions at the top of the image, and the baseline dependent visibility functions are summarized in *Tab.* 3. In green, a point source is depicted as a dot, which results into a unity visibility function for all baselines. A point source is unresolved and thereby fully coherent. In reality, stellar objects are extended sources and can be described by different models, for example as uniform or Gaussian disks. Two uniform disks are shown as uniformly bright circular disks with different angular diameter in purple and orange. The angular diameter θ_d dependence is clearly visible, where sources with larger angular diameter result in a decrease of visibility at shorter baselines as they require shorter baselines to become resolved. Lastly, a blue Gaussian shape is depicted for the intensity distribution, which is a Gaussian visibility function as stated in the van Cittert-Zernike theorem. The angular diameter θ_d in this case is defined as the FWHM. Note that the baseline vector is defined as $\vec{u} = \vec{B}/\lambda$ and the wavelength used for this image is the central wavelength of the H-band $\lambda^H = 1.65\,\mu\mathrm{m}$.

and one possibility to describe such an object is by using a uniformly bright disk with sharp edges. This circular disk intensity distribution is depicted in *Fig.* 7 by a purple and orange circular shape with an angular diameter of $\theta_d = 20.0\,\text{mas}$ and $\theta_d = 41.9\,\text{mas}$ respectively. The latter value is chosen deliberately as it is the angular diameter of Betelgeuse (α Orionis, HD 39801). The value for the angular diameter of $\theta_d^{\text{Betelgeuse}} = (41.9 \pm 0.06)\,\text{mas}$ is an adopted value from several measurements given as it appears in [46]. Betelgeuse is a red supergiant whose core is predicted to collapse into a supernova at the end of its life. It also received immense public interest due to its great dimming in 2019/2020 [47]. Furthermore, Betelgeuse's angular diameter was the first to be measured by an optical interferometer. About 100 years ago, in 1921, Michelson and Pease placed a $20\,\text{feet} \approx 6.1\,\text{m}$ baseline interferometer on top of the 100-inch Hooker telescope on Mt. Wilson where the CHARA Array is located as well [48]. Michelson and Pease measured the angular diameter of Betelgeuse at its first zero-crossing for an effective wavelength of $\lambda = 575\,\text{nm}$ and a baseline of $B = 121\,\text{in} \approx 3\,\text{m}$ [48]. By assuming a uniform disk and applying $\Delta\theta = 1.22 \cdot \frac{\lambda}{B}$, the resulting angular diameter was measured to be $\Delta\theta = 47\,\text{mas}$ with an uncertainty of 10% [48], which is close to today's measured wavelength dependent angular diameters of Betelgeuse. By comparing Betelgeuse's relatively large angular diameter to a smaller example almost half as large, it is clearly visible that for larger angular diameters θ_d the visibility functions decreases faster with increasing baseline. Here in this plot, the absolute value of the true baseline vector $|\vec{B}|$ is used for the x-axis instead of the baseline vector in terms of wavelength $\vec{u} = \vec{B}/\lambda$. For *Fig.* 7, the central wavelength of the H-band $\lambda^H = 1.65\,\mu\text{m}$ is used. Generally for uniform disks, the first zero crossing allows to calculate the diameter of the observed science target whereas the visibility function values for larger baselines inherit information about smaller structures within the shape (e.g. starspots) as well as limb-darkening. The latter effect describes the apparent decrease in intensity from the center to the edge (or "limb") of a star's spherical surface [35]. Furthermore, the purple visibility function for the smaller angular diameter is closer to unity for longer baselines than it is for larger angular diameters. Hence, the smaller uniform disk is more coherent for longer baselines than it is the case for the larger angular diameter uniform disk. Lastly, a Gaussian intensity distribution is depicted in blue in *Fig.* 7. When applying a Fourier transformation to a Gaussian intensity distribution, the result is again a Gaussian distribution. In this case, the angular diameter θ_d describes the FWHM of the Gaussian intensity distribution, which was chosen to be equal to the diameter of the orange circular disk making it overall the largest presented science target, and thus, the fastest decreasing visibility function with increasing baseline. Besides the presented examples, there are several other objects and corresponding shapes and models discussed in literature and used for parameter extraction and

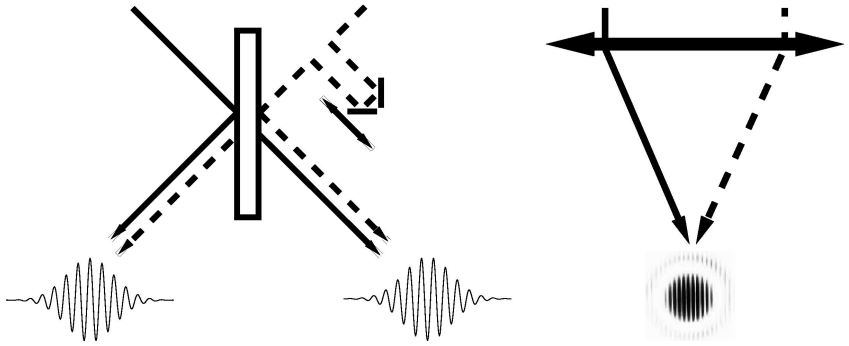

Figure 8: Left: Co-axial beam combination also known as pupil plane beam combination can be achieved for example by overlapping light in a beam-splitter. This results in two beams with temporally encoded fringes. For this type of beam combination, the path in one arm needs to be varied within the coherence length of the light, while the time-dependent intensity fringes are measured [1, 34, 38].
Right: Multi-axial beam combination can be referred to as image plane beam combination and generates spatial fringes. In this case, the fringes are formed directly on the detector itself and are spatially encoded. Image taken from [38].

image reconstruction. A few to mention are limb darkened circular disk, binary stars or ring like structures (see [34, 38] for more examples).
With the foundation of the van Cittert-Zernike theorem discussed, the following chapter will introduce another fundamental aspect of stellar interferometry: interferometric beam combination.

2.4 Interferometric Beam Combination

This chapter discusses different types of beam combination and explains frequently used terminology. The main focus is the beam combination that results in the interferometric fringe pattern, from which amplitude and phase information of the complex visibility of the science signal can be extracted. Mainly two types can be distinguished, which are shown in *Fig.* 8. The left illustration in *Fig.* 8 is referred to as **co-axial** or **pupil plane** beam combination. Here, the two combined beams result in two time-dependent fringes (temporal fringes) [1, 34, 38]. For this type of beam combination bulk-optics beam-splitters can be utilized as well as photonic beam combination solutions. Photonic solutions are e.g. fiber beam-splitters and chip-based Integrated-Optic (IO) circuits where light propagates in waveguides as it is implemented in the beam combiner in the CHARIOT (see *Ch.* 4.5). Other photonic beam combiner types are presented in *Ch.* 5.2. For pupil plane beam combination, the variation of the path length of one of the incoming beams within the coherence length is crucial. Only by applying this modulation, time-dependent intensity variations can be detected, thus creating temporal fringes as depicted in *Fig.* 8 on the left.

The depiction on the right in *Fig.* 8 illustrates the principle of **multi-axial** or **image plane** beam combination. In this case, two incoming beams are directly combined on a screen or camera generating spatial fringes. For image plane beam combination no additional modulation is required as a spatial modulation is inherent to the method. Along the image plane, the path delay between both incoming beams is different, and hence, spatially-dependent fringes are generated. This type of beam combination with spatial fringes is similar to the previously explained comparison between Young's double slit experiment and stellar interferometry [1, 34, 38].
Besides the above stated names for both types of beam combinations, sometimes the terms "Michelson" and "Fizeau" combinations are used for pupil and image plane combination, respectively. This can lead to confusion as Michelson used "Fizeau" combination in his interferometry experiments but the "Michelson" method was named after the Michelson-Morley experiment [1]. Therefore, this terminology will not be used within this thesis and is only mentioned for the sake of completeness.
When combining more than two telescopes, there are different adaptations for pupil and image plane beam combination:

- For **image plane** beam combination, the addition of more telescopes is not restricted as long as the spacing between the beams focusing on the detector is non-redundant — meaning there is no equal spacing, and thus, all spatial frequencies are different [1].

- **Pupil plane** beam combination on the other hand can be adapted by either using **pairwise** or **All-In-One (AIO)** beam combination.

  - **Pairwise** beam combinations means the light is equally split so that it can be interfered with each of the other telescopes individually. This allows measuring the temporal fringes for all baselines but decreases the signal significantly for interferometric arrays with numerous telescopes.

  - **AIO** beam combination is somewhat similar to the adaptation for image plane beam combination. Here, the incoming signals are modulated temporally in order to ensure different temporal fringe frequencies for all combinations in the interferometric array [1].

A more in depth description of different beam combination types can be found in [35] in addition to the other textbooks already mentioned in this chapter. Another way to distinguish beam combination instruments is to state if **free-space** or **IO** are used to accomplish beam combination.
Free-space beam combination is mostly achieved with bulk optics and refers to beam propagation in which the beams are not confined [34]. This solution usually takes up a lot of space, especially for a larger number of telescopes that have to be combined.

Hence, integrated-optics solutions are more often being tested and implemented into beam combination instruments nowadays. For these photonic-based solutions, light propagates confined in waveguides such as fibers or integrated-optics chips [34]. An overview of such photonic beam combination solutions is given in *Ch.* 5.2. Photonic solutions reduce the required size for beam combination on an optical table and usually can have a higher stability with respect to changes in temperature or vibrations, which may otherwise introduce noise and path differences. However, they can suffer from cross-coupling and throughput losses, and thus improving these properties is the focus of current research.
An advantage of photonic beam combination is spatial filtering and the reduction of the effect of atmospheric turbulences on the beam (phase differences across the beam). This is due to the coupling into single-mode fibers or waveguides, as was successfully performed with the now decommissioned FLUOR instrument [49]. In addition, interferometric beam combination can be used at a different part of the instrument, namely for fringe tracking. This is briefly explained along with other methods to reduce atmospheric turbulence in the signal in *Ch.* 2.5. This is a crucial part of image reconstruction, for which (u, v)-plane coverage, number of telescopes and closure phases are introduced in *Ch.* 2.6. Due to the complexity of image reconstruction and atmospheric turbulence compensation, both topics are intended as brief introductions rather than full descriptions, but references to textbooks will be provided. In the following section, an introduction to the effects of atmospheric turbulences and techniques for overcoming them is provided.

2.5 Atmospheric Effects

Ground-based stellar interferometry suffers from atmospheric turbulence effects, which can be experienced in form of stars twinkling. In *Fig.* 9 the effect of Earth's atmosphere is visualized. From a distant star, plane wavefronts (surfaces with constant phase) arriving at the Earth are disturbed by turbulences in the Earth's atmosphere. In this process random phase fluctuations are introduced by turbulences when light propagates through sections with variations in air density and changing refractive indices [1, 29, 34]. Optical turbulences occur in areas where air with temperature differences is perturbed [34]. A statistical description of atmospheric turbulences was derived by Kolmogorov in 1941 and is known as Kolmogorov turbulences theory [34]. An important measure for atmospheric coherence length (often referred to as "seeing" condition), is called the Fried parameter r_0, which is used to describe conditions during on-sky observations in interferometric arrays. The Fried parameter r_0 is wavelength dependent and gives a theoretical diameter of an aperture over which diffraction limited observations can be performed. Thus, for telescope diam-

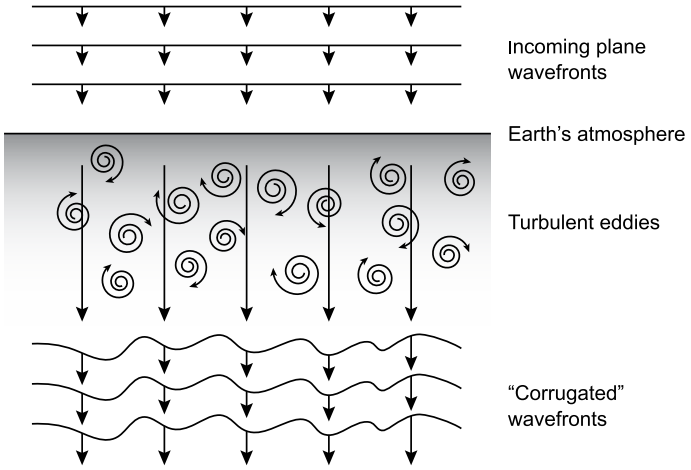

Figure 9: Visualizing wavefront disturbances introduced by atmospheric turbulences. The incoming plane wavefronts (surfaces with constant phase) from a distant star is distorted by turbulences in the Earth's atmosphere leading to unwanted phase variations, which corrupt interferometric measurements and must be corrected before signals can be combined [1, 29, 34]. The image is taken from [34].

eters D larger than r_0, i.e. $D > r_0$, the observations are restricted by atmospheric turbulences, and hence, limited by "seeing" instead of diffraction properties [1, 34]. Usually, for interferometric arrays in locations with very good "seeing" conditions — little atmospheric fluctuations — the Fried parameter is roughly 10 cm to 20 cm in the visible and around 1 m in the NIR [29, 34]. The wavelength dependency of the Fried parameter is roughly $r_0 \propto \lambda^{6/5}$, and thus the Fried parameter (and therefore the "seeing" conditions) increases for larger wavelengths [1, 39]. Thus radio interferometry is less effected by atmospheric turbulence effects than observations in the infrared or visible.

In order to correct for atmospheric disturbances of the incoming wavefronts, different methods are implemented in interferometric arrays. The methods of Adaptive Optics (AO), fringe tracking (the AO of interferometry) and spatial filtering through coupling in single-mode fibers will be briefly discussed in the following. An explanation of those methods can be found in [34, 39]. AO systems can be implemented for each telescope in an interferometric array and consist of wavefront sensors measuring fluctuations in the incoming wavefronts, which are corrected afterwards either by tip-tilt mirrors or more precisely in higher orders with deformable mirrors. Deformable mirrors consist of small actuators, which can change the form of the mirror's surface in order to compensate for the previously measured wavefront distortions, and thus, actively correct wavefront corrugations caused by atmospheric turbulences [34]. A review on AO in stellar interferometry can be found in [50]. In the case of faint science targets, the target itself cannot be used to measure corrugations in the incoming wavefront. Therefore, either a nearby bright star is required (close to the faint science target) or a laser guide star can be utilized enabling a

larger sky coverage [50]. Another way to reduce atmospheric turbulences is the coupling of the observed starlight into single-mode fibers, which spatially filters the signal and passively corrects for atmospheric turbulences [34]. Note that tip-tilt corrections are required for efficient coupling of starlight into fibers. Similar results can be achieved in free-space setups if the light is focused through a pinhole and collimated afterwards. A disadvantage of this method is the loss of all spatial components not focused into the single-mode fiber (or through the pinhole) leading to a reduced sensitivity. See [51] for detailed discussions on the topic of fiber-coupling efficiency in astronomical instruments. As mentioned above, the pioneering work of the FLUOR instrument utilized this passive spatial filtering to reduce atmospheric turbulences while achieving visibility measurements with high precision [49]. Due to the changes in the effective path length, atmospheric turbulences can introduce fringe jitter, which describes random phase errors or changes in the position of the white-light fringe — the center of the fringe packet at zero path delay. This effect is also known as "piston error". In interferometric measurements, when averaging over signals which are corrupted by fringe jitter, a loss of visibility contrast is experienced. Usually, AO do not compensate this fringe jitter completely, hence, both AO and fringe trackers are used in interferometric arrays. A fringe tracker can take advantage of unused wavebands by tracking the location of the white-light fringe and measuring OPD fluctuations. These measurements are sent to the delay lines of the interferometric array to compensate for fringe jitter during on-sky observations with the science beam combiner [1, 34]. Fringe tracking is often performed simultaneously with science measurements in a waveband not used in the science beam combiner. An example for that is the combined MIRC-X J- and H-band and MYSTIC K-band beam-combination and fringe-tracking instrument at the CHARA Array (see *Ch.* 3.2.2). Note that in the case of the MIRC-X/MYSTIC instrument, either MIRC-X or MYSTIC is used as the science combiner, while the other is used as the fringe tracker, or vice versa.
Achieving visibility measurements with high sensitivity by reducing atmospheric turbulence effects included in the incoming signals is crucial for image reconstruction. Due to the complexity of the field of image reconstruction, solely a few selected aspects are presented in the following.

2.6 Image Reconstruction

For image reconstruction, the measurement of the complex visibility including amplitude and phase information of a science target is crucial in order to perform an inverse Fourier transformation. The complex and large field of image reconstruction is not to be fully discussed in this thesis and more details can be found in

textbooks such as [1, 34]. Examples of reconstructed images from interferometric measurements are shown in *Figs.* 1 and 2. In this chapter, only a few aspects of image reconstruction are discussed briefly. One of those aspects is the closure phase, which is the sum of three phases in a closed triangle made up of three telescopes in an interferometric array. The relative phase differences between two telescopes can be measured as $\phi_{i,j} = \phi_0^{i,j} + (\varphi_j - \varphi_i)$ for $i \neq j$, where $\phi_0^{i,j}$ is the phase from the science target and φ the phase due to atmospheric turbulences above each telescope [1, 34]. Thus, the closure phase within a triangle spanned by three telescopes is insensitive to telescope-specific atmospheric turbulences, since the pairwise phase measurements each contribute a positive and negative phase deviation term, which cancels out in the summing process for the closure phase. Closure phases are important for image reconstruction, and hence, at least three telescopes are required in an interferometric array to achieve closure phase measurements for image reconstruction. The number of non-redundant (or independent — no two equal) closure phases in an interferometric array with N telescopes is $\frac{1}{2}(N-1)(N-2)$ [1, 34]. Another important aspect of image reconstruction is filling the (u, v)-plane (or baseline plane) measuring the complex visibility for as many non-redundant baselines as feasible. In reality, it is not possible to fill the (u, v)-plane completely, but with a larger amount of telescopes in an interferometric array, it is possible to achieve measurements for a larger number of baselines simultaneously. For an interferometric array with N telescopes, it is possible to measure $\frac{1}{2}N(N-1)$ non-redundant baselines simultaneously, assuming the telescopes within the array are adequately placed [1, 34]. By utilizing the varied effective baseline B_{eff} due to the Earth's rotation, it is possible to acquire more visibility measurements and further fill the (u, v)-plane, which is critical for image reconstruction. Similar to using the rotation of the Earth, using a larger number of wavelengths increase the (u, v)-plane filling. This completes the brief presentation of the selected aspects of image reconstruction. Further information on this topic can be found in [1, 34].

This concludes the chapter on stellar interferometry, in which the technique of stellar interferometry was motivated and explained by comparing it to the well-know Youngs's double-slit experiment. Afterwards, the van Cittert-Zernike theorem was discussed with selected examples as a more mathematical description. Different beam combination techniques were introduced and techniques presented to overcome atmospheric turbulence effects as well as a brief introduction to image reconstruction. In this chapter, the CHARA Array was shortly mentioned and is focus of the next chapter before the work on CHARIOT is discussed in *Ch.* 4.

3 Center for High Angular Resolution Astronomy (CHARA) Array

A main part of the work for this thesis consists of the setup and alignment of a beam combiner testbench at the CHARA Array, which is the longest direct interferometer array in the world, located on Mount Wilson, USA. This chapter will provide a description of the telescope array, an overview of the beam combiner instruments, as well as the available alignment system that can be used for all instruments.

3.1 The CHARA Array

The CHARA Array is the longest interferometer in the world with baselines ranging from $B_{min} = 34\,\text{m}$ up to $B_{max} = 331\,\text{m}$ operating in the optical and NIR [9, 10]. The interferometric array consists of six 1 m telescopes located on Mount Wilson in California in a non-redundant Y-shape with two telescopes in each arm of the configuration (see *Fig.* 10). When all six telescopes are combined, 15 non-redundant baselines and 10 closure phases are created (see *Ch.* 2.6 for a description of non-redundant baselines and closure phases). A detailed description of the CHARA Array including the telescopes, vacuum tubes for beam transportation, optical delay lines as well as beam reducing and combination setups can be found in [9] and on the CHARA website [10]. In *Fig.* 10, the six telescopes "S1", "S2", "E1", "E2", "W1", and "W2" in the Y-configuration are shown together with the L-shaped CHARA Beam Synthesis Facility (BSF). A crucial part of stellar interferometry is the compensation of OPD between all telescopes from the science target to the point of beam combination (see *Ch.* 2). At the CHARA Array this is achieved in two parts. A constant delay can be compensated with the insertion of mirrors in the vacuum tubes known as the Pipes of Pan (PoPs). These are fixed at various locations in the vacuum pipes at 0 m, 36.6 m, 37.2 m, 109.7 m and 143.1 m [9]. After that, the optical delay of the beams is continuously compensated in the Optical Path Length Equalizer (OPLE) on precisely moving delay lines. The OPLE accounts for the Earth's rotation during observations. Once the OPD is compensated, the beam size is reduced from 12.5 cm to 1.99 cm with a Beam Reducing Telescope (BRT) followed by a Beam Sampling System (BSS) [9]. The BSS splits the incoming light into visible and infrared wavelengths using dichroic mirrors on movable translation stages. The CHARA lab accommodates six beam paths, $B1$ to $B6$, which are redirected to different beam combination instruments in the Beam Combination Laboratory (BCL). The incoming six beams paths $B1$ to $B6$ in the BCL are independent of the six telescopes in the CHARA Array. This means that it is possible to select which telescope within the CHARA Array is assigned to which of the six beam

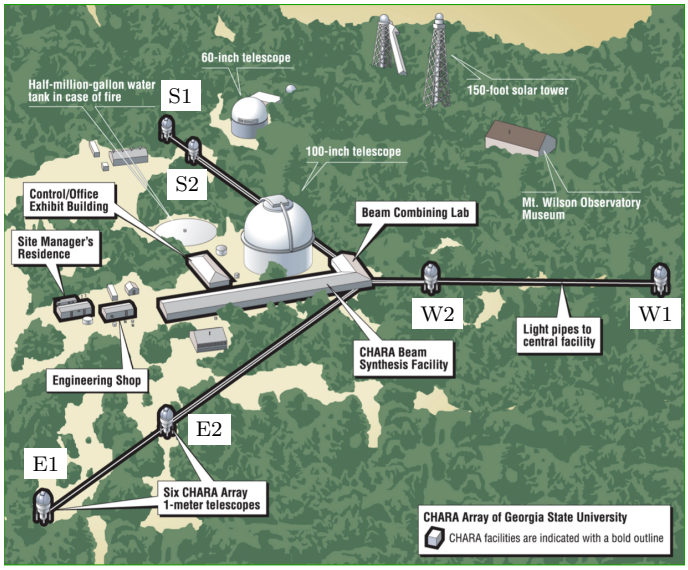

Figure 10: The GSU CHARA Array is the longest direct interferometer in the world with a maximum baseline of $B_{max} = 331\,\mathrm{m}$ operating in the optical and NIR [9, 10]. It consists of six 1 m telescopes. The light from each telescope is transported in vacuum tubes to the CHARA BSF where the optical delay is compensated. The beams are combined in various instruments in the BCL. Image taken from the CHARA website [10] with additional labels for the telescope names "S1", "S2", "E1", "E2", "W1", and "W2". Image credit: The Observatories of the Carnegie Institution.

paths $B1$ to $B6$ in the BCL. For each telescope, there is a beam redirection setup on a translational stage, which can be moved into one of the six beam paths $B1$ to $B6$. Hence, enabling the use of suitable telescope combinations and baseline lengths according to specific science goals. If not all beams are used in one beam combination instrument, it is possible to use another instrument in parallel. Afterwards, the beam is transported to the BCL where the beam combination instruments are located. The currently used beam combination instruments are shortly described in *Ch.* 3.2. Note that at the entrance of the BCL, the beams $B1$ to $B6$ have an OPD of $11.2" = 28.45\,\mathrm{cm}$ between two consecutive beams as described in more detail in *Tab.* 7 and in *Ch.* 4.3. This is due to the different locations of the beam distribution mirrors before the BCL, which match the telescopes to the beams $B1$ to $B6$ after the delay lines. More specifically, the delay lines compensate all OPD up to this point, and the telescope-to-beam matching introduces a new constant delay of $11.2" = 28.45\,\mathrm{cm}$ between two consecutive beams. Thus, all beam combiner instruments in the BCL must compensate this constant OPD. The laboratory light sources at CHARA also take into account the constant OPD to ensure that all telescope beams and light sources are aligned, allowing easy switching between all light sources. See *Ch.* 3.3 for a description of the lab light sources utilized for alignment and lab tests with the beam combiner instruments, which are presented in the following part.

3.2 Beam Combination Instruments

This chapter aims to provide insight into the capabilities of the CHARA Array and context with respect to beam combination schemes. For this purpose, the main beam combiner instruments currently in use will be described. For a complete list that includes decommissioned instruments, see the CHARA website [10]. An exception is the CHARIOT instrument, which is the main topic of this thesis and described in *Ch.* 4 in detail. The science community can apply for observations nights during which the beam combiner instruments can be used. During those on-sky observations, CHARA staff and operators ensure a smoothly working interferometric array. Other nights are reserved for maintenance or engineering work on instruments.

3.2.1 CLASSIC & CLIMB

As the name suggests, the CLASSIC beam combiner instrument combines beams in a very classic way — with free-space bulk optics in the pupil plane. Due to its simplicity, CLASSIC is the initial two-beam combiner at CHARA with which first science was accomplished [52]. A three beam expansion for closure phase measurements is achieved with the CLassic Interferometry with Multiple Baselines (CLIMB) [52]. Both CLASSIC & CLIMB are instruments optimized for high sensitivity measurements resulting in the dimmest observable science targets with magnitudes of K'-mag = 9.3 and H-mag = 9.7 under very good seeing conditions. The K'-band is a transmission band with smaller bandwidth within the K-band. An example for a K'-filter transmission curve is given in *Tab.* 1. Routinely for both K'-band and H-band, CLASSIC combines light from science targets of magnitude 8.5. More information about the CLASSIC & CLIMB instruments can be found in [52]. See also [53] for information on the CLASSIC data reduction software and [54] for a mathematical description of the data reduction. CLASSIC/CLIMB is now being superseded by the new SILMARIL instrument.

3.2.2 MIRC-X/MYSTIC

The world's highest angular resolution imaging instrument in the NIR is the MIRC-X (Michigan InfraRed Combiner-eXeter) upgrade of the initial MIRC (Michigan InfraRed Combiner) instrument. MIRC-X is a six telescope single-mode fiber image plane beam combiner for precision visibility and closure phase measurements operating in the J- and H-bands achieving a magnitude of H-mag = 8.2 under optimal conditions [31]. MIRC-X is open to the interferometric community since mid-2017 and aims to observe various science targets such stellar surfaces and starspots, exoplanets, young stellar objects and planet formation process [31]. Part of the MIRC-X upgrade was the extension to cover the J-band as well and the installation of a very

low-noise sub-electron detector (C-RED One camera) [31, 32]. Such a science camera was recently implemented into the CHARIOT setup and is briefly introduced in *Ch.* 4.4.4.

The Michigan Young Star Imager at CHARA (MYSTIC) instrument, funded by the U.S. National Science Foundation, is located on the same optical table as MIRC-X. MYSTIC is a K-band two-mode beam combiner instrument [43, 44]. One operating mode is the six-telescope AIO single-mode fiber image plane combiner based on the MIRC-X design including photometric measurements (operational scince July 2021) [43, 44]. The second mode is the four-telescope pairwise (ABCD) photonic integrated circuit, which is operational since May 2022. It utilizes a spare GRAVITY chip as implemented in the VLTI-GRAVITY instrument. See *Ch.* 5.2.2 for a description of the GRAVITY chip as an explanation of pairwise ABCD beam combination. With the AIO mode and best-case conditions, science targets as dim as K-mag = 7.7 are observable. MYSTIC is cryogenically cooled to an operating temperature of 220 K and it utilizes a C-RED One camera with low-noise properties. The instrument aims to study mainly planet formation processes in the inner astronomical-unit regions of young stellar objects [43, 44].

Both MIRC-X and MYSTIC share not only the same optical bench, but also the same control software. On advantage of this is the control software's ability to cophase the MIRC-X and MYSTIC instrument for simultaneous fringe-tracking and imaging [31, 43]. Together, MIRC-X/MYSTIC are used to achieve a highly sampled (u, v)-plane [43].

3.2.3 PAVO

A beam combiner instrument in the visible wavelength range at CHARA is the Precision Astronomical Visible Observations (PAVO) instrument [55]. PAVO is a three beam spectrally-dispersed pupil plane beam combiner with an integrated field-unit, in the R-band and I-bands (see *Tab.* 1 in *Ch.* 1). To date, the data reduction pipeline is fully established solely for single baselines, and therefore, no closure-phase measurements were achieved so far. Nonetheless, PAVO is optimized for sensitivity in the visible and allows observations of science targets as faint as R-mag = 7.1 [55].

3.2.4 SPICA

The Stellar Parameters and Images with a Cophased Array (SPICA) instrument is a new six telescope low spectral resolution ($R = 140$ in the visible) single-mode fiber beam combiner in the visible wavelength range [56, 57]. Beside the low spectral

resolution mode, SPICA can operate in a medium ($R \sim 3000$) a high ($R \sim 10000$) spectral resolution mode [57]. Part of the SPICA instrument is a fringe tracker (SPICA-FT) in the H-band implemented in the MIRC-X instrument [58]. It utilizes a six telescope beam ABCD pairwise integrated optics beam combiner inspired by the VLTI/GRAVITY fringe tracker [58]. The installation started at the end of 2021 / beginning of 2022 [10, 57]. SPICA's purpose is to have an extensive study of fundamental parameters of science targets, especially the measurements of diameters of stars utilizing both visible beam combination and infrared fringe tracking [56, 57]. The SPICA instrument is located and based on the decommissioned Visible spEctroGraph and polArimeter (VEGA) instrument [59]. Limiting magnitude for SPICA is expected to be roughly R-mag $\simeq 8$ for measuring the angular diameter of a science target and R-mag $\simeq 4\,\text{to}\,5$ for imaging science targets in the visible wavelength regime [56].

3.2.5 SILMARIL

SILMARIL is a 2 $\times$ three-telescopes beam combiner optimized for throughput efficiency, which has been installed in the beginning of 2023. It operates simultaneous in the H- and K-band [60]. SILMARIL's priority is low losses and high sensitivity (rather than high spectral resolution), with the goal of observing the faintest targets such as active galactic nuclei, dim young stellar objects and binary stars [61]. The instrument's capabilities are expected to enable measurements of science targets as faint as H- and K-mag $\gtrsim 10$. For that, SILMARIL utilizes a minimum of free-space optics instead of fiber-based or integrated optics to reduce coupling losses and an image plane design for the setup together with a low-noise C-RED One camera [60, 61].

3.3 Alignment System

An important part of the CHARA Array is the beam alignment system which is co-aligned with the incoming telescope beams. For the alignment, a white light source and a green laser can be used, as well as a newly implemented Six Telescope Simulator (STS) for alignment and lab tests [9]. Furthermore, a red laser source for back-injection or attached to the STS was used during the alignment process. An overview of the light sources and their models and makes is given in *Tab.* 4. In this chapter, the green CHARA laser and some of its functionalities as well as the STS will be discussed in detail as they were used during the work on CHARIOT (see *Ch.* 4). Further, the CHARA Array has a Six Telescope Star Tracker (STST), which helps tracking the star during on-sky observations. A short description of the STST can be found in [43]. The STST is not further discussed in this thesis and

Table 4: Summary of the models and makes of various light sources available in the CHARA lab. Note that for the STS Halogen lamp a Thorlabs LMA-PM-10 PCF fiber was connectorized by ALPhANOV.

Light Source	Make	Model
White Light Source	Newport	6263
Green CHARA Laser	Laser Technologies	LRS-0532-PFM-00200-1
Red Alignment Laser	Thorlabs	S1FC635
STS Halogen Lamp	OceanOptics	HL-2000

should not be confused with the STS. An important remark when using the STS is that the STST should be out of the beam path of the STS beams, otherwise the signal strength for each beam of the STS is reduced.

3.3.1 Green CHARA Laser

Part of the CHARA facility and its instruments is a green bore sighting and laboratory alignment laser, which is roughly the size of the incoming light during on-sky observations and coincides with it [9]. Within the CHARA Array there are different green laser sources, thus the green CHARA lab alignment laser is referred to as the green CHARA laser in this thesis. Model and make information of this laser can be found in *Tab.* 4. This laser is placed on one of the optical tables in the BCL, where it is split in two beams. Similar to the selection of beam paths to telescopes, the two green laser beams can be matched sequentially to two consecutive beams for alignment. The green CHARA laser is used mainly during daily realignments in preparation of on-sky observations by CHARA employees. It was utilized to facilitate the optical alignment of the CHARIOT setup, in particular placement of **reference targets** with the pentaprism, using a visible beam, see *Ch.* 4.4.2.1. The "beaming" option for the green CHARA laser allows opening and closing a motorized iris, and therefore, the green CHARA laser beams converges to a small point and back to its full size while having alternating dark and bright circular fringes as seen in *Fig.* 11. Converging the CHARA beam enables a more precise alignment because of the alternating dark and bright central spot, which are easier to see and compare to the center of the targets — especially after long hours of alignment in a dimly illuminated lab.

3.3.2 Six Telescope Simulator (STS)

The CHARA facility has a new alignment and calibration source called the STS [31] as seen in *Fig.* 12, which was provided by the MIRC-X team. It consists of an upside-down telescope (Orion SkyQuest XT8) with a fiber-connected (FC/PC to

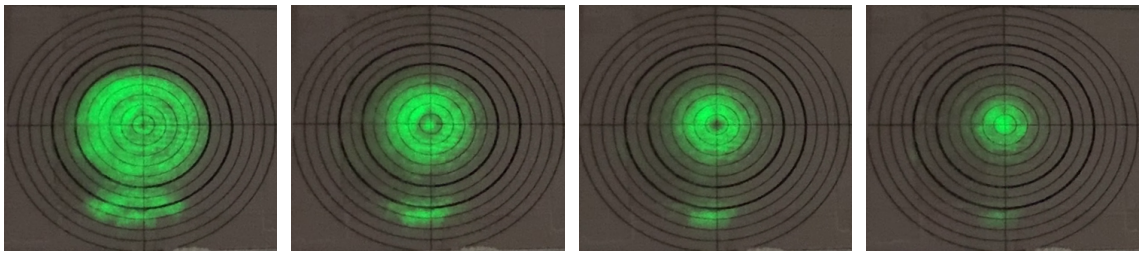

Figure 11: The green CHARA laser can be "beamed" via a program. The green CHARA laser converges to a small point shown in the images from left to right. Afterwards, the iris size, and therefore, the beam size increases again, going through different stages as seen from right to left. The center of the beam alternates from a bright to a dark spot during the "beaming" process (see the two images in the center). Hence, improving the precise alignment of the beam center on a target. This "beaming" process is realized by a motorized aperture, which closes and reopens, thus, creating a decreasing and increasing beam with an alternating bright and dark central spot.

free-space connector) Halogen white light source (see *Tab.* 4.) at the position, where the eye-piece would usually be located. At the telescope's entrance (here the exit of the STS), a coherent and collimated 8" ($\sim$ 20.32 cm) beam is picked-up by six 1" ($\sim$ 2.54 cm) mirrors. The six beams are co-aligned with the CHARA beams (including the telescope beams during on-sky observations). This means their size, angle and delay are as required to enable switching between various light sources without losing alignment [31]. The STS is located right before the BCL, close to the CHARA shutters and the STST, all of which are located on the last optical table before the light travels to the BCL. A program allows an easy switch between the STS, the white light source and the green CHARA laser. Usually, the STS is used for realignment and calibration purposes (even during on-sky observations) [31]. During the work on CHARIOT, the CHARA staff kindly exchanged the Halogen white light source with a red laser, which allowed fiber-coupling in the visible as a first step (the green laser was blocked by the fiber-coupling lens CL — see *Fig.* 13 and *Ch.* 4). Note that due to the fragile fiber connection of the white light source to the STS, the change of the light source should not be done on a regular basis and only carried out by CHARA staff.

The path length from the STS to the beam combiner is relatively short compared to the path length of the white light source. Difference in the overlap of telescope beams to lab sources are more noticeable for longer path lengths. Thus, for more precise overlap, the white light source might be the better source (a disadvantage is the lower intensity and the limit to two beams). The sequence STS - White light source - on-sky telescope light was one recommended sequence for alignment. However, with the CHARIOT instrument, a switch directly from STS to on-sky telescope light was successful during the observation nights.

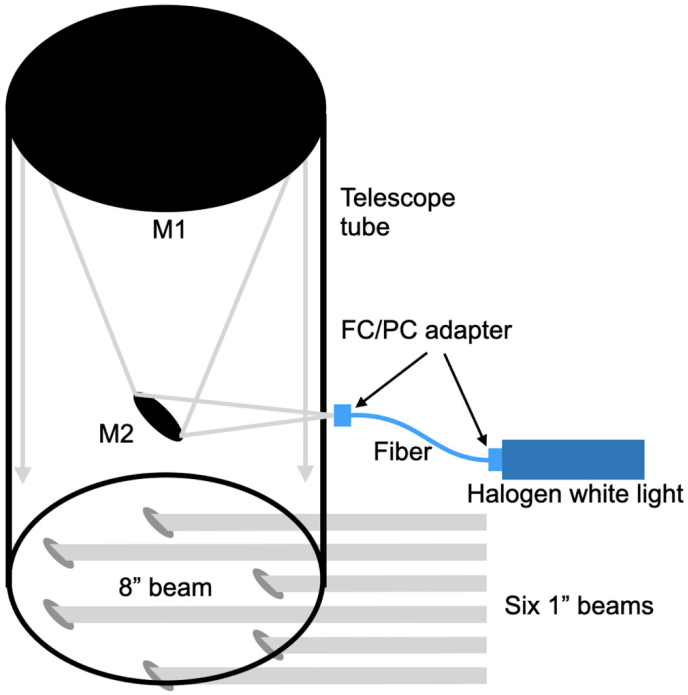

Figure 12: The CHARA Array has a new alignment and calibration source provided by the MIRC-X team. The STS consists of an upside-down telescope (Orion SkyQuest XT8) with a fiber-connected Halogen white light source in place of the eyepiece. At the telescopes entrance (here exit), a coherent and collimated 8" beam is picked-up by six 1" mirrors. The six beams are co-aligned with the CHARA beams (including the telescope beams during on-sky observations). Image taken from [31].

4 CHARIOT: CHara ARray Integrated Optics Testbench

Part of this thesis is the planning of the 4-beam and the optical alignment of the 2-beam CHARIOT instrument. The goal of CHARIOT is to achieve a fully characterized 4-beam (nulling) interferometry setup for lab and on-sky tests of novel astrophotonic 2D and 3D fiber-connectorized beam combiners accessible for the worldwide interferometry community. For that, CHARIOT is planned to cover the J-, H-, and K- bands with plug-and-play interfaces to enable an easy exchange of fiber-connectorized astrophotonic devices for lab and on-sky tests in a real interferometer array environment at the CHARA Array (see *Ch.* 3). CHARIOT is currently setup for two telescope beams, $B3$ and $B4$ (see *Fig.* 13), and is based on precursor instruments in the K-band: the Fiber-Linked Unit for Optical Recombination (FLUOR) [62] and its upgrade JouFLU (Jouvence of FLUOR) [63], which are explained in the following (*Ch.* 4.1). An overview of CHARIOT's goals and current status was presented during the SPIE Astronomical Telescopes + Instrumentation 2024 conference in Yokohama, Japan and can be found in [4].

4.1 History of FLUOR & JouFLU

CHARIOT is based on precursor instruments known as the Fiber-Linked Unit for Optical Recombination (FLUOR) [49, 62, 64] and its upgrade JouFLU (Jouvence of FLUOR) [3, 63]. Please refer to [3] for detailed information on the JouFLU instrument. FLUOR was a fiber-recombination instrument for high precision visibility measurements built by the Laboratoire d'Etudes Spatiales et d'Instumentation en Astrophysique (LESIA) of the Observatoire de Paris [49, 62, 64]. Initially, FLUOR was planned as an inexpensive proof-of-concept experiment on Kitt Peak, Arizona [64], in 1992 using two auxiliary telescopes of diameter $D_T = 80\,\mathrm{cm}$ and a maximum baseline of $B = 5.5\,\mathrm{m}$ [49, 62, 64]. Later on in 1995, an updated version of FLUOR was implemented on Mount Hopkins, Arizona, at the Infrared and Optical Telescope Array (IOTA) enabling to use FLUOR for scientific observations [49]. The IOTA/FLUOR instrument combined light from $D_T = 45\,\mathrm{cm}$ telescopes and baselines between $B = 7\,\mathrm{m}$ and $B = 38\,\mathrm{m}$ [49, 62, 64]. During this time, the IOTA/FLUOR instrument demonstrated high precision visibility measurements due to spatial filtering by coupling starlight into single-mode fibers. Even though coupling of light into single-mode fibers suffers from sensitivity loss, this result as presented in [49] paved the way for many beam combiners using spatial filtering as a tool to reduce the effects of atmospheric turbulences in the signal. Again after a few years, in 2002, FLUOR was moved to the CHARA Array at Mount Wilson, where it became opera-

tional for on-sky observations only a month later. Several upgrades were completed, after which the instrument was known as the Jouvence of FLUOR (JouFLU) [3, 63]. Among others, the upgrades included new motorized mounts for automated fiber-coupling optimization, motorized stages for OPD compensations and fringe scanning as well as a new experimental control software operable within the CHARA operation framework [3, 63].
In recent years, JouFLU was planned to undergo a series of smaller upgrades. This included an exchange of the fiber beam combiner (called "MONA" [3, 62]) with an achromatic fiber-connectorized ultrafast laser-written beam combiner (see *Ch.* 4.5) as a first step already. An unexpected failure of the JouFLU science camera (NICMOS) resulted in a modification to the scheduled sequence of planned upgrades. Consequently, more substantial upgrades were initiated, including the incorporation of a pick-off table and a reconfiguration of the overall setup to enable the addition of two beams in the future. Thus, the beam combination instrument was renamed CHARIOT.
CHARIOT is based on the optical table, software and many of the components of the previous instruments FLUOR and its upgrade JouFLU. Hence, even though the new CHARIOT setup is planned to combine four telescope beams in the J-, H- and K-band, the components from the 2-beam K-band JouFLU instrument are re-used to build the initial 2-beam K-band CHARIOT setup. Planning the 4-beam setup as well as aligning, testing and characterizing the 2-beam K-band CHARIOT setup were part of an Erasmus+ internship in 2023 and a Fizeau Exchange Visitors Program by the Eii in Spring of 2024. Results of this work are presented in the following.

4.2 CHARIOT — 4T Beam Layout

CHARIOT is planned to combine four telescopes, beams $B3$ to $B6$ as seen in *Fig.* 13, in the J-, H- and K-bands with a plug-and-play interface for fiber-connectorized novel astrophotonic beam combiners in laboratory- and on-sky tests. CHARIOT comprises two optical tables, the pick-off table and the CHARIOT table as depicted in *Fig.* 13. In principle, all six telescope beams from the CHARA Array could be picked up by the pick-off table, but for CHARIOT, a 4-beam setup is planned using the incoming CHARA beams $B3$ to $B6$. Two beams could be fully aligned and setup with components, which were either purchased or re-used from the precursor instruments FLUOR and JouFLU. Hence, in a future project, two more beams for beam paths $B5$ and $B6$ can be added without needing to change the 2-beam CHARIOT setup. Various different components are utilized to achieve beam redirection, fiber coupling and imaging of the outputs of the utilized beam combiner (see *Fig.* 13).

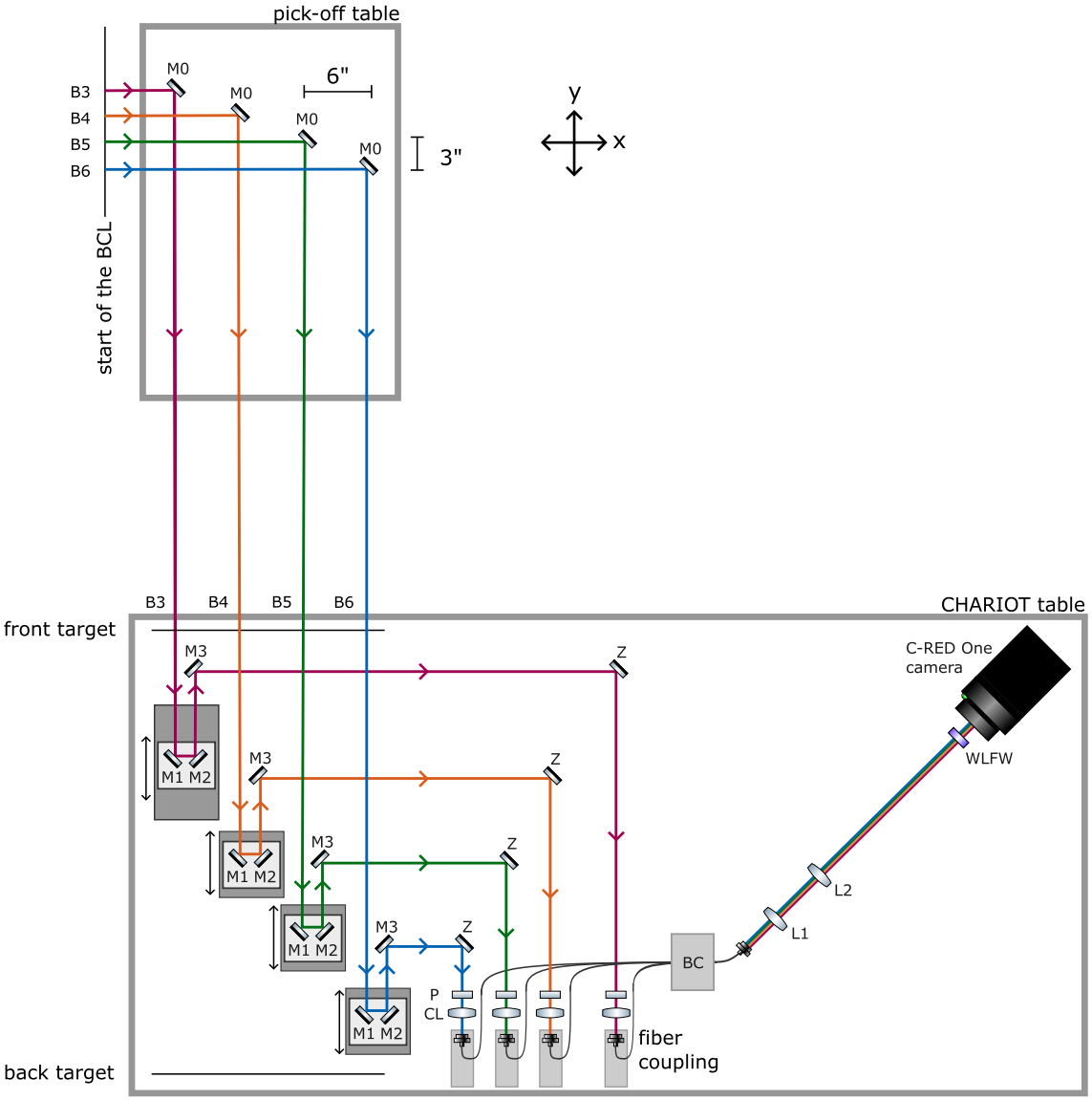

Figure 13: Planned 4-beam CHARIOT layout consisting of two optical tables, the pick-off and CHARIOT table. At the end of the beam redirection subsystem (at the position of fiber-coupling) various sources of OPD are accounted for, such as OPD before the start of the BCL, on the pick-off table and in the overall setup itself. In order to explain the alignment consistently for all components on both tables, a two-dimensional coordinate system is defined as shown in the layout. $M0$ are the pick-off mirrors for the beams $B3$ to $B6$. On the CHARIOT table, in each beam path, the following notation is used: mirrors $M1$ and $M2$ are part of the retro-reflector, which are placed on translational stages used for OPD corrections and fringe scanning. Afterwards in beam direction, $M3$ redirects the beam to a motorized Zaber mirror Z used for automated optimization of fiber-coupling. CL is the coupling lens, which focuses the light into the fiber tip that is secured by a fiber-holder placed on top of a six-axis photonics positioner. Afterwards, the beams enter the output imaging subsystem, which includes the fiber-connectorized beam combiner BC, a collimating lens $L1$, a focussing lens $L2$, a wavelength filter wheel $WLFW$ and a science camera (C-RED One Camera). The front and back target on the CHARIOT table are positioned as shown in the drawing. This figure as well as following ones make use of the ComponentLibrary [65] for optical diagrams.

Table 5: Summary of the models and makes of components in the CHARIOT setup. According to the data sheets, the back focal length of CL is 18.36 mm, while the focal length for $L1$ is 50 mm and 500 mm for $L2$.

Components	Make	Model
Mirrors	Thorlabs	PF20-03-P01
Zaber Mirror Mount	Zaber Technologies	T-MM2
Luminos Positioner	Luminos	I6000 6-Axis Positioner
Telecentric F-Theta Coupling Lens CL	Wavelength Opto-Electronic(s) Pte Ldt	TSLA-1.85-2.4-1-43-D19
Collimating Lense $L1$	Thorlabs	AL72550-E1
Focusing Lens $L2$	Thorlabs	LA5456-D

An overview of the model and make information of the components in CHARIOT can be found in *Tab.* 5. Mirrors $M0$ to $M3$ are used for beam redirection, while the motorized Zaber mirror Z is implemented in order to optimize the fiber-coupling (see *Fig.* 13). Currently, the search algorithm for the highest throughput of the fiber-coupling is a linear snake-like line-by-line method. In future work, the search algorithm will be replaced by a spiral search as it is implemented in other instruments at CHARA. This approach allows for the interruption of a search if the peak is found near the center, as well as the extension of the search to regions farther away from the center without the necessity of repeating measurements. Afterwards, the polarization controllers P will ensure a high fringe contrast. The optimization of these components is the scope of future work. A telecentric f-theta lens is used as the coupling lens CL (see *Tab.* 5). For this specific lens CL (telecentric f-theta lens), angles in the incoming beam in front of the lens result in the output being shifted in the x, y-plane at the output of the CL. Its back focal length is 18.36 mm according to its data sheet. Thus, the lens CL should be placed at this distance to the fiber holder on top of the multi-axis Luminos positioner (see *Tab.* 5 for make and model information of this and other components). The coupled light is redirected to an achromatic fiber-connectorized K-band ULI-written beam combiner, which was fabricated by a group at the Heriot-Watt University [66, 67]. The combiner comprises two interferometric and two photometric outputs, which are arranged in a rectangular two-by-two configuration. See *Ch.* 4.5 for more information on the beam combiner. Currently, a two-lens system ($L1$ and $L2$ in *Tab.* 5) is utilized to image the outputs together on a C-RED One camera. In the context of this thesis, CHARIOT is divided in two subsystems: the **redirection subsystem** and the **output imaging subsystem** and will be discussed separately.

Redirection Subsystem The redirection subsystem comprises all components from $M0$ up to including the fiber-coupling (see *Fig.* 13). The pick-off mirrors $M0$

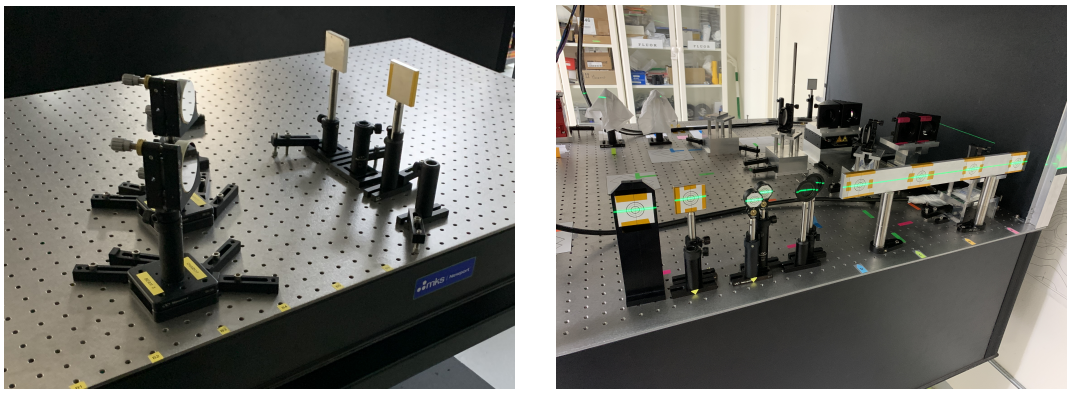

(a) (b)

Figure 14: (a) Pick-off mirrors $M0$ on the pick-off table for beams $B3$ and $B4$. Magnetic mounts allow easy insertion and removal of pick-off mirrors. (b) CHARIOT targets including CHARIOT "front target" and flip targets, which can be placed in various post holders along each beam path. These targets were used during initial beam alignment and are required for regular realignment of pick-off mirrors.

are placed on magnetic mounts as depicted in *Fig.* 14a. The mirrors utilized within the CHARIOT setup are 2" optics from Thorlabs (see *Tab.* 5). In order to redirect the light to the CHARIOT setup (e.g. for laboratory tests or engineering nights), the pick-off mirrors $M0$ must be put in place on the magnetic mounts. While CHARIOT is not in use, all pick-off mirrors have to be removed from the beam path in order to avoid blocking other instruments and experiments. Thus, each time the pick-off mirrors $M0$ are put in place, they require realignment to at least two targets on the CHARIOT table. This is done to ensure a straight and flat beam redirection without introducing unwanted angles and errors, which could lead to loss of sensitivity. The first target on the right is the "front target" on the CHARIOT table and the two circular target in the center are the flipable targets (see *Fig.* 14b). For alignment purposes, the flipable target can be inserted into different post holders along each beam path in several locations, which were placed during the initial alignment of the beams. After the beam is redirected to the CHARIOT table as seen in *Fig.* 13, the beam travels to the two mirrors $M1$ and $M2$ placed at 45 ° each on translational stages as shown in *Fig.* 15. These mirrors, called retro-reflectors in this thesis, redirect the outgoing beam parallel to the incoming beam. Hence, when moving the translational stages within their travel range, the optical path length changes twice as much as the movement of the stage due to the double pass created by $M1$ and $M2$. The properties of the translational stages are summarized in *Tab.* 6. The stage in beam $B3$, called static stage or STAT stage (Newport UTS100PP Motorized Linear Stage), has a longer travel range (see *Tab.* 6) and can compensate for larger OPD. The STAT stage was used for (slow) temporal fringe scanning during initial lab tests of CHARIOT, which is discussed in *Ch.* 4.6.1. For beams $B4$ to $B6$, the

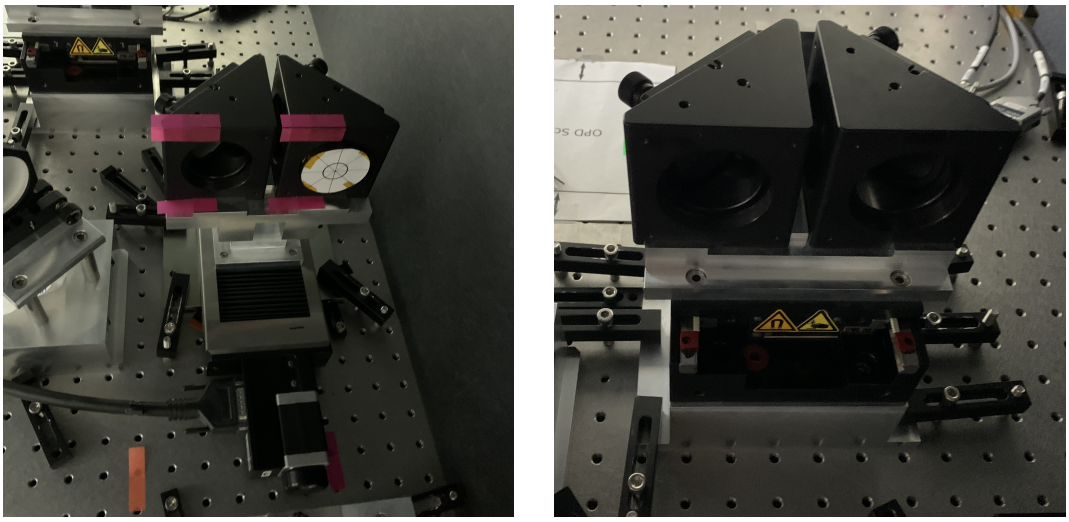

(a) (b)

Figure 15: The translational stages are shown with the mirrors $M1$ and $M2$. (a) Static stage (Newport UTS100PP) in beam path $B3$ used to compensate OPD due to misalignment. (b) Scanning stage (Newport XMS50) in beam path $B4$ is utilized for fringe scanning. The same or a similar model as the scanning stage is planned for beams $B5$ and $B6$. Even though the scanning stage has a smaller travel range, it can compensate for small OPD and scan for temporal fringes. Specification for both stages can be found in *Tab.* 6.

Table 6: Specification of used translational stages (STAT stage in beam path $B3$ and SCAN stages in beam paths $B4$ to $B6$) in the CHARIOT layout as seen in *Fig.* 13. Values are taken from [3] and the corresponding data sheets for both stages.

Specifications	STAT stage	SCAN stage
Model	Newport UTS100PP	Newport XMS50
Travel range	10 cm	5 cm
Maximum velocity	20 mm/s	300 mm/s

scanning stages or SCAN stages (Newport XMS50) are planned, which can be used for both small OPD correction offsets and fast fringe scanning, see *Tab.* 6 for its specifications.

In addition to the stages in the CHARIOT setup, the delay lines of the CHARA Array can be employed to compensate for on-sky offsets and for OPD corrections.

Once the beams passed through the stages with the mirrors $M1$ and $M2$, the mirrors $M3$ direct the beams to motorized Zaber mirrors Z (see *Tab.* 5) utilized for automized optimization of fiber-coupling as shown in *Fig.* 16. The fiber-coupling part of CHARIOT consists of a polarization controller P and a focusing lens CL for the K-band (see *Tab.* 5). This is the last part within the redirection subsystem, which is followed by the output imaging subsystem.

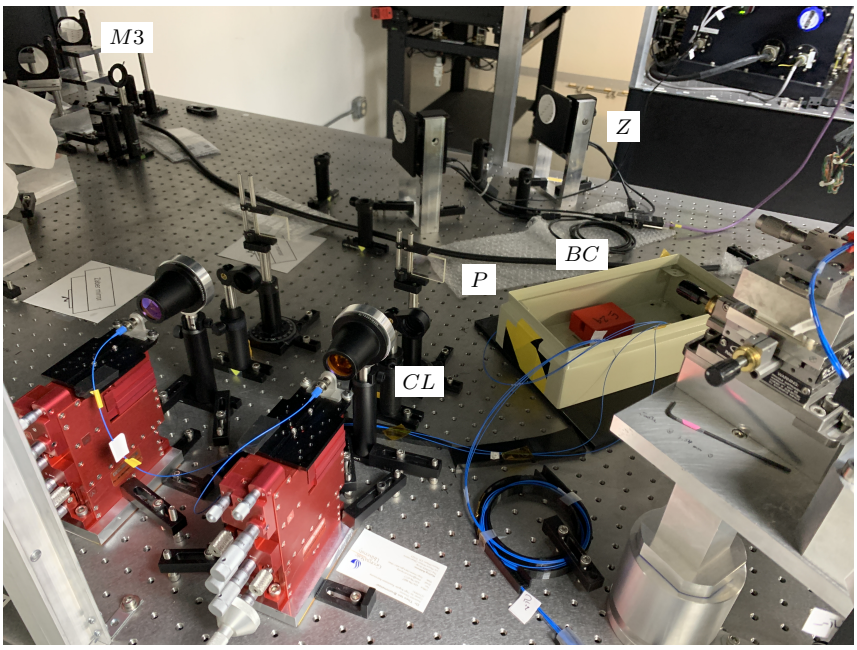

Figure 16: In the upper left corner, the mirrors $M3$ are visible directing the beams to the motorized Zaber mirrors Z (see *Tab.* 5) in the upper center of the image, which are used for automated fiber-coupling optimization. The fiber-coupling part of CHARIOT for each beam path consists of a polarization controller P, a fiber-coupling lens CL and a fiber-holder placed on a six-axis photonics positioner stage. Further on the right is the box housing the fiber-connectorized K-band beam combiner BC written with the ULI technique (see *Ch.* 5.3).

Output Imaging Subsystem Once the light beams are fiber-coupled, they can be interfered within the beam combiner. This is part of the output imaging subsystem together with the two-lens system as shown on the right in *Fig.* 13. Currently implemented into the CHARIOT setup is a fiber-connectorized K-band beam combiner written with ULI (see *Ch.* 5.3), which will be verified within CHARIOT in lab and on-sky tests as part of the NAIR-2 / APREXIS project. The combiner has two interferometric and two photometric outputs, which are arranged in a rectangular two-by-two configuration. Thus, the four outputs are off-axis to the lens system. A more detailed description of the currently implemented beam combiner can be found in *Ch.* 4.5. In the CHARIOT setup, the beam combiner BC output fibers are placed in front of an output imaging subsystem on the CHARIOT table. At this point in time, the output imaging subsystem consists of a collimating lens $L1$, a focusing lens $L2$, a wavelength filter wheel $WLFW$ for various central wavelengths and bandwidths as well as the C-RED One camera as shown in *Fig.* 17. The lens system within the output imaging subsystem is likely to be optimized in future changes to ensure as little light loss and aberrations as possible. Information on the two-lens system is summarized in *Tab.* 5.

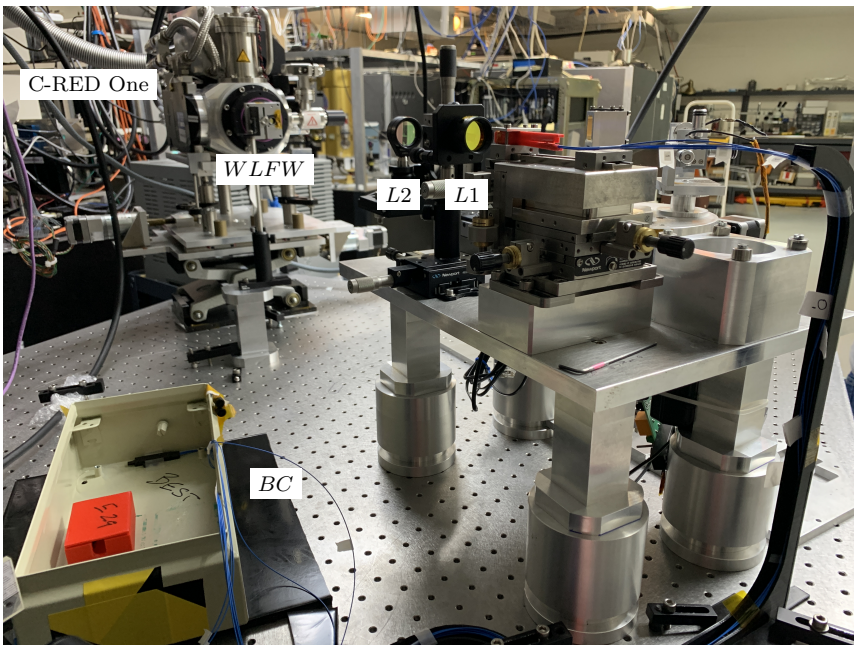

Figure 17: Output imaging subsystem consisting of the fiber outputs of the astrophotonic beam combiner BC, followed by a collimating lens $L1$, a focusing lens $L2$, a wavelength filter wheel $WLFW$ for a variety of central wavelengths and bandwidths as well as the C-RED One science camera.

The setup as shown in *Fig.* 13 was aligned, characterized, and tested in the lab and on-sky for two telescope beams $B3$ and $B4$. In *Ch.* 4.6 the experimental verification of the 2-beam CHARIOT setup is discussed.
A critical point in the design of the 4-beam and alignment of the 2-beam CHARIOT setup was the compensation of all sources of OPD, including OPD introduced by the beam shaping optics prior to the start of the BCL, as well as OPD within the CHARIOT setup itself. The following chapter, *Ch.* 4.3, will describe the OPD corrections in the CHARIOT setup in more detail.

4.3 OPD Corrections

When using broadband light (as opposed to monochromatic laser light), it is crucial to correct precisely for any OPD. Only when the OPD is corrected within the coherence length Δl_{coh} it is possible to achieve fringes in an interferometric setup. The coherence length can be described by

$$\Delta l_{\mathrm{coh}} = \frac{\lambda^2}{\Delta\lambda} = \frac{c}{\Delta\nu}, \tag{7}$$

where λ is the central wavelength and $\Delta\lambda$ the bandwidth. Note that the bandwidth $\Delta\lambda$ describes the FWHM of the incoming signal as usually defined for astronomical bands (see *Ch.* 1 and *Tab.* 1). Usually, the bandwidth $\Delta\lambda$ and the central wavelength

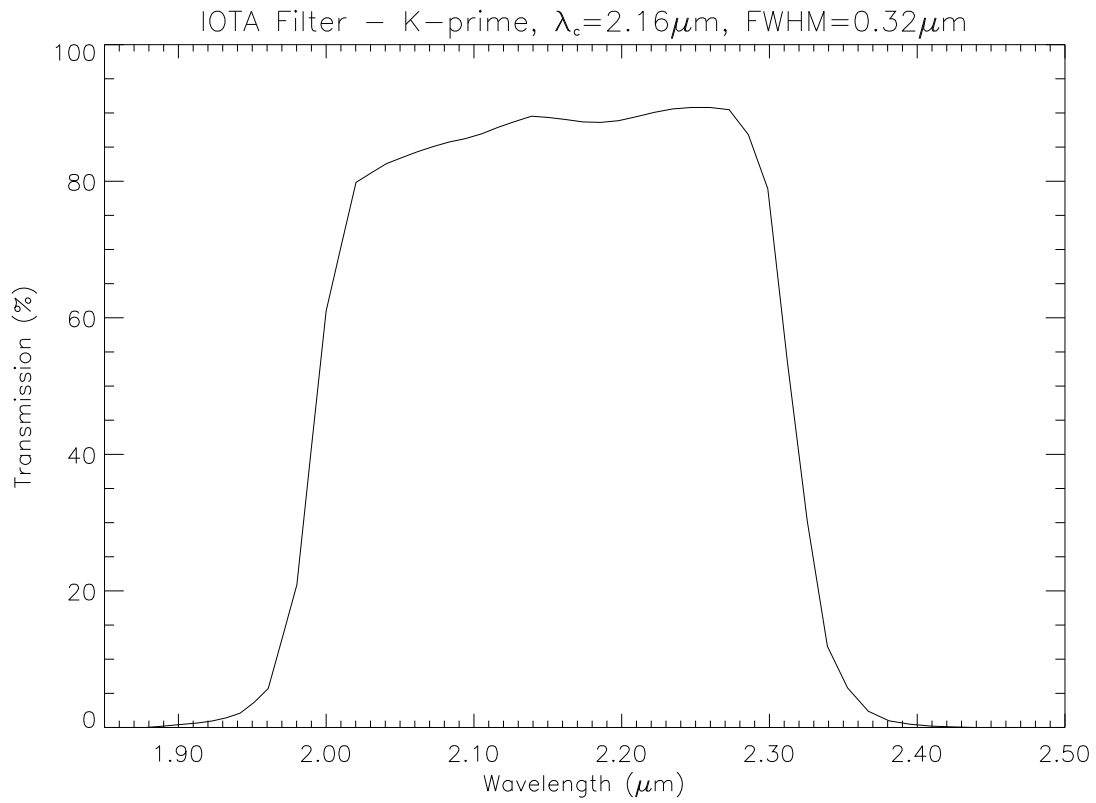

Figure 18: Transmission curve of the K'-filter currently in use in the CHARIOT setup with a central wavelength of $\lambda = 2.16\,\mu$m and a bandwidth of $\Delta\lambda = 0.32\,\mu$m [3]. The filter wheel is part of the components from the precursor instrument JouFLU. This image is taken from [3] (image credit: Rafael Millan-Gabet).

λ are determined by a wavelength filter in the setup [39]. Within the CHARIOT setup, different filters from the filter wheel $WLFW$ can be chosen (see *Ch.* 4.4.4.2). The coherence length can also be given in terms of frequency bandwidth $\Delta\nu$, however the wavelength dependent version of *Eq.* 7 is commonly used in optical direct interferometry. In the context of this thesis and in many textbooks, the coherence length is defined as the distance between zero OPD (center of the white light fringe) and the path length at which the visibility function is reduced to zero [37, 39]. Note that a different definition can be found in [34], where the bandwidth is defined as the Half Width at Half Maximum (HWHM), and therefore, the coherence length is twice as long as the coherence length defined here and used in the context of this thesis.

The CHARIOT setup includes a filter wheel consisting of several wavelength filters for different center wavelengths and bandwidths from the predecessor instrument JouFLU. Currently, the K'-filter with a central wavelength of $\lambda = 2.16\,\mu$m and a bandwidth of $\Delta\lambda = 0.32\,\mu$m [3] is in use, as shown in *Fig.* 18. Hence, for the K'-filter, the coherence length can be calculated with *Eq.* 7 to be $\Delta l^{\mathrm{K'}}_{\mathrm{coh,\ cal}} = \frac{(2.16\,\mu\mathrm{m})^2}{0.32\,\mu\mathrm{m}} \sim 14.58\,\mu$m. The importance and challenge of compensating OPD within the coher-

Table 7: The OPD introduced before the start of the BCL, on the pick-off table and overall before the CHARIOT table is given for all consecutive beams and for the most distant beams $B3$ and $B6$. See *Fig.* 13 for the planned CHARIOT layout.

Relative OPD in inches / Position	$B4$-$B3$	$B5$-$B4$	$B6$-$B5$	$B6$-$B3$
offset at the start of the BCL	11.2	11.2	11.2	33.6
on pick-off-table	3	3	3	9
(sum) before the CHARIOT table	14.2	14.2	14.2	42.6

ence length cannot be emphasized enough. Without the precise compensation within roughly $\sim 15\,\mu$m creating fringes and collecting information about stellar objects is impossible. The delay lines of the CHARA Array already compensate for OPD created in the several hundred meters long beams paths from different telescopes to the BCL. Further, in the overall CHARIOT setup comprised of pick-off and CHARIOT table, the beams travel several more meters ($\sim 5\,$m), for which the OPD needs to be corrected within the comparably small coherence length of $\sim 15\,\mu$m. As a consequence, all four future beams for the CHARIOT setup, have to be precisely planned and aligned to ensure ideally no OPD is present between all beams at the position of the fiber-coupling. In reality, the OPD has to be small enough to be compensated using the stages. Care was taken to minimize the OPD in the setup to within the measurement uncertainties. Otherwise, no interferometric signal can be achieved. Thus, the stages included in the CHARIOT setup are used for compensating OPD caused by small misalignments that are within their travel range as discussed in *Ch.* 4.2. To be more even precise, the compensable OPD is twice the travel range due to the double pass created by mirrors $M1$ and $M2$ on the stages [3]. In addition to the critical OPD correction, the design of the CHARIOT setup had to take into account the physical space for the travel ranges of the stages as well as sufficient space for mounting. Furthermore, the given space on the CHARIOT optical table had to be used as efficiently as possible. To design the 4-beam layout on the CHARIOT table, the OPD constraints must be examined. The OPD introduced before the start of the BCL and before the CHARIOT table is discussed below.
Due to beam shaping optics before the start of the BCL, the incoming beams already have an OPD of 11.2" = 28.45 cm between two consecutive beams. Additionally, OPD is created by the placement of the pick-off mirrors $M0$ of 3" = 7.62 cm. Overall, after the pick-off table and before the CHARIOT optical table is an OPD of 14.2" = 36.07 cm between consecutive beams (as summarized in *Tab.* 7), which needs to be compensated on the CHARIOT optical table up to the fiber-coupling. Hence, after the pick-off table and before the CHARIOT optical table, the longest

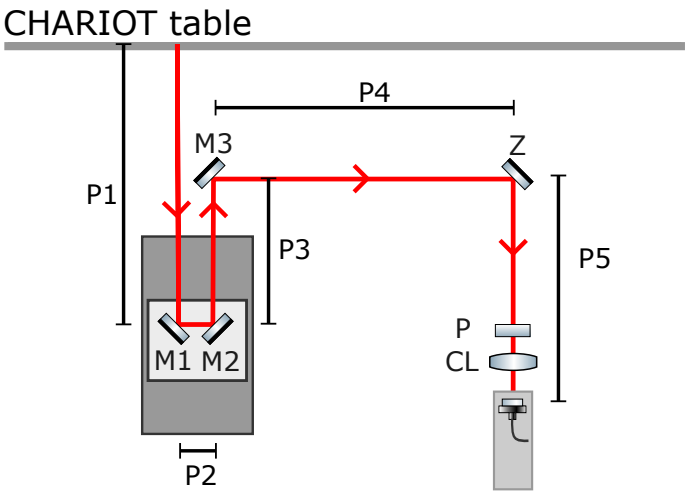

Figure 19: Schematic of exemplary beam path on the CHARIOT table including path labels $P1$ to $P5$ used for describing path lengths and OPDs on the CHARIOT optical table.

Table 8: Path lengths for paths $P1$ to $P5$ on the CHARIOT table as depicted in *Fig.* 19. All beams are planned in a "V"-shaped configuration to compensate the OPD introduced before the CHARIOT optical table as summarized in *Tab.* 7.

Path lengths in inches \ Beam	$B3$	$B4$	$B5$	$B6$
$P1$	16.3	25.20	33.1	41.0
$P2$	3.5	3.5	3.5	3.5
$P3$	10.8	10.7	9.6	8.5
$P4$	44.5	30.5	18.5	6.5
$P5$	34	25	16	7
Sum $P1$ to $P5$	109.1	94.9	80.7	66.5

overall OPD between the most distant beams $B3$ and $B6$ is 42.6" = 108.2 cm. This needs to be compensated on the CHARIOT table, which is accomplished by a "V"-shaped layout of the components used on the CHARIOT table as seen in *Fig.* 13 and with path labels in *Fig.* 19. Each path length for paths $P1$ to $P5$ on the CHARIOT table as depicted in *Fig.* 19 is summarized in *Tab.* 8. These path lengths can be used to check the OPD after each individual beam path $P1$ to $P5$ and overall at the position of fiber-coupling as summarized in *Tab.* 9. Actually, the beam paths $P1$ to $P5$ should exhibit comparable relative OPDs between two consecutive beams. However, the relative OPD between $B4$ and $B3$ differs due to the increased space requirements of the STAT stage in $B3$. Here, it is shown that the total OPD on the CHARIOT table is equal to the OPD before it but in opposite direction as indicated by the minus signs. Thus, the "V"-shaped CHARIOT layout shown in *Figs.* 13 and 19 corrects for the OPD created before the start of the BCL and on the pick-off table as summarized in *Tab.* 10. In theory, the OPD

Table 9: OPD for paths $P1$ to $P5$ on the CHARIOT table and total OPD on the CHARIOT table itself.

Relative OPD in inches / Path	$B4$-$B3$	$B5$-$B4$	$B6$-$B5$	$B6$-$B3$
$P1$	8.9	7.9	7.9	24.7
$P2$	0	0	0	0
$P3$	-0.1	-1.1	-1.1	-2.3
$P4$	-14	-12	-12	-38
$P5$	-9	-9	-9	-27
Sum $P1$ to $P5$	-14.2	-14.2	-14.2	-42.6

Table 10: OPD for the overall CHARIOT setup including both pick-off and CHARIOT table.

Relative OPD in inches / Position	$B4$-$B3$	$B5$-$B4$	$B6$-$B5$	$B6$-$B3$
offset at the start of the BCL	11.2	11.2	11.2	33.6
on pick-off table	3	3	3	9
(sum) before the CHARIOT table	14.2	14.2	14.2	42.6
on CHARIOT table	-14.2	-14.2	-14.2	-42.6
(sum) complete beam path	0	0	0	0

will be corrected for all four beams if aligned according to the planned layout in *Fig.* 13. In practice, checking if the OPD is truly compensated requires achieving fringes within the coherence length of the signal. In 2023, the 2-beam CHARIOT setup for beams $B3$ and $B4$ was aligned up to fiber-coupling in the visible with a red laser attached to the STS (see *Ch.* 3.3.2). The work on the CHARIOT instrument was continued in 2024. Among other tasks, the output imaging system was aligned and a new astronomical camera (C-RED One camera) was installed into the setup. Hence, it was possible to check if the OPD was correctly compensated for beam paths $B3$ and $B4$ by using the STS with a halogen lamp injected into it as a calibration lab source. The ULI-written fiber-connectorized K-band beam combiner was produced by project partners as part of the NAIR-2 / APREXIS collaboration. In *Ch.* 4.6.1, the OPD compensation is verified in lab experiments and the coherence lengths measured for various bandwidth sizes using different filters from the filter wheel. The proof-of-concept measurements as part of an on-sky engineering night with CHARIOT are briefly presented in *Ch.* 4.6.2. Methods and procedures to align the 2-beam CHARIOT redirection setup are described in more detail in the following.

4.4 CHARIOT — 2T Optical Alignment

CHARIOT, as planned for four telescope beam combination, will be completed in multiple steps. Before the research trip in 2023, the whole CHARIOT optical table was relocated to be in a position in which a pick-off table could be used. Previously, these mirrors had to be mounted on the optical table from another instrument. The new pick-off table was required to improve the stability of the system. It also provides more space for future extensions of the setup to four telescope beam combination and possibly an additional adaptive optics setup. During this relocation of the CHARIOT optical table, the table height, and thus, the beam height changed slightly and needed to be corrected before starting the alignment of the 2-beam CHARIOT setup for beams $B3$ and $B4$. Due to the reuse of the components and the optical table of the JouFLU instrument, the mounts create a fixed beam height of 6.5” measured from the surface of the optical table. Therefore, this beam height had to be restored in order to keep all mounts instead of replacing or changing them. The procedure for the beam height correction of the CHARIOT optical table can be found in *Ch.* A.1 in the appendix together with how various targets for the beam alignment were created. In 2023, a preliminary pick-off table was used until it was replaced with a more stable Newport pick-off table (VIS3048-PG4-325A Optical Working Station) later on. Thus, a few alignment steps were repeated during a realignment phase after the pick-off table was replaced by a Newport optical

table. Aligning the 2-beam CHARIOT setup was achieved up to the fiber-coupling using a red laser injected into the STS. In 2023, the new science camera (C-RED One) was sent to the manufacturer to change the filter in the camera to enable K- and H-band measurements. Therefore, the fiber-coupling in the NIR, working on the output imaging setup and the integration of the C-RED One camera among other tasks were scope of the research visit in 2024 during which lab and on-sky fringes were achieved (see *Ch.* 4.6) with the 2-beam K-band CHARIOT setup and a ULI-written fiber-connectorized K-band beam combiner (see *Ch.* 4.5) produced by project partners. Before explaining the optical alignment process, the general alignment goals as well as various alignment tools are presented.

4.4.1 Alignment Goal

The setup was designed to correct all OPD, i.e. with equal path lengths in all arms. In reality, small path differences can be introduced, most likely during the positioning of optics. Along the beam, this was done within the $\simeq$ mm precision of rulers and other tools. Thus, with a total path length from the start of lab to the fiber coupler of around 5 m and $\sim$ 6 optical components that may introduce small differences, a total OPD on the order of mm − cm between the two beams can be expected. This can be compensated with the translational stages. In order to achieve the best possible alignment, different tools and techniques are utilized.
The goal of the alignment is to generate a perpendicular and flat beam redirection throughout the complete beam path according to the planned CHARIOT setup as explained above in *Ch.* 4.2 and in *Fig.* 13. In the context of this thesis, a *perpendicular* beam means the following: In the x-y-plane defined in *Fig.* 13, the incoming and outgoing beams at each optical component are perpendicular to each other. Further, *flat* describes that the correct beam height is maintained and does not change throughout the complete setup. More specifically, the optical components create a flat outgoing beam between the beam and the table without introducing an angle, that would otherwise change the beam height. The incoming beams at the pick-off table are the reference for the complete setup. On the pick-off and CHARIOT table, an outgoing beam should be perpendicular and flat compared to the incoming beam in order to ensure an OPD corrected beam path for all beams in the setup. During the alignment process, it was noticed that the CHARIOT table is tilted in the x-y-plane. Hence, the table grid of the rows of holes on the table is not parallel to the beams of the setup. While this leads to the setup seemingly being tilted when compared to the grid of screw holes on the CHARIOT table, the beam is in fact aligned to be perpendicular and flat with respect to the incoming beam. The alignment process will be explained in more detail in the following, after the alignment tools have been introduced.

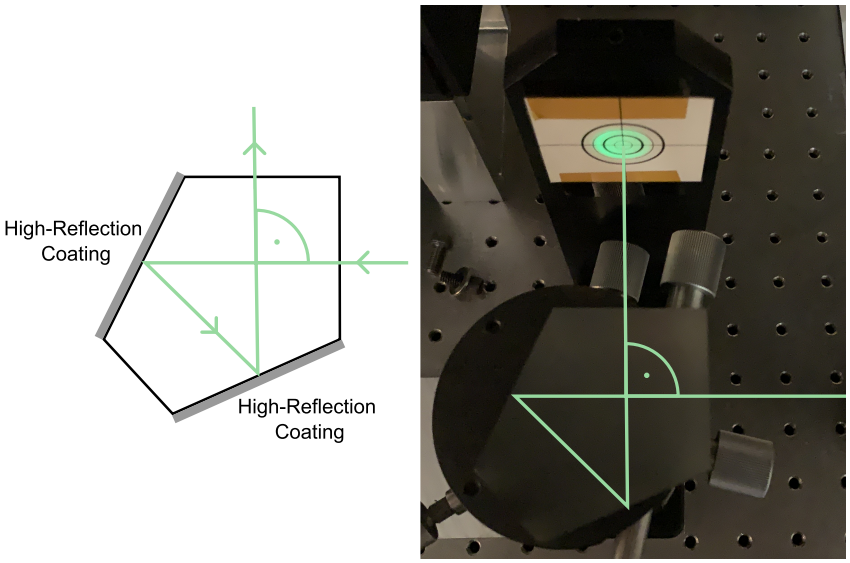

Figure 20: A pentaprism is a five sided prism with two high-reflection coated sides (long sides of the pentaprism). The pentaprism is a tool, which redirects the outgoing beam perpendicular to the incoming beam without being sensitive to the exact orientation of the pentaprism to the incoming beam [68, 69]. Nonetheless, the side of the pentaprism was aligned to the center of the incoming beam during the alignment process. The image schematically shows the beam redirection within the pentaprism.

4.4.2 Alignment Tools

To ensure a correct optical alignment of the CHARIOT setup, different tools were utilized including standard tools such as rulers, paper cards and tape as well as more specific tools, such as a pentaprism and a theodolite. For the alignment in the visible, the green CHARA laser was used. The STS was utilized when connected with a red laser for fiber-coupling in the visible, and later for fringe measurements in the NIR with the Halogen lamp injected into the STS described in *Ch.* 3.3.2.

4.4.2.1 Pentaprism A pentaprism as seen in *Fig.* 20 is a five sided prism with high-reflection coating on the two longer sides, which creates a perpendicular outgoing beam compared to the incoming beam [68, 69]. Precise perpendicular redirection of the beams to ensure correctly placed targets along the complete beam path was a crucial task during the initial optical alignment phase. Using a pentaprism has the advantage of creating a 90 ° angle between the incoming and outgoing beam in the x-y-plane independent of the precise orientation of the pentaprism to the incoming beam [69]. Hence, small differences in the angle of the pentaprism did not change the position of the redirected beam, and therefore, did not alter the placement of the targets throughout the setup. Nonetheless, the pentaprism was aligned in such a way, that the side facing the incoming beam was roughly perpendicular and centered to the beam (see *Fig.* 20) and placed according to the planned CHARIOT

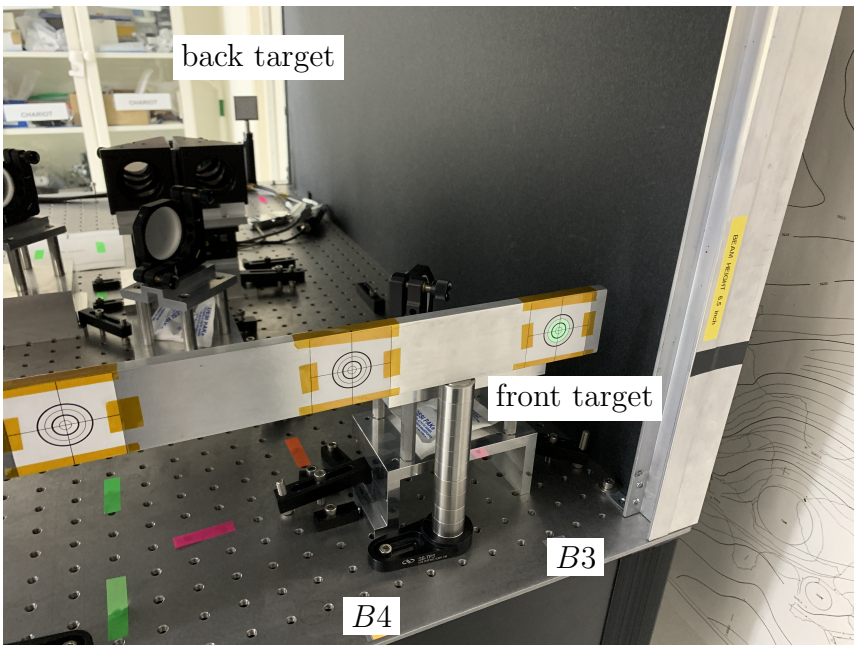

Figure 21: The *front target* and *back target* are used to align the pick-off mirrors but also for the alignment of the theodolite for the realignment process. At the start of the optical table, the beam paths are for the incoming beam $B3$ to $B6$, from right to left, respectively (i.e. the rightmost beam path is for $B3$, and the leftmost path is for $B6$).

layout (see *Fig.* 13). The pentaprism was only utilized during the initial alignment phase to place all reference targets precisely. For the realignment phase — after the pick-off table was replaced — a theodolite was used.

Target Alignment with the Pentaprism Following the correction of the CHARIOT optical table height (see *Ch.* A.1), a series of targets were aligned to the appropriate beam height. For both the table height correction and target height alignment, a self leveling laser with a free hanging laser hat was used as seen in *Ch.* A.1. In order to position targets on the CHARIOT table for the alignment of the pick-off mirrors and other components in the beam path, the pentaprism can be used. As an example, the position of the back target utilizing the pentaprism is explained in this paragraph. Positioning other targets on the CHARIOT table is done analogously. The *front target* on the CHARIOT table as seen in *Fig.* 21 was already fixed in position after the beam height corrections of the CHARIOT table and determines the position of the entering beam. With the pentaprism, a second target can be positioned, which is depicted as *back target* in *Fig.* 21. Both targets ensure a perpendicular and flat alignment of the pick-off mirrors. The pentraprism is positioned on the pick-off table and needs to be roughly at the correct height to hit the center of the front target at the start of the CHARIOT table. As a next step, the pentaprism should be positioned in such a way that the incoming beam hits the first side of the

pentaprism in the center. Afterwards, the pentaprism can be moved in x-direction on the pick-off table until the center of the CHARA green laser beam hits the center of the front target at the start of the CHARIOT table. Once the correct pentaprism position is achieved, the pentaprism should not be moved until the back target on the CHARIOT table is correctly placed. Similarly, other targets can be placed along the beam path. For example, two targets are placed between $M3$ and Z as well as between Z and P as depicted in *Fig.* 13. In both cases, one target is close to the beginning of the redirected beam (near $M3$ and Z respectively) and the other target further away close to the following component (here Z and P). Having two targets, one near and one far from the optical component, allows for proper alignment of both the beam position and its angle. Precise alignments were critical to ensure the OPD was corrected as planned in the CHARIOT layout (see *Fig.* 13). However, as explained above, the CHARIOT table (its grid of screw holes) is tilted compared to the perpendicular redirected beam. Thus, the position of the closest target (and position of the pentaprism) was chosen according to the planned CHARIOT layout. This position can be found within the grid of screw holes on the table. Whereas the target further away was determined by the perpendicular redirected beam of the correctly placed pentaprism, even if its position did not exactly match a row of screw holes on the table.

4.4.2.2 Theodolite A theodolite (as seen in *Fig.* 22) is a precise tool to measure horizontal and vertical angles. It consists of a narrow field-of-view telescope with alignment crosshairs, which can be mounted on a tripod and rotated along its vertical and horizontal axis to measure even small angles precisely [70]. Theodolites are commonly used in surveying but were utilized for the realignment phase. For that, the theodolite must be precisely aligned to the front and back target of the CHARIOT table as seen in *Fig.* 13 and its position locked. Afterwards, the optical components on the CHARIOT table can be inserted one after another and aligned using the theodolite by changing the focus onto various targets along the beam path.

Positioning of the Theodolite Before the optical components on the CHARIOT target can be aligned, the theodolite itself needs to be placed and aligned correctly. The only possible placement of the theodolite is at the short side of the pick-off table the farthest away from the CHARIOT table, and not in between mirrors $M0$ and $M1$ (see *Fig.* 22). Otherwise, the theodolite itself would block its view of the targets on the pick-off table that are used to align the mirror $M2$ as described in *Ch.* 4.4.3.2. Placing and aligning the theodolite can be achieved following a procedure:

1. Position the theodolite roughly in the correct x-position and ensure focusing along the chosen beam path is possible.

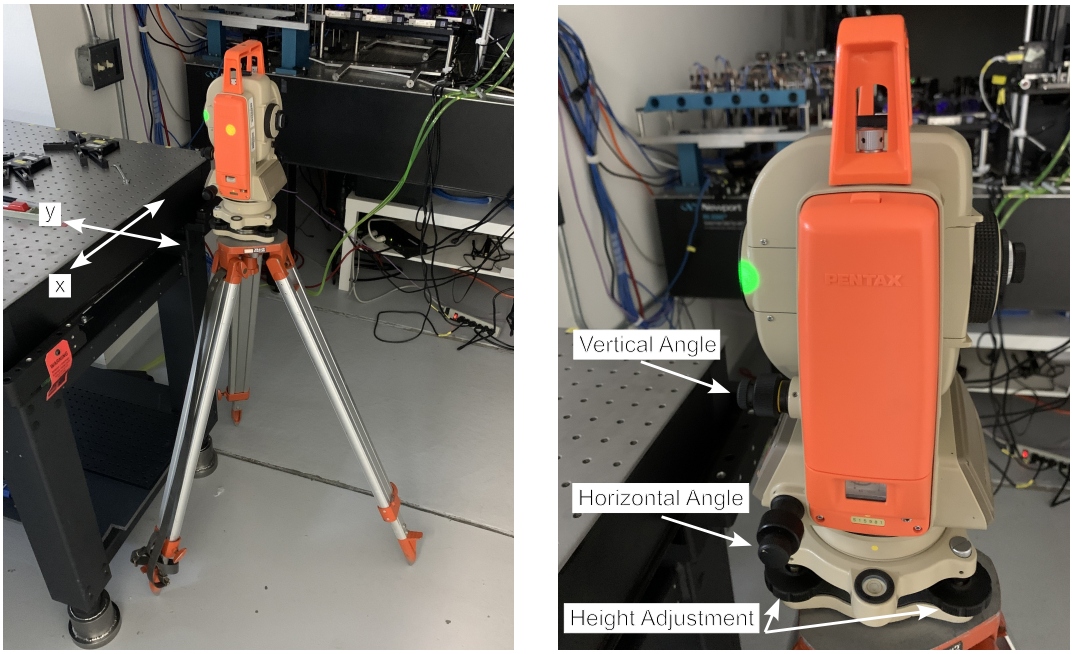

Figure 22: A theodolite is a precise tool to measure small vertical and horizontal angles. It consists of a telescope mounted on a tripod (left), which can be rotated along its vertical and horizontal axis [70]. The correct height of the tripod can be achieved by aligning the middle of its objective lens to the center of the green CHARA laser (right). The lowest three screws closest to the platform of the tripod can change the height of the theodolite. Two of the three lowest screws are visible in the image. With the other two screws the horizontal and vertical angle of the theodolite can be changed.

2. The correct height is found once the center of the objective lens of the theodolite is aligned to the center of the green CHARA laser beam as seen *Fig.* 22 on the right. ⇒ The placement of the theodolite in x-direction and height is an iterative process. For larger height changes, the legs of the tripod might need to be elongated, shortened or changed in angle. Due to the floor not being level, this can again change the x-position of the theodolite.

3. After the legs of the tripod are positioned and fixed, different screws can be used to do the precise alignment.

4. Correct the x-position precisely by moving the screw that attaches the theodolite to the platform along a rectangular hole within tripod platform.

5. Adjust the height, horizontal and vertical angle of the theodolite by using several screws as seen in *Fig.* 22 on the right.

6. Iteratively correct the precise alignment in x-direction, height and angles until the crosshair of the theodolite coincides with the front and back targets as seen in *Fig.* 23. It can be easier to first correct only one dimension. This means either the height together with the vertical rotation or solely x-position and the horizontal angle. This technique is similar to the well known technique of *Beam Walking* where two mirrors are used (as described in [71]).

After the alignment, the theodolite should not be changed except for the focus. A precise placement and alignment of the theodolite to the front and back target is crucial for a precise realignment of the optical components on the CHARIOT table.

4.4.3 CHARIOT — Redirection Subsystem

In this chapter, the alignment of the various components of CHARIOT's redirection subsystem is explained as seen in *Fig.* 24. The redirection subsystem includes the complete beam path up to including the fiber-coupling. The alignment is explained for one beam and was repeated analogously for the other beam. Currently, two beams — $B3$ and $B4$ — were aligned with available components, which were either specifically purchased or inherited from the precursor instruments FLUOR and JouFLU. In the future, two more beams can be implemented by following the alignment process described here.

4.4.3.1 $M0$ Pick-off Mirror Critical for the CHARIOT setup is a correct and precise alignment of the pick-off mirrors $M0$ on the pick-off table shown in *Fig.* 13. For that, the front and back target described in *Ch.* 4.4.2.2 can be used. Therefore, no other component (as the stages with mirrors $M1$ and $M2$) can be in the beam

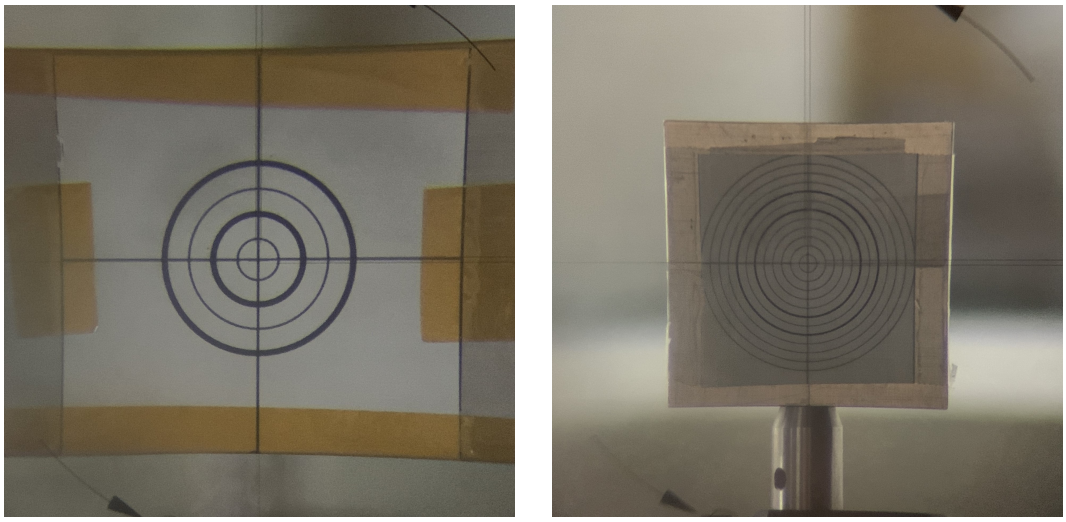

Figure 23: Both images show the view through the eye piece of the theodolite. The theodolite has a cross-hair, which can be aligned to different targets. The lines of the cross-hair are faintly visible in the picture, where they overlap with the lines on the target. In the left image is the front target and on the right is the back target of the CHARIOT table. These images were taken after the theodolite was aligned correctly to both targets. With the correctly aligned theodolite, it is possible to focus onto different targets along the beam path while precisely aligning the optical components of the setup.

path which would block the back target used during this alignment process. The pick-off mirrors are placed on a magnetic mount consisting of two magnetically connectable plates. One magnetic plate is attached to the mirror mount and the other — the base plate — is permanently fixed to the table. Aligning the base plate precisely is very important because the pick-off mirrors need to be removed when CHARIOT is not in use to avoid blocking light going to other instruments in the BCL of the CHARA facility. At the start of the $M0$ alignment, the magnetic bases of the pick-off mirrors should not be screwed in yet. Due to the angled clearance in the bottom part of the magnetic base, changing the pick-off mirror position in only one dimension is very difficult if a screw is loosely holding the base in place. Thus, the first alignment is done with the magnetic base not screwed on the table and checked after fixing the position. An image of the bottom part of the magnetic mount (base plate) for the pick-off mirrors can be found in *Fig.* 25. The pick-off mirrors should be placed according to the planned CHARIOT layout as shown in *Fig.* 13. The correct height is accomplished by centering the mirror to the green CHARA laser. For that, a piece of paper is put close to the mirror without touching it (see *Fig.* 26, left). The piece of paper should be in the plane with the incoming beam path. Afterwards, the pick-off mirrors can be aligned in **y-direction** as follows:

1. Rotate the mirror to be roughly angled at 45 ° to the incoming beam.

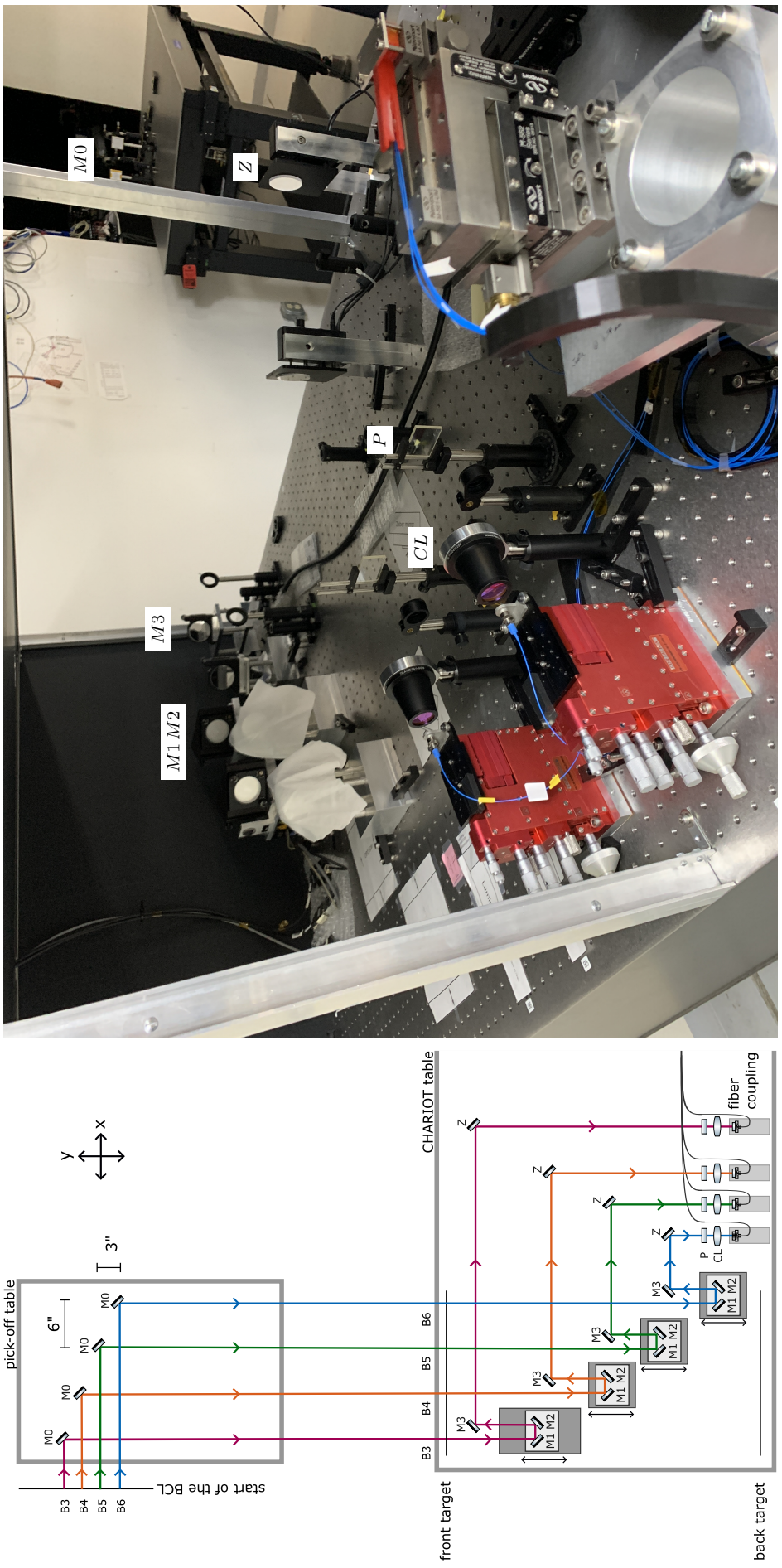

Figure 24: Layout and image with labels for the redirection subsystem of CHARIOT including the beam path up to including the fiber-coupling. On the left, the layout for the subsystem is shown and on the right is an image of it. In the image, the various components are labelled as in the layout on the left exemplary for the components in beam path $B3$.

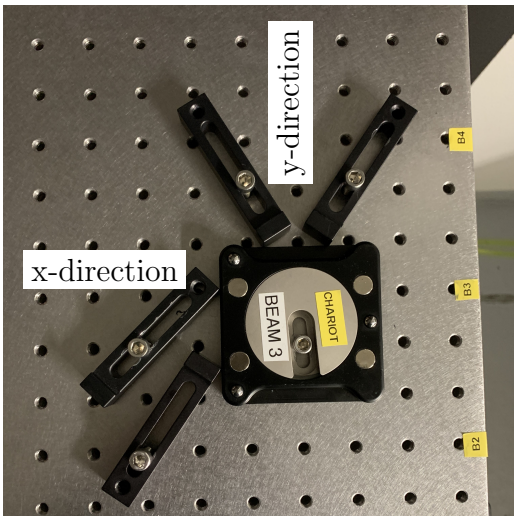

Figure 25: Clamps are used to help position the magnetic base for the pick-off mirrors. The y-position is fixed with two clamps first, to ensure a centered beam on the mirror. These clamps allow to move the base only in the x-direction. The clamps in the x-direction can be used to support finding the correct position for the pick-off mirror. After the position is correct and checked on both front and back target on the CHARIOT table, the magnetic base can be screwed in place.

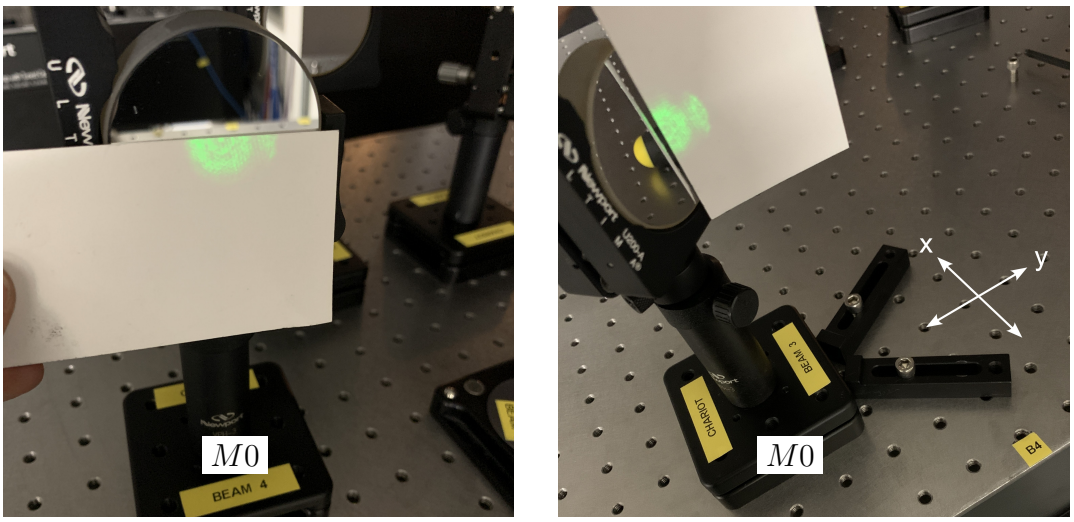

Figure 26: A piece of paper can be put into the beam path close to the mirror without touching it to check the centering of the beam on the mirror. In the left picture, the beam height can be adjusted and fixed by using a collar. After rotating the mirror into a 45 ° position, the centering can be corrected by moving the mirror in the y-direction as depicted on the CHARIOT layout in *Fig.* 13.

2. Determine the y-position by centering the CHARA green laser beam on the pick-off mirror $M0$.

3. Check if the base is at an angle compared to the grid of screw holes and possibly correct it.

4. Use the edges of two clamps to fix the y-position of the base plate (see *Fig.* 26, right).

After fixing two clamps, the magnetic base can be moved in the x-direction only. Achieving the **x-position** is a bit more difficult and can be done with the following procedure:

1. Align $M0$ to the center of the front target.

2. Check the alignment of the redirected beam on the back target.

3. If the beam is off-center on the back target, correct the angle of the mirror and check the front and back target.

4. If the beam is off-center on the front target, correct the x-position of the mirror. Check the alignment on the front and back target.

5. Iteratively repeat the steps above until the beam is aligned to both targets simultaneously.

This technique is similar to the well known technique of *Beam Walking* where two mirrors are used. In the case of the CHARIOT setup, one mirror has to be moved in the x-y-plane (position) and its rotation (pitch and yaw) needs to be corrected instead of solely changing pitch and yaw of two mirrors at fixed positions.
Note that similar to the clamps for the y-position, clamps can be used to help with finding the correct x-position (see *Fig.* 25). Once the base plate is fixed, check the alignment on both targets again and repeat the process above if necessary.
The precise positioning of the pick-off mirror is crucial for the alignment of the downstream optical components, and should therefore be done precisely for example by "beaming" the green CHARA laser as shown in *Fig.* 11. The redirected beam from the pick-off mirrors $M0$ to the first component on the CHARIOT table is already a few meters long. Therefore, even small misalignments can later result in OPD between the beams, which should be avoided and then corrected in the setup. Once the mirrors $M0$ are correctly aligned, the beams are redirected to the stages and mirrors $M1$ and $M2$, which are discussed in the next part.

4.4.3.2 Translational Stages with Mirrors $M1$ and $M2$ During the initial phase, the alignment of the translational stages and their mirrors $M1$ and $M2$ were done in the visible using the green CHARA laser. Later, during the realignment phase, the theodolite was used for the alignment of these components. An image of the two types of stages used for beams $B3$ and $B4$ are shown in *Fig.* 15. In this chapter, the alignment using the theodolite is explained in detail, but the visible alignment with the green CHARA laser can be done analogously. If a theodolite is available, it is the preferred tool for the alignment of this component due to its precise measurement of even small angles over large distances. Aligning this component can be divided in two parts: the alignment of the stage itself, and afterwards, the alignment of the mirrors $M1$ and $M2$ on top of the stage.

Translational Stage Alignment Before aligning the translation stage, the mirror $M3$ must be removed from the beam path so that it does not block the view from the theodolite during the following steps. After the positioning of the theodolite and its alignment to the front and back target of the CHARIOT table as described in *Ch.* 4.4.2.2, the stage can be inserted back into the beam path. For the CHARA beam $B3$ the static stage (STAT stage) is inserted into the beam path while for $B4$ the scanning stage (SCAN stage) is used. As mentioned above, the hole grid pattern of the CHARIOT optical table seems rotated in the x-y-plane compared to the incoming perpendicular redirected beams. Thus, the alignment of the translational stages cannot be done by aligning them to the rows of holes on the table. Furthermore, because of the travel range of the stages, the retro-reflectors cannot be only positioned in their neutral position. Neutral position here means that the mirrors on the translational stages are having the same amount of travel range in both directions. Therefore, the potential movement across the travel range of the stages has to be taken into account.

The stages can be aligned in their neutral position using the following procedure:

1. Inserted a target in front of the mirror $M1$. The target is visible through the theodolite as shown in *Fig.* 27.

2. Fix the y-position according to the optical layout as seen in *Fig.* 13. Keeping the y-position can be achieved by placing the edge of a clamp either in the front or the back of the stage.

3. Find the correct x-position by moving the stage in x-direction until the center of the target is aligned to the cross-hair of the theodolite.

4. Temporarily clamp down the stage and check the beam height of the stage. In both cases for beams $B3$ and $B4$ the height of the stages needed to be corrected.

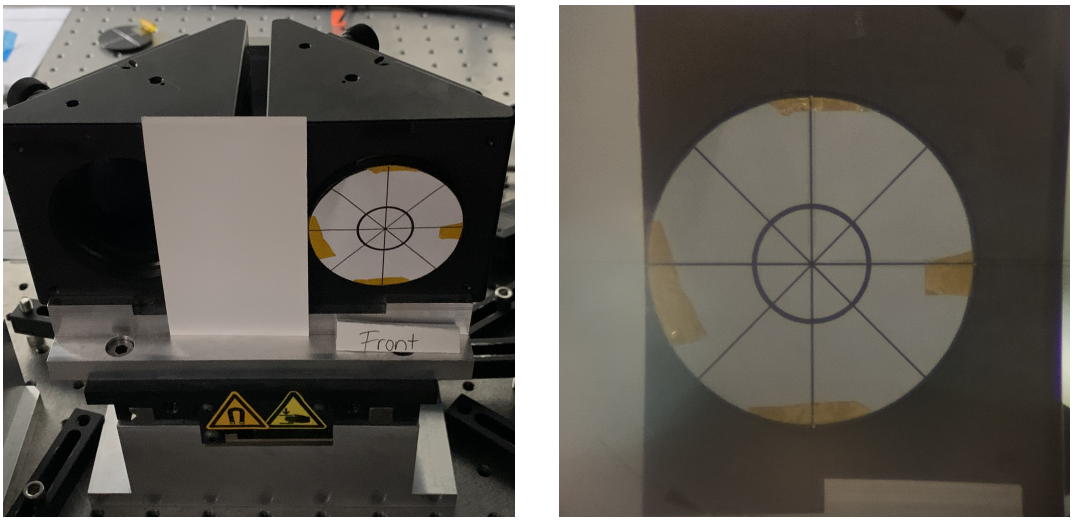

Figure 27: Left image shows the paper target inserted in front of mirror $M1$ not facing the mirror but visible from the theodolite as seen on the right. The correct alignment is achieved by aligning the center of the paper target with the cross-hair of the theodolite. The alignment should not change when the stage is moved within its travel range. Small changes in the height and rotation of the stage during its travel range result in a change of the beam position further along in the beam path. Nevertheless, small corrections can be performed with the Zaber mirror Z later in the beam path.

> Therefore, shims (plastic sheets) of different thicknesses were positioned in several positions under the stages to achieve the correct beam height on the stage.

Now, the rough alignment is done in the neutral position of the stage. To achieve an overall correct alignment, the stage needs to be moved within its full travel range. The scanning stage (in beam $B4$) can be moved freely while it is not powered, while the static stage (in beam $B3$) can be controlled and moved via software only. While changing the stage within their travel range, it was noticed that the alignment gets lost due to the stage not having the correct alignment in the x-y-plane yet. Correcting the rotation to align the target on the stage to the cross-hair of the theodolite is an iterative process. The stage needs to be rotated, changed in x-position and checked on the theodolite for the complete travel range. Changing the position of the stage on the table might result in a height change and the shims under the stage need to be adapted accordingly in the final stage position. Note that as long as the stage is not completely clamped down, the height might differ to when it is permanently fixed on the optical table. Hence, aligning the stages in all dimensions is achieved iteratively. Even with a lot of effort, the scanning stage could not be as precisely aligned as the static stage. Since the scanning stage is only meant to dither a few hundred microns around a fixed position, this is not expected to severely affect the measurements during laboratory- and on-sky tests.

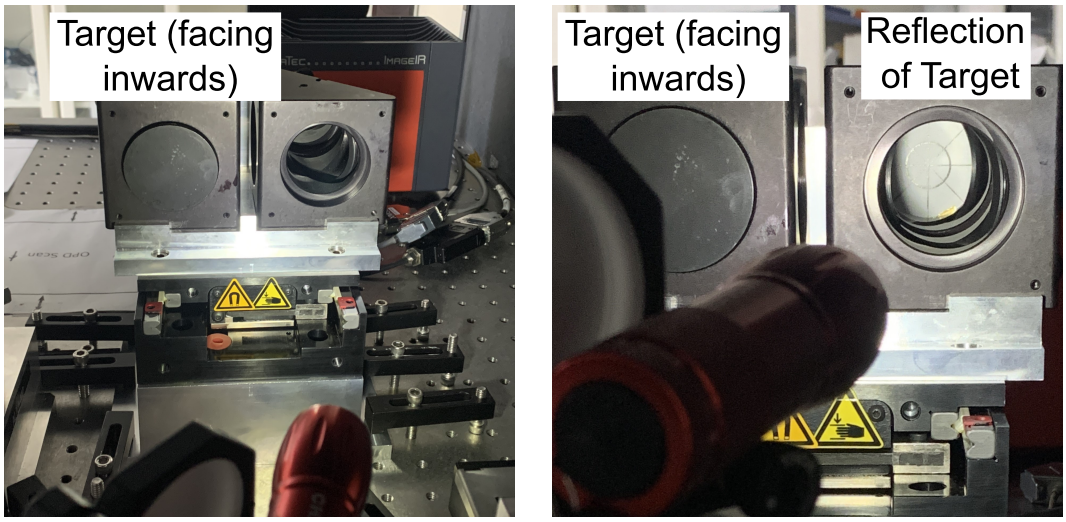

Figure 28: On the left the target in front of mirror $M2$ is shown with the paper target facing mirror $M2$. On the right, the reflection of the paper target after $M2$ and $M1$ is shown. The reflection of the paper target is only visible when a flashlight is positioned in front of the stages illuminating the entrance of the mirror mount while not blocking the view for the theodolite. With the entrance being illuminated, it is possible to see the target with the theodolite.

However, if the absolute scanning stage position is changed or if the dither range is drastically increased, fiber coupling may suffer due to beam misalignment. If required, the motorized mirrors Z can compensate small changes when searching for the optimum fiber-coupling throughput. Now that the stage itself is aligned correctly, the alignment of the mirrors $M1$ and $M2$ can be done.

Alignment of Mirrors $M1$ and $M2$ After the translational stages themselves are aligned for their complete travel range, the mirrors $M1$ and $M2$ that are mounted on top of the stages must be aligned. First, mirror $M1$ can be aligned by removing the paper target from its position in the previous step and inserting the target in front of and facing mirror $M2$ as seen in *Fig.* 28. With this target inserted, the mirror position of mirror $M1$ can be corrected until the target is aligned to the cross-hair of the theodolite as shown in *Fig.* 29. If the stage is moved within its travel range, the alignment as seen through the Theodolite should not change and if it changes slightly the stage itself is not perfectly aligned. Small corrections can be applied with the motorized Zaber mirror Z later in the beam path. Larger shifts require a correction of the stage alignment. Once the mirror is correctly aligned, the mirror $M2$ can be corrected. The two mirrors $M1$ and $M2$ are meant to create a double pass with the reflected beam parallel to the incoming beam (coming from $M0$). Hence, the distance between the incoming and outgoing beam should be the separation of both mirrors $M1$ and $M2$ on the stage. In order to measure the mirror separation, i.e. the distance between the mirror centers, a target is placed in front of

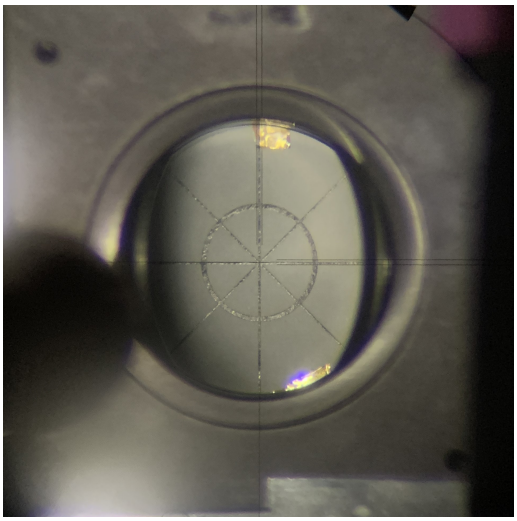

Figure 29: The paper target that is mounted in front of — and facing — $M2$ is reflected by mirrors $M2$ and $M1$, which can be seen here. This setup can be used to align the mirror position of mirror $M1$. As seen in the image, the entrance of the retro-reflector is illuminated by a flashlight without it blocking the view from the theodolite. The mirror $M1$ position is corrected until the paper target is aligned to the cross-hair of the theodolite.

each mirror on the stage, as shown in *Fig.* 30. The distance between the centers of the targets, and thus the mirror separation, is measured as 8.55 cm. Afterwards, two targets are placed on the new pick-off table with a separation of 8.55 cm as shown in the left image in *Fig.* 31. Now, the translation stages and the mirrors $M1$ and $M2$ should be correctly aligned for the whole travel range of the stage. In case of a shift in the alignment when the stage is moved within its full travel range, it needs to be decided whether this can be compensated with the motorized Zaber mirror Z later in the setup or if the stage position and alignment needs to be corrected. If the stage needs to be corrected, then the mirror alignment should be checked afterwards again. In principle, the retro-reflector stage is now correctly aligned and the mirror $M3$ can be inserted back into the beam path for the next alignment step.

4.4.3.3 Mirror $M3$ For the alignment of the mirror $M3$ the theodolite can be used as well. If the mirror is not at its correct position, it appears cut-off and off-center when viewed through the theodolite as shown in *Fig.* 32 on the left. For this test, the theodolite has to be focused on a reference target behind the mirror, but the edge of the mirror is still visible in the beam path. This can be corrected by moving the mirror along the x-direction to align with the two reference targets. Both targets are in the reflected beam path after mirror $M3$. One target is close to the mirror, and one at a far away position (close to and in front of the motorized Zaber mirror Z). For a correct alignment of $M3$, the center of both targets should coincide with the cross-hair of the theodolite. Positioning $M3$ in the y-direction is determined by the

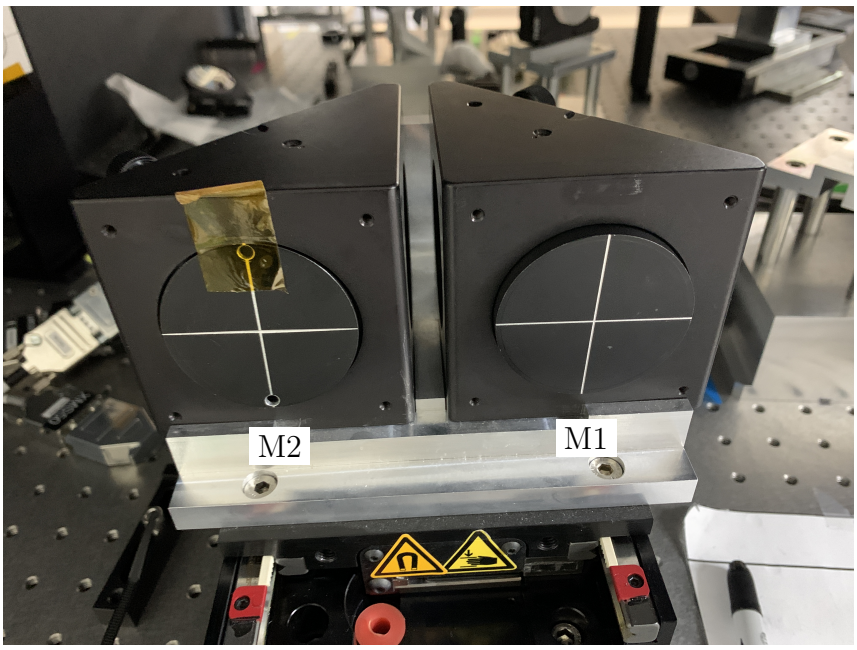

Figure 30: The separation of both mirrors needs to be measured in order to be able to place two targets on the pick-off table at the same distance. Therefore, two targets are put in front of the mirrors on the stage and the distance between the center of mirror $M1$ to $M2$ is measured to be 8.55 cm. The left target in front of mirror $M2$ is slightly smaller and had to be taped in place for the measurement.

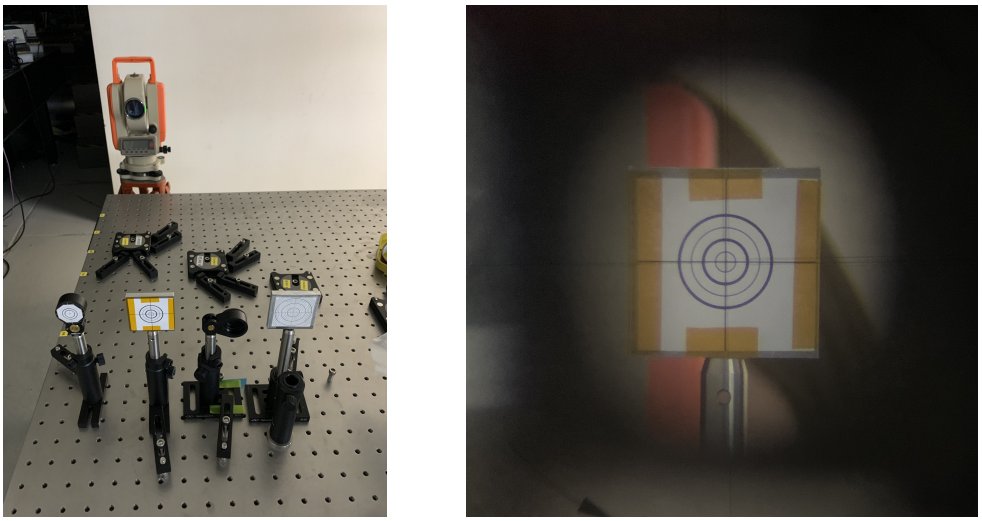

Figure 31: In the left image, the two targets placed at a distance of 8.55 cm are shown for both beam paths $B3$ and $B4$. In the back behind the flipable targets is the theodolite. In this image, the theodolite focuses onto the second target from the left with the orange tape. The view of this target through the theodolite is seen in the right image. To be able to focus on this target, the flipable target needs to be flipped out of the beam path and the focus of the theodolite changed accordingly. Now the screws for the mirror alignment for mirror $M2$ can be corrected until the target is aligned to the cross-hair of the theodolite. For a perfectly aligned stage, the beam position should not shift when the stage moves.

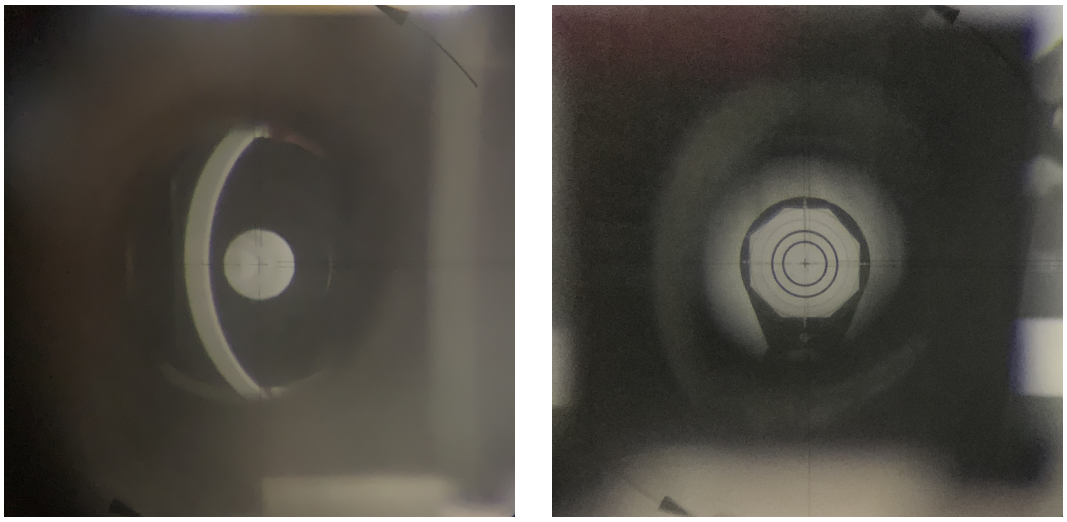

Figure 32: Left: View of an incorrectly placed mirror $M3$ through the theodolite, which focuses onto a target. In the case of a misaligned mirror, the edge of the mirror is visible instead of a centered mirror to the cross-hair of the theodolite. Right: A target in the beam path following $M3$ is focused on. A correct alignment of $M3$ is achieved once the target coincides with the cross-hair of the theodolite.

optical layout (distance between the translational stages with mirrors $M1$ and $M2$ to mirror $M3$) to ensure an overall OPD correction. By iteratively correcting position and angle of the mirror $M3$, the mirror can be aligned correctly. As previously mentioned, this process is similar to the well-known *Beam Walking*. If the mirror $M3$ is aligned correctly, it is possible to see the target in the beam path being aligned to the cross-hair of the theodolite as seen in *Fig.* 32 on the right. Now that the alignment of the mirror $M3$ is done, the motorized Zaber mirror Z and fiber-holder on top of the six-axis photonics positioner can be aligned using the theodolite before the lens CL is aligned using the green CHARA laser and a back-injected red laser.

4.4.3.4 Motorized Zaber Mirror Z Similar to the mirror $M3$ the motorized Zaber mirror Z can be aligned using the theodolite. For that, two targets were positioned in the beam path of the reflected beam after the Zaber mirror Z and before the position of the polarization controller P, the focusing lens CL and the fiber-holder on top of a Luminos positioner. One important aspect of the motorized Zaber mirror Z is that it is a steering mirror, and therefore, when aligning Z, the mirror should be in a neutral position to enable an equal amount of travel range in all directions. During on-sky tests, the motorized mirror Z can be used to optimize fiber-coupling with on-sky light. The x-position should be kept as planned in the optical layout (distance between mirror $M3$ and Z). The y-position is determined by the perpendicular redirected beam and the reference targets. For the Zaber mirror Z alignment, the theodolite is focused on two targets in the following beam path,

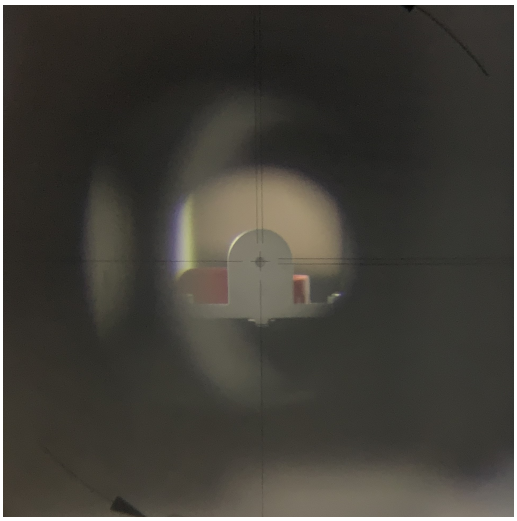

Figure 33: Aligning the center of the fiber-holder to the cross-hair of the theodolite to ensure an overall aligned setup. The y-position should be kept as planned in the optical layout (distance between fiber-holder and Z) while the x-position can be aligned with the theodolite. Further, the height of the fiber-holder (and the mount of the Luminos positioner) can be corrected with shims (plastic sheets of different thicknesses) if necessary.

analogous to the alignment of $M3$, and therefore, a similar image as in *Fig.* 32 on the right is visible for the alignment of Z.

4.4.3.5 Fiber-Holder on a Luminos Positioner After the motorized Zaber mirror Z is aligned to two reference targets, the fiber-holders on a six-axis photonics positioner can be precisely aligned using the theodolite. This is done by aligning the center of the hole of the fiber-holder on the Luminos positioner to the cross-hair of the theodolite as seen in *Fig.* 33. This can be achieved with the following procedure:

1. The y-position should be kept as planned in the optical layout (distance between the fiber-holder and mirror Z).
2. Move the positioner in x-direction until the fiber-holder (fiber tip for light insertion) is aligned to the cross-hair of the theodolite.
3. Similarly, the height of the fiber-holder can be corrected with plastic shims placed under the mount.

During this alignment process, it is important to ensure the screws of the Luminos positioner have equal travel range for adaption during the fiber-coupling. The alignment of the fiber-holder is completed when the center of the hole of the fiber-holder coincides with the cross-hair of the theodolite as in *Fig.* 33. This is the last component in the setup that is aligned using the theodolite. The complete process has to be repeated for the other beam(s) in the CHARIOT setup. Finally, the focusing lens CL is aligned utilizing a back-injected red laser and the green CHARA laser.

4.4.3.6 Alignment of the focusing lens CL In *Fig.* 34 on the left is the fiber-coupling part of the full CHARIOT layout depicted. The complete layout is shown in *Fig.* 13. The notation for this part of the alignment description is as follows: The terms *in front of* and *before* CL is in the direction of the beam path. Hence, in case of a target being *in front of* or *before* the focusing lens CL, it is the section of the beam path between the focusing lens CL and the motorized Zaber mirror Z. Furthermore, if the complete beam path *in front of* or *before* CL is described, the beam path sections between the start of the BCL, mirrors $M0$, $M1$, $M2$, $M3$, Z and P up to the focusing lens CL are referred to. If the beam path section *after*, *behind* or at the *back* of the focusing lens CL is part of an explanation, the section of the beam path between the lens CL and the fiber-holder on top of the Luminos positioner is described. For the alignment of CL, a red laser is connected to the fiber-holder on the Luminos positioner for back-injection. Information about the red laser can be found in *Tab.* 4. A correct alignment of CL can be achieved with the following steps:

1. Place a target onto the back cap of the lens CL.
2. Align the x-position of the lens by aligning the center of the target with the back-injected red laser as seen in *Fig.* 34. For that, a long metal block was clamped on the side of the mount to slide the lens CL along the x-direction.
3. Remove the back cap in order to allow the red laser to pass through the lens (see *Fig.* 35).
4. Place another target attached to an empty lens holder in front of the lens CL.
5. Overlap the green CHARA laser with the back-injected red laser (see *Fig.* 36). This step ensures the correct x-position and angle (rotation) of the lens CL.
6. Find the correct y-direction (distance from fiber-holder), which should be equal to the back focal length of the lens of 18.36 mm according to the data sheet.
7. For that, place a metal block in order to allow sliding along the y-direction.
8. The correct distance is achieved when the back-injected red laser is collimated in front of the lens along the complete beam path. In other words, the back-injected red laser must have the same size throughout the complete beam path in front of the lens CL.
9. Finish the alignment, by first fixing the lens and checking the alignment again.

The correct position of the lens CL can be checked with several targets in the beam path in front of CL. The overlap of both lasers can be seen on the front target in

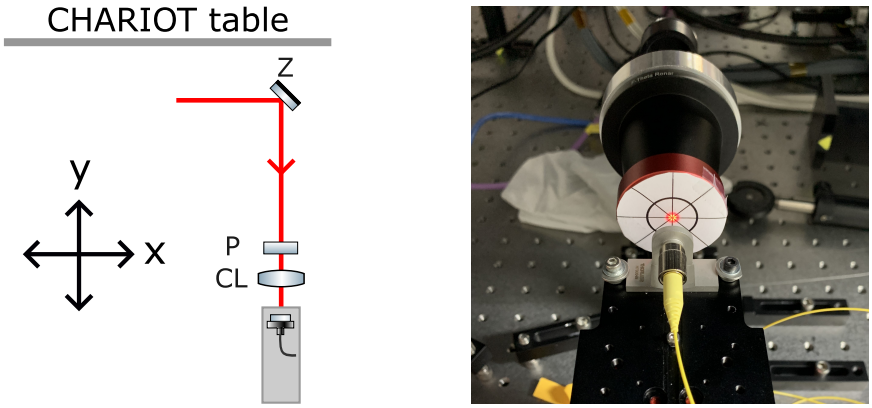

Figure 34: Left: The fiber-coupling part of the CHARIOT layout is depicted. The back-injected red laser on the Luminos positioner can be used to center the coupling lens CL with the paper target on the back cap.

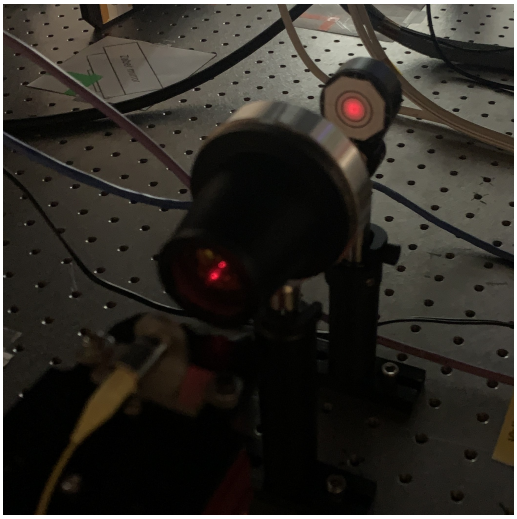

Figure 35: The back-injected red laser passes through the lens and can be seen on a target in front of the lens.

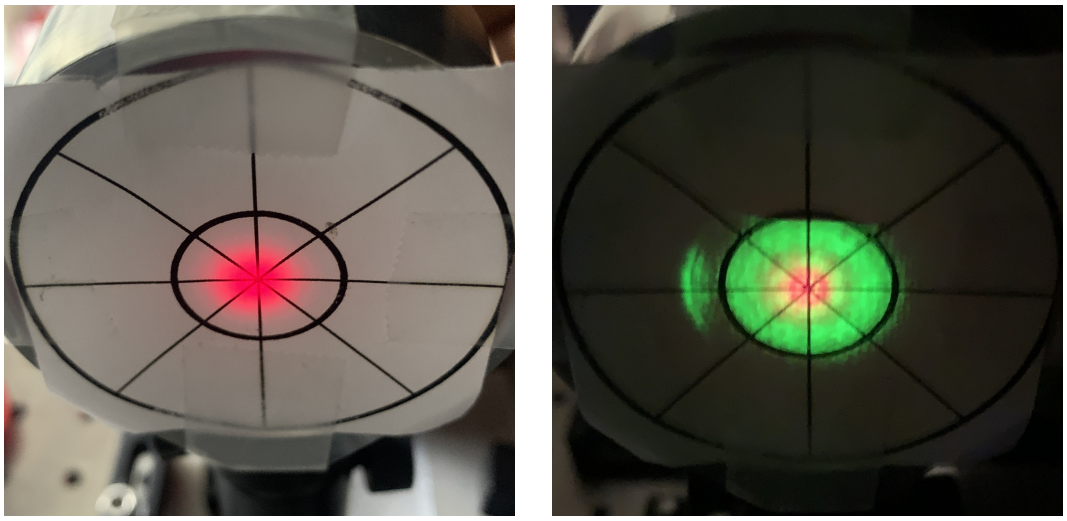

Figure 36: Both images show the paper target on an empty lens holder put in front of the lens CL. On the left, the back injected red laser is shown and on the right the overlap of the back-injected red laser overlapped with the green CHARA laser. The x-position needs to be corrected until the back-injected red laser is centered on the target at the back cap while the green CHARA laser is centered on the target in front of the focusing lens CL as seen on the right. The overlap of both lasers allows to correct the x-position and the angle (rotation) of the lens CL.

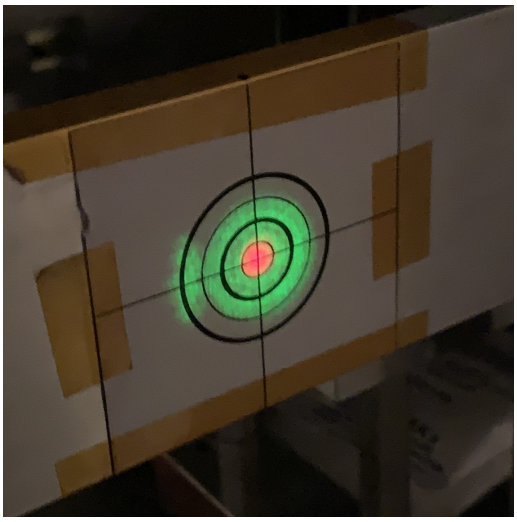

Figure 37: Overlap of the green CHARA laser and the back-injected red laser at the position of the CHARIOT front target. The red laser is centered along the complete beam path with the center of the green CHARA laser while keeping the same size. Thus, the lens is at the correct back focal length of 18.36 mm to the fiber-holder on top of the Luminos positioner. The overlap of both lasers can be checked by holding a paper card into the beam path at different positions throughout the complete setup to check the alignment of all components and the collimation of the back-injected red laser.

Fig. 37. Another way to check the overlap of both lasers and the collimation of the back-injected red laser is to use a paper card placed into the beam path at different positions. Note that in principle, the travel range of the Luminos positioner should be large enough to correct the distance between lens and fiber for the optimization of fiber coupling. For this specific lens CL (telecentric f-theta lens), angles in the incoming beam in front of the lens result in the output being shifted in the x-direction at the output of the CL. Now, the lens CL is aligned in the visible and fiber-coupling was achieved with a red laser injected into the STS. However, the fiber-coupling — especially the back focal length (distance of the lens to the fiber-holder) — is different in the NIR from the visible red laser. Therefore, the NIR light had to be recoupled once a sensitive K-band camera was available, for which the adjustment screws on the Luminos positioners could be used.

4.4.3.7 Polarization Controller In the precursor instruments FLUOR and JouFLU, polarization controllers (lithium niobate plates) were installed in the beam path to increase the fringe contrast. In interferometry, fringes will form between light in the same polarization state, but the resulting fringe pattern on the camera is a combination of both. Thus, if relative phase delay occurs between the polarization states, e.g. within the waveguides of the beam combiner, the fringe contrast decreases. Polarization control can improve the fringe contrast. Here, lithium niobate plates are included in the setup, which can be optimized to compensate the relative phase delays by adjusting their angle to the incoming beam. The process of optimizing the polarization controllers is described in [3] in detail. Until now, there was only little time to do an optimization of the polarization using the polarization controllers P as depicted in the CHARIOT layout in *Fig.* 13 and in *Fig.* 38. Nevertheless, the polarization controllers were put in place similar as in the previous setup. Their angle was optimized roughly with a few manual measurements with post-processed fringe analysis. More specifically, the orientation of the polarization controller P was changed by a small angle and the fringe pattern measured. After measuring three different angles of P, the position with the best fringe contrast was chosen. In a future research trip, the polarization optimization can be performed similar to the optimization for JouFLU (see [3]). Hence, enabling to optimize the fringe contrast for CHARIOT leading to an overall higher sensitivity of the instrument, which is important for future science measurements of dimmer targets. Important for on-sky observations is a suitable output imaging subsystem in CHARIOT, which is described in the next section.

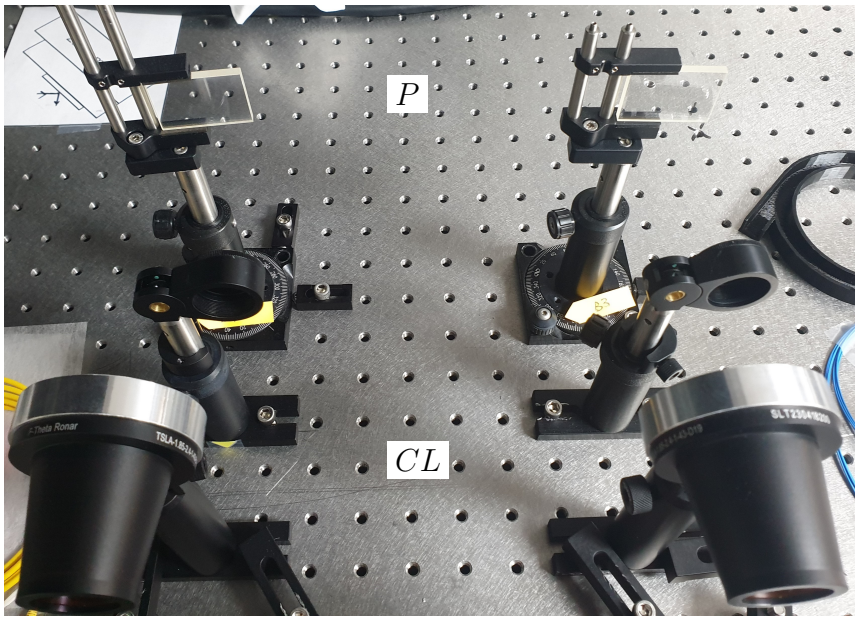

Figure 38: Polarization controllers P implemented into the beam path before fiber-coupling lens CL in both beams. During the last research trip, there was little time to optimize the polarization controllers for maximum fringe contrast. This is one tasks to be performed during future research trips to the CHARA Array.

4.4.4 CHARIOT — Output Imaging Subsystem

Currently, the output imaging subsystem of CHARIOT (see *Fig.* 39) consists of the fiber output after the beam combiner, followed by a two-lens system (collimating lens $L1$ and focusing lens $L2$), a wavelength filter $WLFW$ and a newly installed science camera (C-RED One Camera).

4.4.4.1 Lens System The two-lens system was aligned as described in the following:

1. Attach a red laser source to one of the beam combiner inputs.
2. Collimate the visible red laser beam with the collimating lens $L1$. This distance should be the focal length of the lens (see *Tab.* 5 for the component information).
3. Align the focusing lens $L2$ to the center of the collimated beam.
4. Ensure, that the focused laser spot is centered on the camera, while its cap is on. The distance between the focusing lens $L2$ and the position of the detector within the camera corresponds to the focal length of $L2$. See *Ch.* 4.5 for more information on the beam combiner.
5. Once the alignment is completed roughly in the visible, use NIR light to fine tune the alignment.

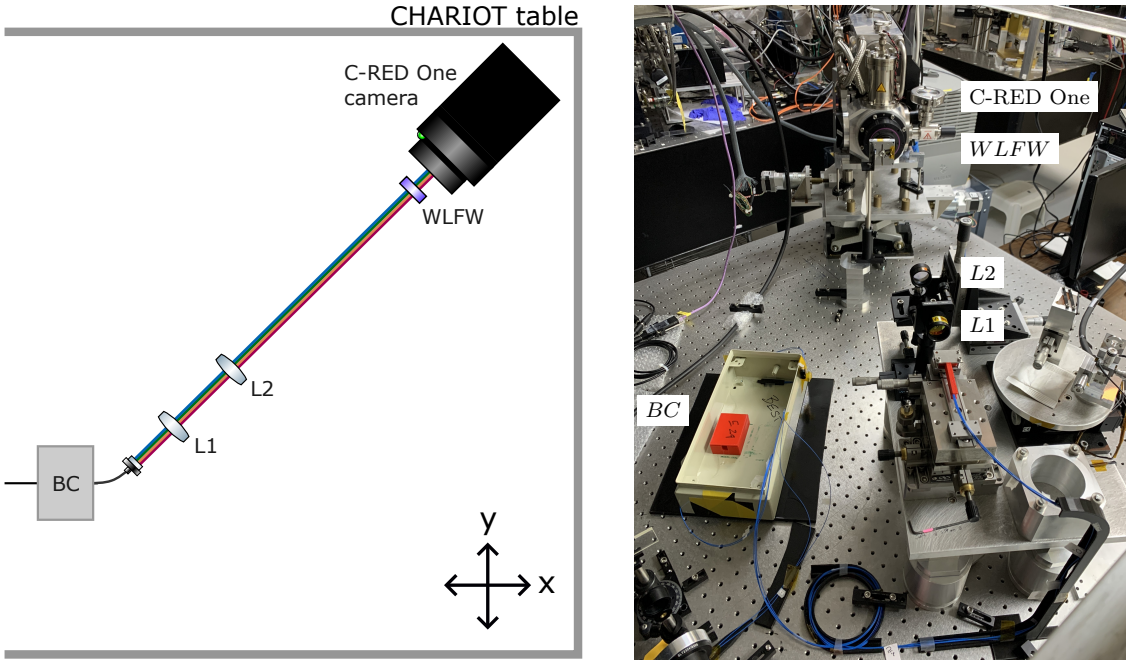

Figure 39: On the left, the layout of the imaging setup is shown. On the right, an image of the output imaging subsystem of CHARIOT is shown with labels for various components in this setup. Currently, the output imaging setup consists of the beam combiner with its output mounting followed by a collimating lens $L1$, a focusing lens $L2$ and a wavelength filter $WLFW$ before the light is imaged with the recently implemented science camera (C-RED One Camera). The output optics subsystem will be subject to futher redesign and optimization.

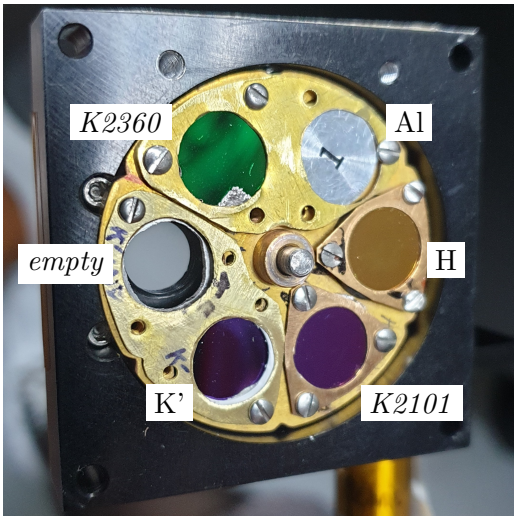

Figure 40: Filter wheel implemented in the CHARIOT output imaging subsystem including the filter K', *K2101*, H, Al, *K2360* and no filter denoted as *empty*. The filter properties are summarized in *Tab.* 11.

The two-lens system is a preliminary output optics design. The current output imaging subsystem shows loss of signal strength and aberrations for off-axis outputs. Currently, colleagues and project partners from the University of Cologne are investigating the source of these effects. A possible explanation could be that the signal is vignetted due to the baffle size of the science camera. Goal of the future lens system is a high signal throughput without introducing aberrations for all output beams of the currently implemented beam combiner (see *Ch.* 4.5). The implementation of a redesigned output imaging system is the highest priority for the next research trip. One part of this setup is the filter wheel, which is described below.

4.4.4.2 Wavelength Filter As discussed in *Ch.* 4.3, the bandwidth of the used wavelength filter $WLFW$ in the output imaging setup determines the coherence length (see *Eq.* 7). Generally, the larger the bandwidth of the used wavelength filter the shorter the coherence length of the signal, and thus, the shorter is the fringe packet. Especially during initial interference measurements and to make the fringe search easier, a narrower bandwidth is an advantage. The reason for that is that narrower bandwidths result in longer coherence lengths, and thus, in wider fringe packet. A wavelength filter wheel as seen in *Fig.* 40 including various wavelength filter from the precursor instruments could be reused and is implemented in CHARIOT. An overview of the filter properties from the filter wheel (see *Fig.* 40) is summarized in *Tab.* 11. So far, only the K'filter, no filter (*empty*) and the *K2101* filter were used. Parts of the information presented here is given in [3] — especially the K' filter is described there. In the case of the CHARIOT setup, a C-RED One

Table 11: Overview of the central wavelength λ and bandwidth $\Delta\lambda$ of the filters included in the current filter wheel. Note that throughout its use in different beam combiner instruments, some filters within the filter wheel were exchanged and the values given in the table should be used with precaution. For the filters written in cursive (*K2101* & *K2360*) only incomplete handwritten notes from 2006 were available whereas for the K'- and H- filter transmission curves exist (see *Fig.* 18 for the K'filter). The *empty* place in the filter wheel does not block any light from the combiner instrument, thus, all wavelength passing through the instrument can be detected in principle. The Aluminum (Al) "cold" stop blocks all science light leaving only a background emission to be detected. Information presented here is partly given in [3].

Filter Type	Central Wavelength λ_c	Bandwidth $\Delta\lambda$
K'	$2.16\,\mu$m	$0.32\,\mu\text{m} = 320\,\text{nm}$
K2101	$2.101\,\mu$m	$0.06\,\mu\text{m} = 60\,\text{nm}$
H	$1.66\,\mu$m	$0.30\,\mu\text{m} = 300\,\text{nm}$
Al — "cold" stop	/	/
K2360	$2.360\,\mu$m	unknown
empty — all detectable wavelengths	–	–

Camera was implemented recently and is introduced briefly in the following section.

4.4.4.3 C-RED One Science Camera *Fig.* 41 shows the cryogenically cooled C-RED One camera by FirstLight — now part of Oxford Instruments — ultra high-speed 320×256 electron Avalanche Photodiode (e-APD) array consisting of Mercury Cadmium Telluride (MCT) semiconductor materials. According to the data sheet, the C-RED One camera in the f/20-baffle K-band configuration, as it is implemented in the CHARIOT setup, enables measurements in the wavelength range of $\lambda = (0.8 - 2.43)\,\mu$m including the J-, H- and K-bands (see *Ch.* 1 and *Tab.* 1 for information about astronomical transmission bands). The camera achieves sub-electron read-out noise, dark noise with a flat quantum efficiency of $> 60\%$ at 100 K for $\lambda = (0.1.1 - 2.4)\,\mu$m as well as a maximum full frame single readout speed of 3500 Frames Per Second (FPS). The C-RED One camera is implemented in several beam combiner instruments at CHARA due to its low noise and high sensitivity properties. The camera was used for alignment of the output optics and to observe interference fringes.

As stated above, the output imaging subsystem is a work in progress and will be improved during the next research trip, which is planned for October 2024. One part of the output imaging subsystem and heart of the CHARIOT setup is the fiber-connectorized ultrafast laser-written beam combiner, which will be explained in the following.

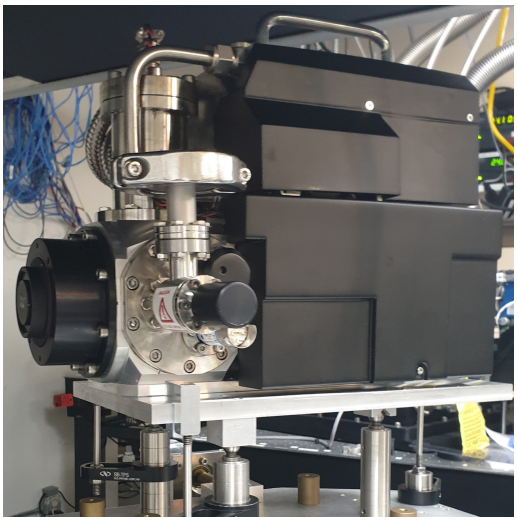

Figure 41: The cryogenically cooled C-RED One camera by FirstLight is shown, which is now part of Oxford Instruments.

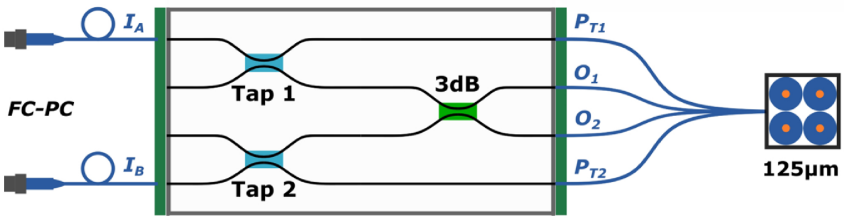

Figure 42: Schematic of an achromatic fiber-connectorized K-band ultrafast laser-written beam combiner [66, 67]. Such a component produced and characterized by project partners as presented in [66] is implemented in the 2-Beam CHARIOT setup. It comprises two inputs I_A and I_B and four outputs, which can be distinguished into two interferometric outputs O_1 and O_2 as well as two photometric outputs P_{T1} and P_{T2}. The four outputs are arranged in a rectangular shape. The image is adapted and taken from [66].

4.5 Fiber-Connectorized Beam Combiner

A concise description of the fiber-coupled K-band ultrafast laser chip-based beam combiner implemented in the 2-beam CHARIOT setup is provided in this chapter. More detailed description of the design, production and characterization can be found in [66]. This beam combiner was meant to replace the fiber-combiner (called "MONA" [3, 62]) in the JouFLU instrument at the CHARA Array. Earlier development stages of the beam combiner are presented in [67]. Implemented into the 2-beam CHARIOT setup (see *Fig.* 17) is such a component as schematically presented in *Fig.* 42. The image is adapted and taken from [66]. The used beam combiner was fabricated by a research group at the Heriot-Watt University, and is an achromatic fiber-connectorized K-band ultrafast laser-written beam combiner [66, 67]. The technique of the ULI for writing integrated-optics beam combiner chips is discussed in more detail in *Ch.* 5.3. The beam combiner is written in Infrasil Glass

(IG) and comprises two inputs I_A and I_B and four outputs distinguishable into two interferometric outputs O_1 and O_2 as well as two photometric outputs P_{T1} and P_{T2}. The photometric outputs can be used to calibrate the interferometric outputs. The four output fibers are arranged in a rectangular shape. In the first part of the integrated-optics beam combiner chip are so-called *taps*, which split the light 75:25, so that most of the light (75% each) is used for the interferometric overlap and 25% of the incoming light goes straight to the photometric outputs. The 3 dB-coupling structure in the chip splits the light roughly 50:50, so that there is ideally a balanced overlap of the incoming light. Please refer to [66, 67] for a more detailed discussion of the splitting ratios of the beam combiner. The authors characterized for several 17 mm long straight single-mode waveguide an insertion loss of ~ 1.1 dB for wavelengths between $\lambda = 2.0\,\mu$m and $\lambda = 2.3\,\mu$m [66]. For the beam combiner presented in [66] a visibility contrast of $> 80\%$ was measured. The work on the CHARIOT setup and the performance of the fiber-connectorized K-band ULI-written beam combiner can be verified in two milestones: lab and on-sky fringes, which will be discussed in the next section.

4.6 Verification of the 2-Beam CHARIOT Setup

In the previous chapters, the planned 4-beam and aligned 2-beam CHARIOT setup was introduced highlighting the importance of compensating the OPD between both beam paths before it is possible to interfere the light in the K-band fiber-connectorized ULI-written beam combiner and to record fringes with the output imaging setup. Achieving interference fringes in the 2-beam CHARIOT setup is an easy way to verify the corrected OPD and its functionality as a future beam combination instrument. This verification can be split in two milestones. First, interference fringes with a lab source in a controlled environment should be accomplished before reaching for the second milestone of measuring fringes of various bright stars in on-sky tests in an interferometric array environment including effects such as atmospheric turbulences, wind and humidity. Both milestones were successfully accomplished and are discussed in this chapter.

4.6.1 Lab Verification

For accomplishing the first milestone regarding the verification of the 2-beam CHARIOT setup, the STS with the Halogen lamp for K-band light (see *Ch.* 3.3.2) was utilized to form fringes in a controlled laboratory environment. At that point, the new software for the C-RED One camera and the JouFLU software was not yet adapted and combined to suit the new CHARIOT setup. Therefore, the static stage in beam $B3$ was moved individually in steps smaller than the coherence length via

the manufacturer's software in order to scan for temporal interference fringes. At a relatively small offset of $\sim 2.4\,\mathrm{mm}$ from the central position of the static stage the central white light fringe was found. Thus, due to the double pass introduced by the mirrors $M1$ and $M2$ on the static stage, the path difference between $B3$ and $B4$ is $\sim 4.8\,\mathrm{mm}$. Hence, the OPD between $B3$ and $B4$ is not even a thousandth of their total beam path length of about $\sim 5\,\mathrm{m}$, indicating a precise alignment of both beams according to the planned CHARIOT layout as seen in *Fig.* 13. At the start, to make the search for the OPD offset easier, the *K2101* filter with the narrowest bandwidth $\Delta\lambda$ was chosen, since this results in the longest coherence length l_{coh}, see *Eq.* 7 in *Ch.* 4.3. See *Tab.* 11 in *Ch.* 4.4.4.2 of the filters, which is discussed in the next part.

4.6.1.1 Coherence Lengths Measurements for Different Filters One of the first measurements to characterize the system was generating interferograms using different filters in the K-band. In general, the inverse influence of bandwidth size on the coherence length can be directly measured by generating interference fringes with different filters. Once the OPD correction was verified and the OPD offset found, the static stage was used to achieve fringes for three different filters $WLFW$, namely for the smallest known filter *K2101*, the K'-filter for which a transmission curve can be found in *Fig.* 18 and the longest possible bandwidth achieved with no filter through the *empty* filter wheel spot. While the STS emits light over a very broad wavelength range, only light that can couple into the beam combiner (and onto the camera) will contribute to the white light fringe. The bandwidth is thus not exactly known. It is determined by a combination of the light source, the optical components (e.g. lenses and fibers), which only transmit certain wavelengths, and the response of the camera.
Usually, in textbooks on stellar interferometry, the cosine fringe signal achieved for monochromatic light can be adapted for polychromatic sources. In this case, the cosine is integrated over a filter bandwidth, which is assumed to be a "top hat" function around $\lambda \pm \Delta\lambda/2$ [39]. Note that the definition of the bandwidth can be different for several textbooks as explained in *Ch.* 4.3. When integrating over such a "top hat" function, the resulting fringe signal A is given by

$$A \propto \cos(2\,\pi\,\delta/\lambda)\,\frac{\sin(\pi\delta/l_{\mathrm{coh}})}{\pi\delta/l_{\mathrm{coh}}} \tag{8}$$

where δ is the varied OPD, λ the central wavelength and $l_{\mathrm{coh}} = \lambda^2/\Delta\lambda$ the coherence length as defined as in *Eq.* 7. A more detailed derivation of the fringe signal A can be found in [39]. The cosine gives information of the fringes whereas the sinc function describes the envelope introduced by a finite filter bandwidth described as a "top

Table 12: Summary of the theoretically calculated coherence lengths with uncertainty estimations and the measured coherence lengths for the filters *K2101*, K' and no filter at the *empty* filer position. The measured coherence lengths are derived through the fitted sinc envelope function (see *Eq.* 8).

Filter	Central Wavelength λ in μm	Bandwidth $\Delta\lambda$ in nm	Calc. Coh. Length $l_{\mathrm{coh,\,calc}}$ in μm	Meas. Coh. Length $l_{\mathrm{coh,\,meas}}$ in μm
K2101	2.101 ± 0.010	60 ± 5	74 ± 6	66.7 ± 0.6
K'	2.160 ± 0.010	320 ± 5	14.58 ± 0.26	15.89 ± 0.09
empty	2.20 ± 0.20	400 ± 10	12.1 ± 2.2	10.21 ± 0.12

hat" function. In reality, the filter shape is not a perfect "top hat" function — typically a real filter has smoother edges, see e.g. *Fig.* 18 — thus, the resulting fringe pattern might deviate from the ideal sinc envelope function. Nonetheless, this model was utilized to fit the peaks of the fringes in the data sets for the three filters (*K2101*, K' and no filter). Further, for the data analysis, only one of the interferometric outputs is shown exemplary in this thesis. The other interferometric output experienced some nonlinearity, which is assumed to originate from a too high signal for which the C-RED One camera had a nonlinear response. The photometric outputs can be used for the following calibration known as photometric calibration. Generally, the interference signal of a monochromatic source can be described as

$$I = I_1 + I_2 + 2\sqrt{I_1\, I_2}\, \cos(2\,\pi\,\delta/\lambda)\,, \tag{9}$$

where I_1 and I_2 are the intensities of the interfered signals [34, 36, 39]. Thus, the measured fringe signal O_i for $i = 1, 2$ can be calibrated by applying

$$O_{i,\mathrm{cal}} = \frac{O_i - P_{T1} - P_{T2}}{2\sqrt{P_{T1}\, P_{T2}}}\,, \tag{10}$$

where P_{T1} and P_{T2} are the measured signals from the photometric outputs with a scaling factor. The fiber-connectorized K-band ULI-written beam combiner was designed to allow simultaneous photometric measurements in order to perform such a calibration. For the following data analysis, the signals consist of the sum of 7-by-7 pixels for each output. After the calibration was performed, there was still a small offset, which was corrected by subtracting the mean value of the data sets. Thus, the amplitude of the signal is given in arbitrary units (a.u.) and only the analyzed coherence length is of interest. For the plots in *Figs.* 43, 44 and 45, the fringe peaks depicted as dots in the plots were fitted to the sinc function of *Eq.* 8 and the cosine was omitted in the fit function. The resulting coherence lengths are summarized in *Tab.* 12. Note that for the filters *K2101* and K' smaller uncertainties were as-

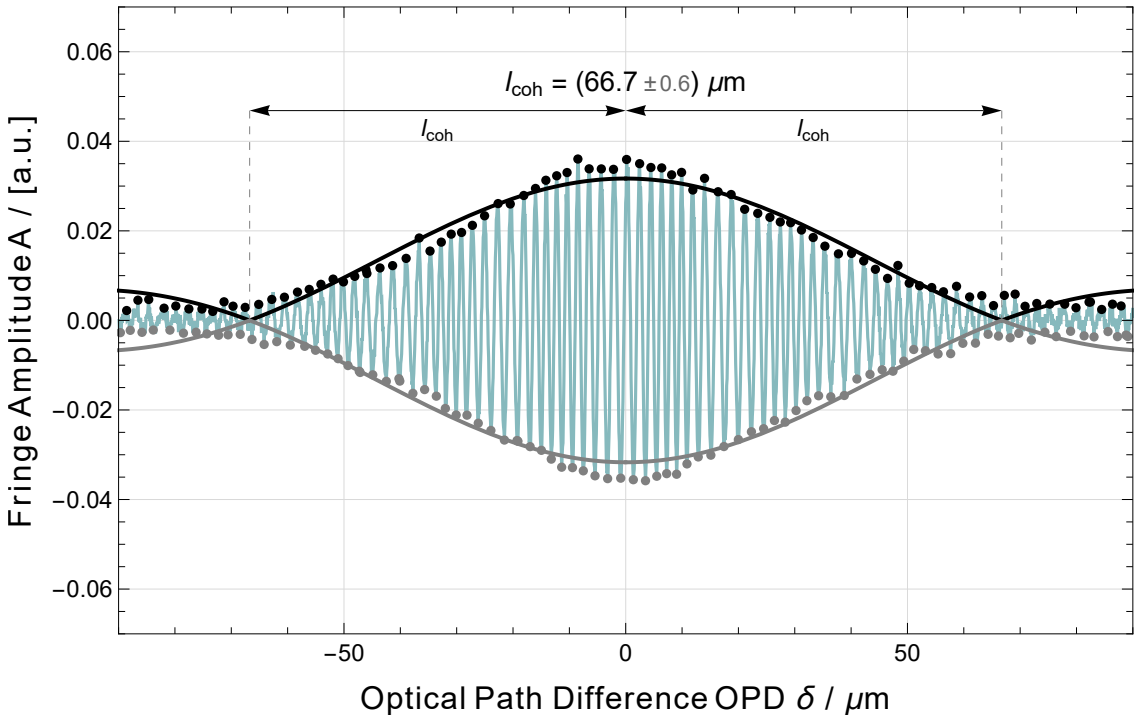

Figure 43: The fit for the *K2101* filter results in a coherence length of $l_{\mathrm{coh,\,meas}}^{K2101} = (66.7 \pm 0.6)\,\mu\mathrm{m}$. A theoretical coherence length with approximated uncertainties of $l_{\mathrm{coh,\,calc}}^{K2101} = (74 \pm 6)\,\mu\mathrm{m}$ can be calculated by assuming a central wavelength of $\lambda^{K2101} = (2.101 \pm 0.010)\,\mu\mathrm{m}$ and a bandwidth of $\Delta\lambda^{K2101} = (60 \pm 5)\,\mathrm{nm}$.

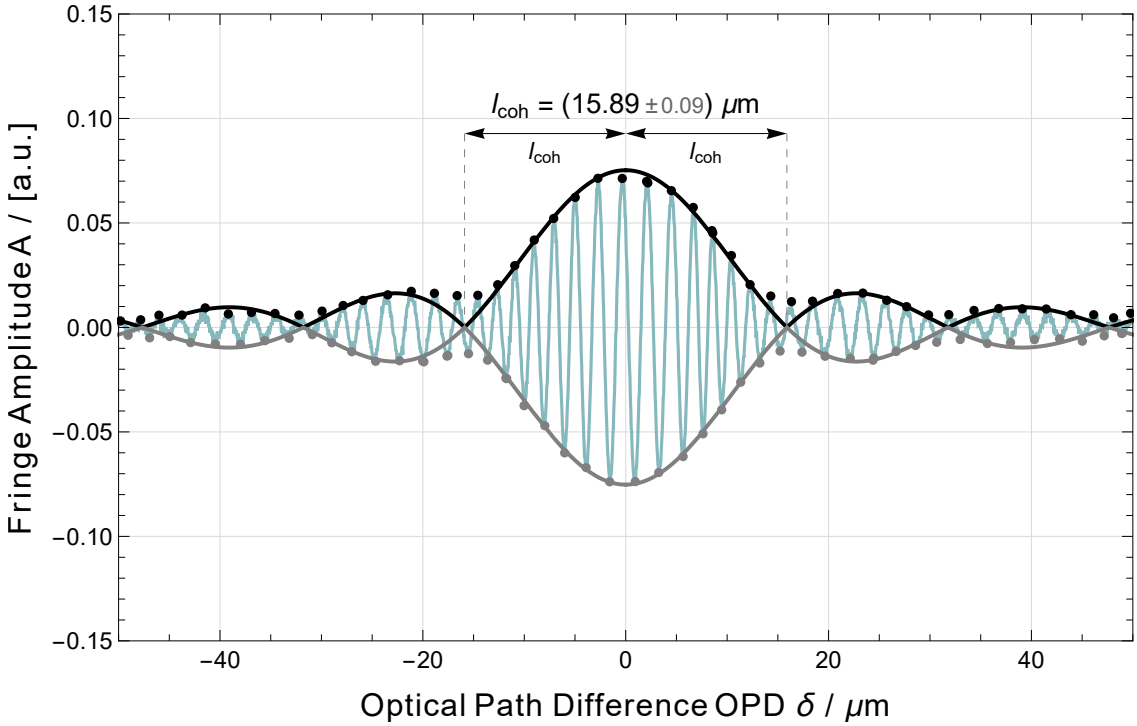

Figure 44: The fit for the K' filter results in a coherence length of $l_{\mathrm{coh,\,meas}}^{\mathrm{K'}} = (15.89 \pm 0.09)\,\mu\mathrm{m}$. A theoretical coherence length with approximated uncertainties of $l_{\mathrm{coh,\,calc}}^{\mathrm{K'}} = (14.58 \pm 0.26)\,\mu\mathrm{m}$ can be calculated by assuming a central wavelength of $\lambda^{\mathrm{K'}} = (2.160 \pm 0.010)\,\mu\mathrm{m}$ and a bandwidth of $\Delta\lambda^{\mathrm{K'}} = (320 \pm 5)\,\mathrm{nm}$.

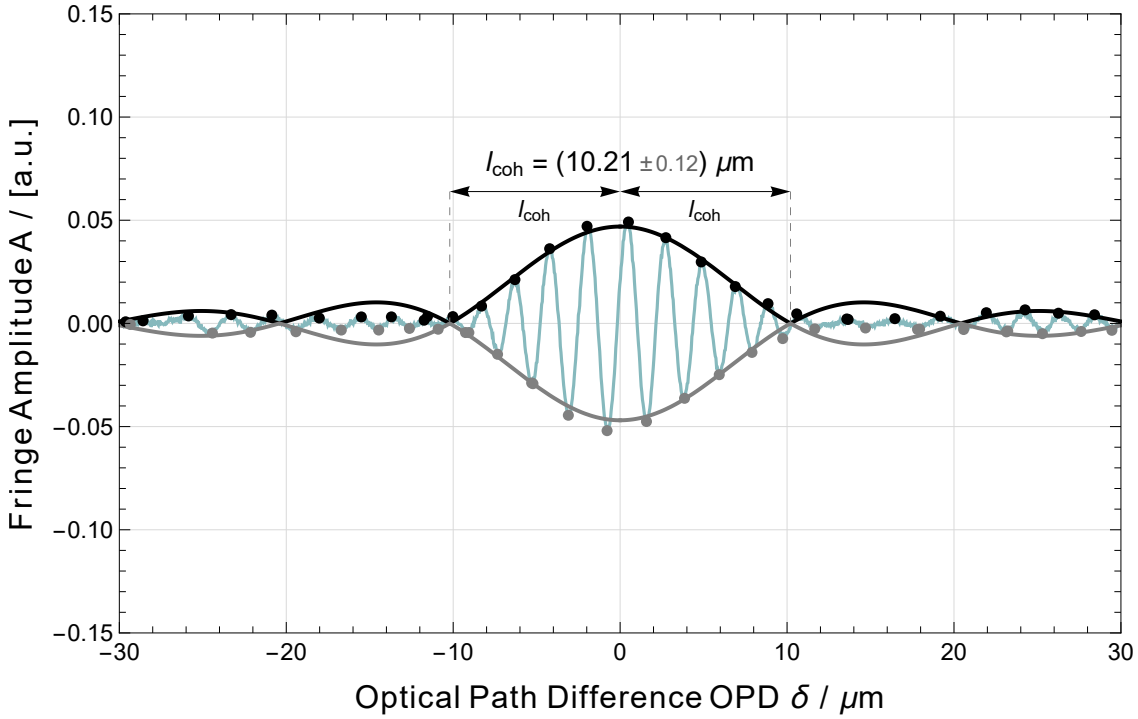

Figure 45: The fit for no filter results in a coherence length of $l^{\text{empty}}_{\text{coh, meas}} = (10.21 \pm 0.12)\,\mu$m. A theoretical coherence length with approximated uncertainties of $l^{empty}_{\text{coh, calc}} = (12.1 \pm 2.2)\,\mu$m can be calculated by assuming a central wavelength of $\lambda^{empty} = (2.20 \pm 0.20)\,\mu$m and a bandwidth of $\Delta\lambda^{empty} = (400 \pm 10)\,$nm.

sumed than for the *empty* filter spot because in their case the central wavelength and bandwidth was given. Therefore, only a relatively small uncertainty for the central wavelength of $\pm 0.010\,\mu$m and for the bandwidth of $\pm 5\,$nm was roughly estimated. For the *empty* filter spot, the observable wavelengths could be all wavelengths included in the NIR STS signal. However, the CHARIOT setup as well as the beam combiner is optimized for the K-band. Thus, for the calculated *empty* filter spot coherence length, the central wavelength is assumed to be within the K-band and the bandwidth the size of the K-band (see *Tab.* 1 for astronomical transmission bands). The central wavelength and bandwidth in this case is unknown, and thus a large uncertainty is assumed. For the central wavelength, the uncertainty of $\pm 0.20\,\mu$m includes the whole K-band, while the bandwidth uncertainty is approximated to be $\pm 10\,$nm. In order to get a more precise estimation of the central wavelength, bandwidth, and with that the coherence length for all filters, the filters should be spectrally analyzed in the future. Such a measurement would give information of the filter form, possibly allowing to specify a more fitting filter envelope function for the fringe pattern. Due to the large estimated uncertainty for $l^{empty}_{\text{coh, calc}}$, its value is the only one coinciding with the measured coherence length $l^{empty}_{\text{coh, meas}}$ within its uncertainties. For all cases in *Figs.* 43, 44 and 45, it is clear that the fitted sinc envelope function (see *Eq.* 8) does not perfectly fit the measured fringe pattern envelope. Es-

pecially in *Fig.* 44, it is clearly visible that the minimum between the lobes does not go to zero as it would be the case for a perfect "top hat" bandwidth function. The given uncertainties for the coherence lengths measurements through the fit function have relatively small uncertainties and do not take into account that the envelope function itself might not perfectly describe the polychromatic situation. Thus, the uncertainties should be taken with precaution and the values seen as an estimate of the coherence lengths. Nonetheless, in *Figs.* 43, 44 and 45 and their measured coherence lengths, it is obvious that with increasing filter width, the coherence length is reduced. Thus, depending on the application, different filters can be selected, e.g. small coherence lengths as for filter *K2101* can be beneficial when searching in a wide OPD area for the fringe signal. Whereas during on-sky tests, especially when reaching for dimmer science targets, a smaller bandwidth reduces the signal-to-noise factor and larger bandwidths are favorable. In the case of the available filter in CHARIOT, this would be the K' or *empty* filter spot, however, in on-sky tests having unknown filter properties would be an additional uncertainty. Thus, the K' filter was utilized as it is the only filter with known properties and a relatively large bandwidth allowing a larger signal-to-noise factor. In the future, characterizing the remaining filters in the filter wheel might provide useful information with respect to the system characterization beyond the K-band. After laboratory characterization and additional adjustments of e.g. the control software to achieve synchronization of the stages with the camera (not shown here), the next milestone is on-sky testing.

4.6.2 On-Sky Verfication

After successful lab fringes, the next milestone was achieving on-sky fringes. In 2024, the first on-sky fringes were successfully recorded with the achromatic fiber-connectorized K-band ultrafast laser-written beam combiner in the 2-beam CHARIOT setup at the CHARA Array with the 34 m $S1 - S2$ baseline (see *Ch.* 3) on May 2nd 2024. The traditional celebration of an instrument's first on-sky fringes is shown in *Fig.* 46. The first fringes were obtained on the bright star AW CVn (HD 120933) in standard weather conditions ($\sim$ 1 arcsecond seeing). Throughout the observation night, fringes down to a magnitude K$\sim$ 4 were recorded. This result was obtained by the NAIR-2 / APREXIS research team including the AIP, University of Cologne, the Heriot-Watt University, the Durham University with strong support from GSU CHARA staff. Note that during this engineering run only the interferometric outputs were imaged onto to C-RED One camera to avoid excessive clipping of the fiber output when all outputs were imaged off-axis. In order to reach the K$\sim$ 4 star, only one interferometric output was placed in the center of the optical axis of the output lens system to avoid further reduction of signal strength. An upgrade of the output imaging subsystem is planned for the next research trip to

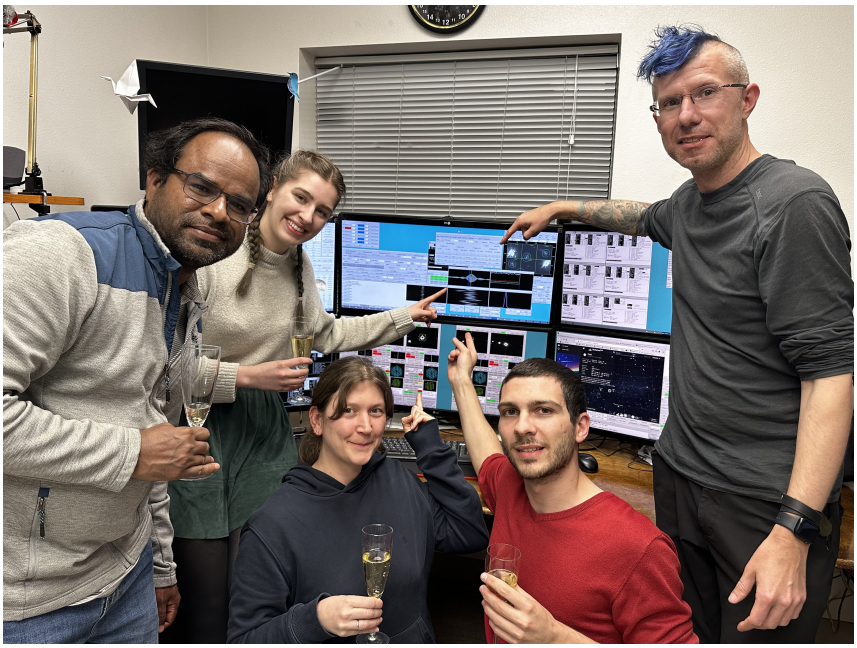

Figure 46: Celebrating the first on-sky fringes recorded with the achromatic fiber-connectorized K-band ULI beam combiner in the 2-beam CHARIOT setup at the CHARA Array on May 2nd 2024. From left to right: Narsireddy Anugu (GSU/CHARA), Alyssa V. Mayer (AIP), Aline N. Dinkelaker (AIP), Kévin Barjot (University of Cologne), and Nicholas J. Scott (GSU/CHARA). Image credit: Gail Schaefer (GSU/CHARA).

enable simultaneous measurements of all four beam combiner outputs, which will be tested again in on-sky experiments.

The work completed as part of this thesis included providing support for the planning of the 4-beam and optical alignment of the 2-beam redirection subsystem. Furthermore, the fiber-coupling was achieved with a visible red laser and later in the NIR. Additional tasks included the alignment of the current output imaging subsystem and various measurements for the characterization of the setup and the C-RED One camera. These efforts collectively formed the basis for the successful laboratory and on-sky tests. The data analysis of the on-sky test is ongoing. A few results of CHARIOT were published during the SPIE Astronomical Telescopes + Instrumentation conference 2024 in Yokohama, Japan and can be found in [4, 5].
The objective of the CHARIOT project is twofold. Initially, the goal is to validate the existing beam combiner through on-sky tests. Subsequently, CHARIOT is meant to be a future instrument for testing astrophotonic beam combiners in a real interferometric array environment. Such on-sky experiments are crucial for developing novel astrophotonics. An introduction to astrophotonics, different types of chip-based beam combiners as well as a description of the ULI technique can be found in the next chapter.

5 Astrophotonic Beam Combiners

The CHARIOT setup aims to provide a testbed for astrophotonic components, especially beam combiners, such as the ULI-fabricated beam combiner from the NAIR-2 / APREXIS project. At AIP, preparations are currently taking place for the manufacturing of waveguides with ULI, with the future goal to produce beam combiners at AIP. For this thesis, first steps were taken to test the fabrication system. This chapter will provide a brief overview of astrophotonics in general, with a focus on photonic beam combiners. The method of ULI is presented in *Ch.* 5.3, and laboratory results of the tests with the ULI System at AIP are presented in *Ch.* 6.

5.1 Photonics in Astronomy

The term "astrophotonics" describes photonic technologies developed for astronomy, more specifically for implementation in astronomical instruments, which can be used at telescopes or interferometric arrays. Analogous to electronics, which manipulates electric charge, photonics manipulate photons, e.g. guide, split, diffract, or filter light [72]. Astrophotonic technologies have been developed for the past 20 years; a book describing the principles of this technology can be found in [72]. In addition, there is a range of literature that provides an overview of the broad topic, such as [5, 73, 74], which were consulted for this chapter. Usually in astronomical instruments, bulky optics are utilized, such as mirrors for beam redirection, lenses for focusing and collimation, diffraction gratings or filters. These kinds of components take up a lot of space on optical tables and are sensitive to vibrations and temperature changes. Particularly in interferometric arrays, where light from multiple telescopes is redirected and combined, free-space beam combiners with bulky optics grow enormously in size with the number of incoming telescope beams. As previously discussed in *Ch.* 2.6 the number of measurable baselines and thus the required beam combinations increases as $\frac{1}{2}N(N-1)$ for an interferometric array with N telescopes [34]. Hence, reducing the size as well as increasing the stability of various parts of astronomical instruments is greatly desired. In addition to the goal of expanding interferometric arrays to include more telescopes, ground-based interferometry aims to achieve $\sim$ km baselines in the future. This is planned for the CHARA Array, where initial efforts include a mobile fiber-based 7th telescope [75, 76]. Furthermore, photonic solutions for nulling interferometry are developed, where light from a bright host star is destructively interfered to enable off-axis observations of faint objects such as exoplanets [5]. IO beam combiners usually have a small footprint on the scale of a few cm. Generally, astrophotonic devices are applicable along the entire beam path from incoming wavefront to beam combination as schemati-

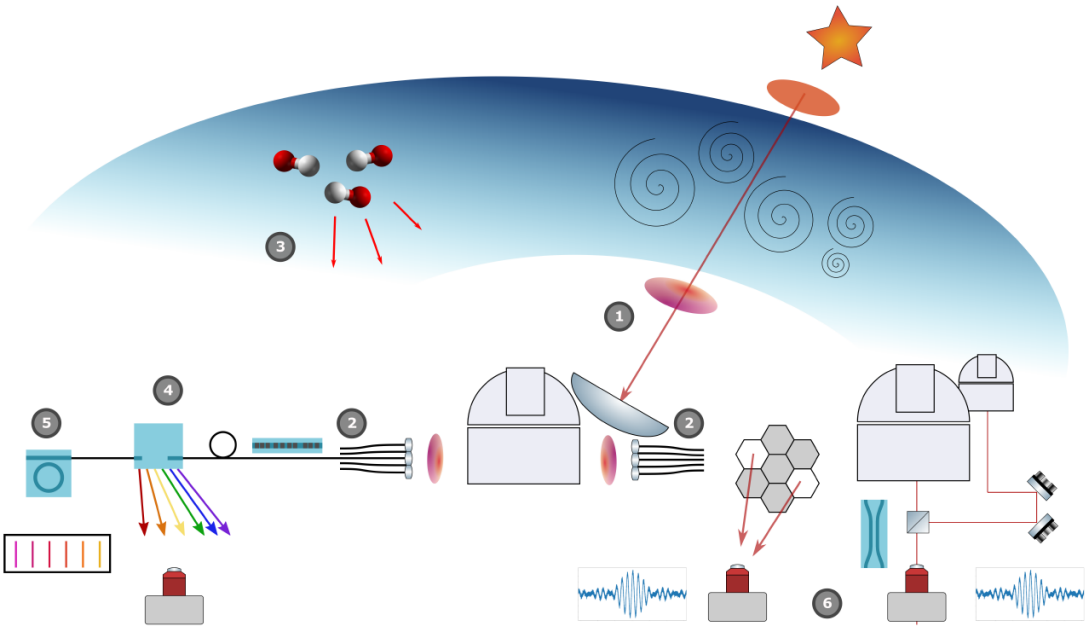

Figure 47: Overview of astrophotonic devices implemented along the entire beam path from incoming wavefront to beam combination. Schematically depicted are (1) atmospheric turbulences, (2) photonic lanterns and remappers, (3) filters for the emission lines of OH atoms, (4) spectrographs, (5) frequency references, and (6) beam combiners for interferometry. This image is taken from [5].

cally depicted in *Fig.* 47. Besides interferometric arrays, large single telescopes such as the future $\sim 39\,\mathrm{m}$ ESOs ELT [6] can benefit greatly from various novel astrophotonic devices. For example, the use of photonic lanterns (see **(2)** in *Fig.* 47) can increase the efficiency of collecting starlight within a large single telescope.

As discussed in *Ch.* 2.5, it is crucial to compensate the turbulence effects from the Earth's atmosphere. These turbulences are depicted in **(1)** and can be compensated with AO. In the following, some of the main astrophotonic components will be briefly described, to give an idea of the working principles and capabilities of astrophotonics. *Fig.* 47 shows examples of potential applications of astrophotonic components. Directly after the light is collected by an aperture, the light can be effectively collected with an astrophotonic component called a photonic lantern as shown in **(2)**, which was developed for multimode to single-mode conversion in astronomy. Photonic lanterns can be fabricated in different ways, e.g. by adiabatically tapering an array of single-mode fibers inside a capillary, which produces a multimode waveguide at the end. Thus, photonic lanterns enable conversion of single-mode light from several fibers into a single multimode output and vice versa [5, 72, 74]. Here, photonic lanterns are utilized to collect the incoming stellar signal as efficiently as possible with the multimode end and converting it into single-mode fiber outputs [5]. These single-mode fiber outputs are utilized for other astrophotonic devices, which make use of single-mode fibers and waveguides. One of these devices to introduce briefly

is a Fiber Bragg Grating (FBG) as depicted in **(3)** following the photonic lantern on the left. FBGs are aperiodic gratings written in single-mode fibers in order to suppress the bright and narrow emission lines from OH atoms in the Earth's atmosphere [5, 72, 74]. Further, single-mode fibers are used as inputs in so-called Arrayed Waveguide Gratings (AWGs) as shown as a symbol in **(4)**. AWGs are miniaturized spectrographs, which are fed by single-mode fibers and consist of a free propagation zone where the light spreads outs, followed by an array of curved waveguide of variable lengths, and another free propagation zone. Similar to conventional spectrographs, AWGs introduce a phase difference to the signal in order to create a spectrally dispersed signal [5, 72]. Next to the AWGs in *Fig.* 47, number **(5)** shows a ring resonator, which can be used to make a frequency comb, which emits light at a large number of evenly spaced frequencies. These frequencies can be stabilized using atomic references, which allows the use of frequency combs as precise frequency references for spectrographs. Such frequency combs with frequency spacings and parameters suitable for astronomy are known as astrocombs [5]. This concludes the brief descriptions of the astrophotonic components on the left side of *Fig.* 47. On the right side of the image, Aperture Masking Interferometry (AMI) is depicted in number **(6)**, which describes the technique of combining light from several sub-apertures within a single telescope in order to achieve higher angular resolutions. This technique is utilized in the Near-InfraRed Imager and Slitless Spectrograph (NIRISS) instrument of the JWST as the first infrared single-telescope interferometer in space [77–79]. With so-called pupil-remappers, light from sub-apertures of single telescopes can be collected with photonic devices to remap the outputs (i.e., to use waveguides in chips or fibers to guide the light in a controlled way and thus change the position of the output configuration) and combine them interferometrically [5]. Last but not least, there are several photonic devices for interferometric beam combination as schematically shown in **(7)** in *Fig.* 47. Beam combiner technology will be discussed in more detail in *Ch.* 5.2, including the GRAVITY beam combiner and the NAIR-2 / APREXIS beam combiner as examples. This aims to provide some context, to help understand the requirements for fabrication of beam combiners, as well as the requirements and the importance of a testbed such as CHARIOT.

There are different ways, how astrophotonic components are manufactured, either using photolithographic methods, or glass processing and ULI. The method of photolithography is the more mature method, as it has a longer heritage from manufacturing of photonic devices in the telecommunication sector. However, the photolithographic technique limits the fabrication to 2D structures. A previously designed mask is used to transfer a pattern to a substrate, which is placed on a "photoresist" and exposed to radiation followed by an etching and developing phase. [80]. The

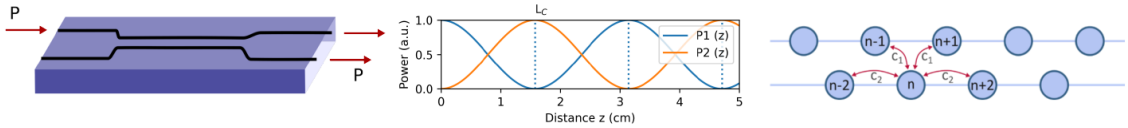

Figure 48: Left: Schematic of a directional coupler consisting of two inputs, an interaction region for evanescent coupling followed by two outputs. Center: This plots depicts the coupling rate between both waveguides depending on the length of the interaction zone. Right: The evanescent field of one waveguide extends in all dimensions and can couple into all neighboring waveguides. Thus, this technique of beam combination is not limited to 2D. Image is taken from [5].

fabrication with photolithography is commonly done by an external manufacturer for a fixed design, which hinders a flexible design change and possibly introduces higher costs and longer waiting times [5, 73]. An alternative method is ULI. Here, a pulsed laser is focused into a glass substrate allowing to change the refractive index of a glass substrate, and hence, creating 3D structures. A more detailed description of the ULI technique can be found in *Ch.* 5.3. In the following Section, different types and examples of astrophotonic beam combiners are presented.

5.2 Photonic Beam Combiner Types

In this section, different types of chip-based beam combiners and their working principles are introduced. First, directional couplers are explained, which form the foundation of photonic beam combination and are key to photonic beam combination. Secondly, ABCD pairwise beam combiner are discussed as implemented in the GRAVITY instrument at the VLTI [11], and finally Discrete Beam Combiners (DBCs), which might be specifically advantageous for combining larger numbers of telescope beams. Note that besides the presented chip-based beam combiner types, there are fiber combiners. A fiber combiner was implemented in the FLUOR [49, 62, 64] & JouFLU [3, 63] instrument, but those will not be presented in this thesis.

5.2.1 Directional Couplers

The building blocks for all types of astrophotonic beam combiners is evanescent coupling. It utilizes the extension of the electromagnetic field outside a waveguide, which is also known as evanescent field. If two waveguides are close enough, light from each waveguide can couple into the other. Directional couplers can be viewed as a building block for more complex astrophotonic beam combiner types, as they use evanescent coupling in one of its simplest forms. An example for a directional coupler is depicted in *Fig.* 48 on the left. It consists of two inputs, an interaction region for evanescent coupling and two outputs. In the interaction zone, both waveguides are brought close together, so that the evanescent field extending from each

waveguide can couple into the neighboring waveguide [5]. Depending on the length of said interaction zone, different splitting ratios can be achieved as depicted in the center plot of *Fig.* 48. Hence, if designed correctly, the two incoming beams can be combined in the interaction zone as it would be the case for a 50:50 beamsplitter. Directional couplers can be fabricated using lithographic methods or ULI. As the evanescent field extends in all dimensions outside the waveguide, it is possible to extend this design to use in 3D with more than two waveguides. As shown on the right in *Fig.* 48, the evanescent field of one waveguide can couple into all neighboring waveguides if they are close enough. Crucial for astronomical applications of directional couplers, is that the bend radius is chosen to ensure minimized losses due to stay light [5]. If a single directional coupler design is used, the phase information is derived solely by introducing a path delay within the coherence length in one of the incoming beams in order to create temporal fringes. Such a beam combination method is implemented in the 2-beam K-band CHARIOT setup (see *Ch.* 4.5). In reality, the design of directional couplers can be a bit more complex, e.g. including additional splitters for photometric taps, and waveguide detuning (i.e. different waveguide diameters in the interaction region) to increase achromaticity and enable broadband operation of the splitter. Furthermore, other beam combiner designs exist, which allow single shot extraction of information through simultaneous measurements of different outputs. Two types, namely the ABCD and the DBC beam combiner types, will be presented in the following.

5.2.2 ABCD Pairwise Beam Combiners

ABCD beam combiners allow extraction of the fringe in a single shot by monitoring 4 outputs for each pairwise combination, where light from the same input has been combined with different relative phase shifts. The most prominent example is the ABCD combiner in the GRAVITY instrument at the VLTI [11, 12]. The chip-based GRAVITY beam combiner has been photolithographically produced (and is therefore a planar beam combiner) and has 4 inputs and 24 outputs. In *Fig.* 49 is an image of the GRAVITY astrophotonic beam combiner chip itself at the top and a schematic of the GRAVITY chip at the bottom. In the schematic of the ABCD beam combiner chip at the bottom of *Fig.* 49 the principle of the beam combination is shown. First each telescope beam is split with a 33:66 splitter, and afterwards, the 66% splitting output is split two more times and the 33% once. Hence, all telescope inputs are split into 6 outputs with 16.5% of the initial starlight each. At specific points $\pi/2$ phase shifts are introduced in the beam path before beam combination in the X-couplers occurs. Thus, at the output of the beam combiner chip, each telescope combination (in total 6 baselines) has 4 outputs with different relative phase of 0, $\pi/2$, $3/2\,\pi$ and π. By measuring the intensity of all four phase shifted outputs

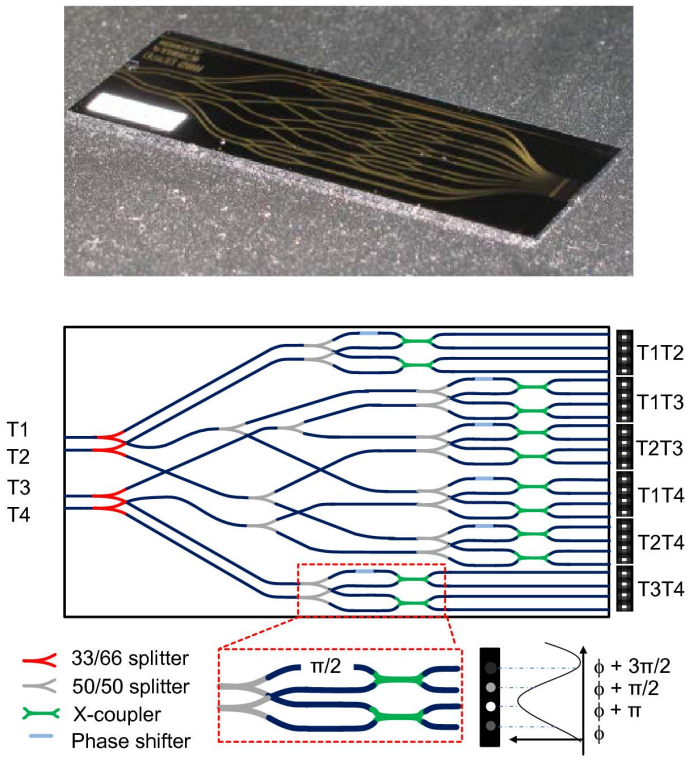

Figure 49: Top: Image of the astrophotonic 2D photolithographic ABCD pairwise beam combiner chip implemented into the GRAVITY instrument at the VLTI. Bottom: Schematic of the pairwise ABCD beam combiner. The beam combiner uses several Y-splitters to ensure equal intensity in all 6 splitting outputs for each telescope input. Relative phase shifts are introduced in the waveguides prior to beam combination in X-couplers. The beam combiner chip has 4 telescope inputs, resulting in 6 baselines. Due to the ABCD design, each baseline has 4 outputs, which results in a total of 24 outputs of the beam combiner. The 4 outputs per baseline have a relative phase difference of 0, $\pi/2$, $3/2\,\pi$ and π. This image is taken from [11].

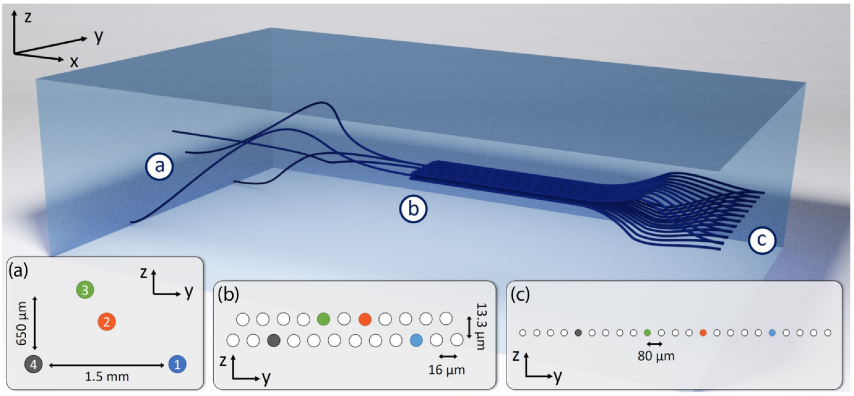

Figure 50: Schematic of a 4-beam 3D DBC design for the H-band including a pupil-remapper and a fan-out region. Within one photonic integrated-optics device, the inputs are remapped in (a), combined in the discrete beam combination zone in (b) and rearranged in a fan-out zone in order to achieve an in-line output format. This image is taken from [82].

for each baseline simultaneously, both amplitude and phase information of the complex visibility can be derived. In the case of this ABCD beam combination method no additional path delay is required to create fringes because of the relative phase shifted outputs. In earlier ABCD designs these phase shifts were not implemented and temporal fringes were required to measure the phase information [11]. Overall, the GRAVITY beam combiner has 24 outputs consisting of 4 phase-shifted outputs for each of the 6 baselines. It has a small footprint on the cm-scale with a length of 50 mm [81]. Such a leftover GRAVITY chip is implemented in the MYSTIC beam combiner instrument at CHARA (see *Ch.* 3.2.2). In addition, the CHARA/SPICA-FT utilizes a six telescope beam ABCD integrated optics beam combiner inspired by the GRAVITY fringe tracker [58] (see *Ch.* 3.2.4). Both the GRAVITY instrument at the VLTI and the MYSTIC instrument at CHARA achieved great results with the ABCD astrophotonic beam combiner chip. Contributions from the GRAVITY instrument at the VLTI lead to the 2020 Physics Nobel Prize as discussed in *Ch.* 2. However, for the combination of several telescopes, 2D beam combiners experience many unwanted cross-overs. In the following DBCs as an example for 3D beam combiners are described.

5.2.3 Discrete Beam Combiners

DBCs are 3D beam combiners, and thus, cross-overs and unwanted crosstalk can be avoided [73]. Above, the concept of evanescent coupling and its possible application in 3D was briefly mentioned. One way to utilize the evanescent field to combine in 3D is accomplished in DBC designs. An example for a 4-beam DBC design for the H-band is shown in *Fig.* 50. The IO chip includes (a) an area for pupil-reformatting, (b) the DBC region, and (c) a zone to fan-out the outputs and rearrange them in an

in-line format [82]. The DBC region consists of two or more stacked layers horizontally shifted to achieve a zig-zag configuration, in which the extending evanescent field in one waveguide can couple into its neighboring waveguides [5, 82, 83]. Due to the use of only straight and parallel waveguides, cross-overs and bend-losses are intrinsically avoided. Similar to the above described simultaneous ABCD pairwise beam combination, DBCs do not require a variation in path length or the creation of temporal fringes. The location of a waveguide as well as the coupling strength into other waveguides influences the propagation of the input signals. Thus, the outputs include both amplitude and phase information of the complex visibility and can be derived through the transfer matrix [36, 83, 84]. The transfer matrix has to be calibrated first, but can then be applied during measurements to extract the complex visibility. A mathematical description is not scope of this thesis but can be found in [84]. The possibility of 3D structures, as well as the avoidance of bend losses and crossovers, makes DBCs a possible candidate for future astrophotonic beam combiner designs that combine light from numerous telescopes [5]; however, this design, like all others, comes with its own challenges in scaling for larger numbers of telescopes. Since DBCs make use of 3D structures, fabrication is currently only done using ULI.

Which type and which specific realization of beam combiner is used depends on the application, the wavelength, and the achievable performance. Developments on the field of beam combiners are still ongoing, where high light throughput, additional accessible wavelengths, broadband operation, and higher numbers of inputs are some of the development goals. The development of astrophotonic beam combiners can be fully advanced only by testing design concepts in laboratory and on-sky tests, as will be possible with the CHARIOT instrument.
In the following, the ULI technique is described as a theoretical background for the experimental work described in *Ch.* 6.

5.3 Ultrafast Laser Inscription (ULI)

The ULI technique is known by a variety of terms such as femtosecond laser direct writing, femtosecond laser micromachining, and all possible combinations of laser direct or waveguide writing and processing. This makes literature searches difficult, as different groups have used different terms to describe ULI over the years. ULI was first demonstrated in 1996 by Davis et al. [85] and Glezer et al. [86]. Although ULI is not yet as readily applicable to industry as planar 2D photolithographic techniques, it offers a number of advantages [87]. ULI is inherently more flexible than photolithography because it allows structures to be designed and written in

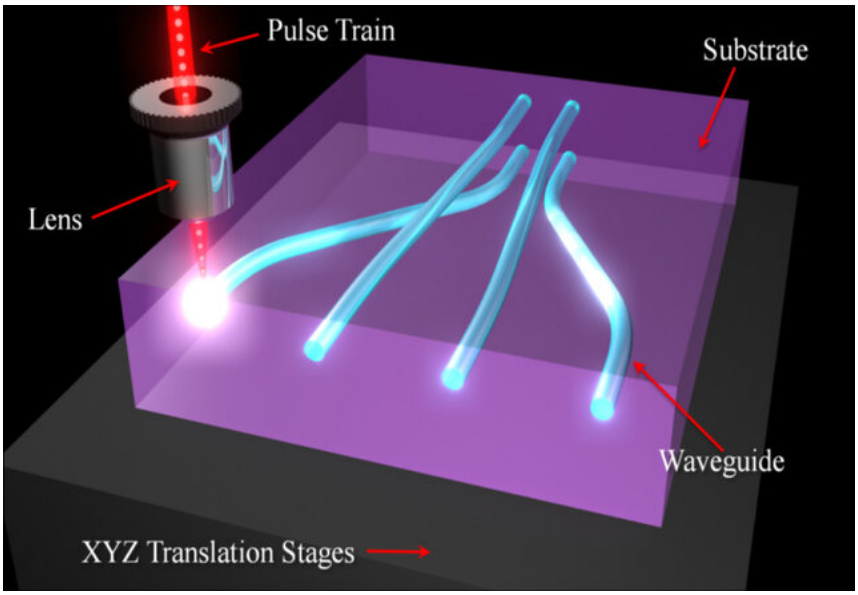

Figure 51: A laser with ultrashort pulses (usually with a duration of a few hundred femtoseconds) is focused into a glass substrate through a microscope objective or lens in order to permanently alter the substrate's refractive index locally. By moving the glass substrate placed onto a three-axis translational stage, 3D structures are fabricated [87–92]. The image is taken from [91].

3D without the need to first create a mask with a fixed design. Further, a ULI system can be placed and utilized in a common laboratory instead of a cleanroom environment [88]. Additionally, fabricating astrophotonics with ULI enables complex 3D waveguide structures, which are particularly advantageous when combining light from multiple telescopes. In this case, waveguide cross-overs and cross-talk is avoided, which occurs for planar 2D photolithographic beam combiner chips.
In this chapter, the ULI technique and different modification types are described before the Representative Net Fluence (RNF) is introduced as a figure-of-merit to compare the deposited energy for varying parameters within the large parameter space of ULI systems.

5.3.1 Technique

The technique of ULI is shown schematically in *Fig.* 51, where a laser with ultrashort laser pulses, usually with a duration of a few hundred femtoseconds, is focused into a glass substrate either through a microscope objective or a lens. In the focus area within the substrate, the refractive index of the material is permanently changed. By moving the glass substrate relative to the laser focus, waveguide structures can be produced. Note that waveguides are formed by structures within a material with different refractive indices. In order to guide light within a structure, this structure must have a higher refractive index n_{str} than the surrounding material n_{mat}. Thus, waveguides require a positive refractive index difference

$\Delta n = n_{\mathrm{str}} - n_{\mathrm{mat}} > 0$ [5]. The refractive index changes achieved with ULI are on the order of $\Delta n = 10^{-4} - 10^{-2}$ [89]. By moving the substrate placed on a three-axis translational stage, it is possible to fabricate 3D structures [87–92]. Refractive index changes with ULI are accomplished for a wide range of materials, such as glasses and crystals, but most commonly in fused silica and commercial available (alumino-) borosilicate glasses [87, 92]. Key principle of ULI is that the photon energy $h\nu$ of the laser is smaller than the energy band gap of the material E_g, where h is the Planck constant and ν the frequency of the laser. In other words, the wavelength of the laser must be within the transparency window of the material to avoid linear absorption of the focused laser light in the material [92]. While the ULI technique avoids linear absorption, the high peak intensities in the material due to the tight focusing of ultrafast laser pulses lead to nonlinear absorption processes such as multiphoton absorption and tunneling ionization [88–90, 92, 93]. How nonlinear absorption manifests as modification within the material depends strongly on the writing parameters, such as pulse energy E_p, writing speed v_s, pulse duration τ_p, pulse repetition rate R_p and spot diameter in the focus D_p, but also on the specific chemical composition of the glass substrate. Some possible modifications are refractive index changes due to melting, variations in the local structural composition of the material, or mechanical damage such as voids and microcracks [87–90, 92, 93]. Please refer to [87, 88, 90, 92, 93] for a more detailed theoretical description of the nonlinear absorption processes and the changes that occur in the material, which are not yet fully understood. Nevertheless, for the discussion of experimental results in *Ch.* 6, two types of modifications are defined in the next section to distinguish between smooth refractive index changes and modifications that cause optical damage.

5.3.2 Modification Types

As previously mentioned, the nonlinear energy deposition within the material causes different types of structural changes. Therefore, a clarification into type I and type II modifications was introduced [94]. By defining different modification types, it is possible to distinguish between a smooth refractive index change (type I) and optical damage created within the material (type II) [87, 89, 93, 95]. In *Fig.* 52, the type I and II modification is schematically shown as well as structure arrangements to achieve waveguides for light propagation. Further, in *Fig.* 52, transverse writing is shown in **(a)**, **(b)** and **(d)**, whereas longitudinal writing is depicted in **(c)**. Transverse writing describes a perpendicular writing direction to the laser beam direction whereas longitudinal writing is parallel to the direction of the laser beam [87, 89]. The multiscan technique [96] can be utilized to write larger waveguide structures as seen in *Fig.* 52 in **(a)** on the right and in **(d)**.

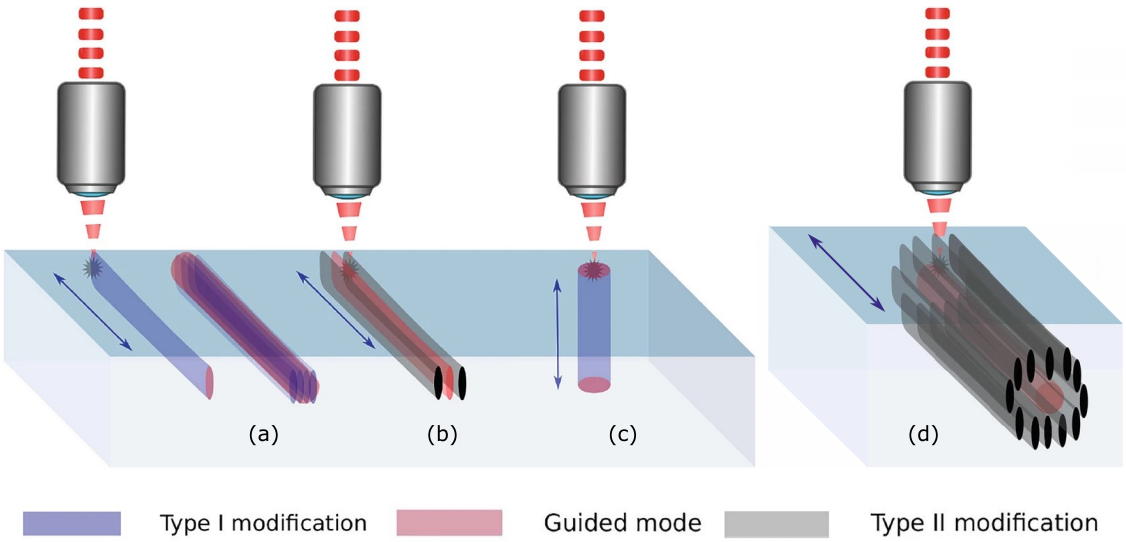

Figure 52: Schematic of ULI modification types and arrangements for waveguide writing. In **(a)** type I modification is depicted, and the creation of a large enough waveguide for light propagation by writing multiple lines separated by some distance. In **(b)** a waveguide is produced by writing two parallel lines with type II modification. In **(a)**, **(b)** and **(d)**, the waveguides are written perpendicular to the laser beam, known as transverse writing. Longitudinal writing is shown in **(c)**, which is parallel to the direction of the laser beam. Larger waveguides written with type II modification can be achieved with multiple writings in a circular arrangement as shown in **(d)**. These images are adapted and taken from [87].

Type I Modification describes the creation of a smooth refractive index change where no optical damages are produced within the material (see **(a)** in *Fig.* 52). According to [89, 93], either a positive or negative refractive index change is fabricated by type I modifications. Whereas in other literature [87, 95], type I modification is referred to the creation of light-guiding regions (positive refractive index change). In the context of this thesis, type I modification is referred to positive refractive index change. However, both definitions agree on a smooth refractive index change within the laser-irradiated region without the creation of any damages [87, 89, 93, 95]. Usually, this is the case for lower pulse energies E_p and for materials such as fused silica or commercial available borosilicate glasses [95]. This type of modification is difficult to achieve in crystals [89]. In order to create optical waveguides, the structures require a size of a few up to tens of μm [89]. Waveguides can be achieved by writing a number of slightly overlapping lines next to each other until the desired size of the waveguide is achieved. Such a multipass approach is schematically shown on the right in **(a)** in *Fig.* 52.

Type II Modification refers to a regime of light-matter interaction, which creates optical damages and voids caused by micro-explosions [89]. In this case, the damages occur as negative refractive index changes in the focus area of the laser

Table 13: Comparison of the thermal and athermal writing regime. Thermal means that the time between pulses T_{pulse} is shorter than the required time for heat dissipation τ_{heat}, whereas for the athermal regime the opposite is the case. Values are taken from [89].

Parameters	Athermal Regime	Thermal Regime
Repetition Rate R_p	low: few kHz	high: up to several MHz
Pulse Energy E_p	hundreds of nJ up to μJ	tens to hundreds of nJ
Numerical Aperture NA	low: ~ 0.4 to 0.7	high: ~ 0.6 to 1.4
Writing Speed v_s	tens of μm/s	$\sim$ mm/s
Heat Dissipation τ_{heat}	$T_{\text{pulse}} > \tau_{\text{heat}}$	$T_{\text{pulse}} < \tau_{\text{heat}}$

and a light-guiding stress field with positive refractive index change is created at some distance to the damages [87, 89, 93, 95]. Type II modification is shown in **(b)** and **(d)** in *Fig.* 52. By writing two parallel structures at some distance, it is possible to create a waveguide with positive refractive index change [89, 93] (see **(b)** in *Fig.* 52). Another way to create a light-guiding structure with type II modification is by writing multiple structures in a circular arrangement, which is shown in **(d)** in *Fig.* 52. Type II modification is achieved for higher pulse energies and can be achieved for a variety of materials including crystals [89].

Usually, type I modification is utilized to create waveguides for astrophotonic beam combination. Depending on the laser properties in the ULI setup, different writing regimes for type I modification can be defined. An overview of those writing regimes is given in the following.

5.3.3 Writing Regimes

In addition to the type I and type II regimes of laser-matter interaction, there exists different writing regimes, called **thermal** and **athermal**. Both writing regimes are compared in *Tab.* 13. Main difference between both regimes is whether the time between pulses $T_{\text{pulse}} = 1/R_p$, which is the inverse of the repetition rate R_p, is longer or shorter than the required time for the heat to dissipate τ_{heat} [89]. The latter is also known as the thermal diffusion time and is on the order of $\tau_{\text{heat}} \sim 1\,\mu$s, thus, the transition between both regimes is roughly at a repetition rate of $R_p \sim 1\,$MHz [88–90]. The terms thermal and athermal regimes are often exchangeable by high and low repetition rate writing regimes. For the athermal regime, the pulse-by-pulse material modification require slower writing speed v_s in order to achieve smooth waveguides [89]. In the thermal writing regime, heat is accumulated, and smooth waveguides achieved by a sequence of melting followed by rapid cooling. Hence, higher writing speeds are possible, and therefore, writing waveguide structures achieved

within a shorter time span [89]. The intermediate writing regime provides ideal writing parameters, in which high enough writing speeds v_s can be used for fast fabrication, while requiring moderate pulse energies E_p [88, 90]. Usually, Yb-based lasers operate in the intermediate regime. An example for an athermal, low repetition rate ULI system is an amplified Ti:sapphire system, whereas long cavity Ti:sapphire oscillators are used for thermal, high repetition rate ULI systems [88, 90].

Depending on the substrate material, different writing parameters are suitable. For pure fused silica, lower repetition rates between $1\,\text{kHz} \leq R_p \leq 100\,\text{kHz}$ and writing speeds up to a few mm/s were found to create smooth waveguides [92, 95]. Whereas for alumino-borosilicate glasses, such as Corning Eagle XG, Eagle2000, Schott AF32 or SchottBorofloat, higher repetition rate of 500 kHz to 5 MHz and writing speeds between 10 mm/s and 100 mm/s enabled waveguide formation [87, 92]. When discussing different writing regimes, it becomes clear that finding ideal parameters for a ULI system is difficult due to its large parameter space. In the next section, the parameter space and a suitable figure-of-merit — the RNF — is explained.

5.3.4 Representative Net Fluence (RNF) and the ULI Fabrication Parameter Space

In ULI, a wide range of parameters influences the outcome of the light-matter interaction within the substrate. A fixed set of parameters is defined by the ULI system itself, such as the laser type, its operating wavelength λ_L, the pulse duration τ_p and pulse repetition rate R_p. Depending on the ULI system, some of these parameters might be variable too. The Numerical Aperture (NA) of the microscope objective or lens is another important factor that defines the beam diameter D_p as twice the Gaussian beam waist ω_0 of the focused laser: $D_p = 2\,\omega_0$. Note that in the context of this thesis, the spot diameter of the focused laser refers to the Gaussian beam diameter in vacuum. The Gaussian beam waist ω_0 can be calculated in terms the NA according to

$$\omega_0 = \frac{\lambda_L}{\pi\, NA}\,, \tag{11}$$

where

$$NA = n \sin(\alpha)\,, \tag{12}$$

with n being the refractive index [87]. The focus spot of the laser beam is elongated in z-direction (direction of the laser beam). By calculating the Rayleigh length z_r

of the Gaussian laser beam as

$$z_r = \frac{\pi \omega_0^2}{\lambda_L}\,, \tag{13}$$

the spot diameter in air in z-direction $D_z = 2\,z_r$ can be calculated as twice the Rayleigh length z_r [87]. Note that in some references, the spot diameter and the elongation in z-direction is not defined as the $1/e^2$-criterium for beam waist ω_0 and Rayleigh length z_r, but as the FWHM of both [87]. In this thesis, the $1/e^2$ definitions are utilized. Thus, with *Eq.* 11 the focus spot area in air can be calculated as:

$$A = \pi \omega_0^2\,. \tag{14}$$

In a ULI system, the laser focus is not in air but in a dielectric material. Thus, the focus spot is elongated to a line accompanied by a decrease in the peak intensity because of the planar (flat and not curved) air-dielectric interface [87]. A detailed description of this effect can be found in [87]. This elongation depends on the focusing depth d_f. For most ULI systems, having a focusing depth of up to 200 μm does not reduce the maximum intensity by more than 10% [87]. Therefore, when the focusing depth does not exceed this value, the elongation due to the planar air-dielectric interface does not result in a significant reduction in the deposited intensity. Similarly, the focusing depth should not be chosen too close to the surface of the glass substrate in order to avoid edge effects due to uneven heat dissipation and surface ablation.
With the focus spot area A defined in *Eq.* 14, it is possible to introduce a figure-of-merit to describe the amount of energy deposited per area, the RNF or net fluence. The RNF can be calculated by

$$RNF = \frac{E_p\, N_p}{A}\,, \tag{15}$$

which is the pulse energy E_p multiplied by the number of pulses within the spot diameter N_p divided by the spot area A [97–100]. When writing multiple times over the same structure with the same parameter set, the total representative net fluence RNF_M is described by

$$RNF_M = RNF \cdot M\,, \tag{16}$$

where M is the total number of scans performed. The number of pulses within the spot diameter N_p for a non-zero writing speed v_s is given by

$$N_p^{v_s \neq 0} = \frac{D_p\, R_p}{v_s}\,, \tag{17}$$

as similarly defined in [98]. If the glass substrate is not translated during the writing process, the number of pulses (within the same spot, as $v_s = 0$) can be calculated with

$$N_p^{v_s=0} = R_p \, \tau_i \, , \tag{18}$$

where τ_i is the total illumination duration (burst). Sometimes in literature, the average laser power P_{ave} is given instead of the pulse energy E_p. Both quantities are related through:

$$P_{\text{ave}} = E_p \, R_p \, . \tag{19}$$

Note that both quantities are measured at the surface of the sample. The RNF can be used to compare different experimental runs with changed parameters. For example, the same RNF can be achieved by varying the writing speed v_s and the pulse energy E_p. Thus, the RNF can be used to discuss the influence of the individual parameters regarding the material modification even if it does not explain their influence on the non-linear light-matter interactions. Nonetheless, in the next chapter about the ULI system at AIP, the RNF is used as a figure-of-merit to simplify comparison between different parameter sets.

6 Fabrication of ULI-Written Waveguides at AIP

The Astrophotonics (innoFSPEC) group at AIP designs, fabricates and characterizes a wide range of astrophotonic components. See *Ch.* 5.1 for an overview of photonic components used in astronomy along the complete beam path. Until recently, competences at AIP in the field of beam combiners included design and characterization. A missing part in this development chain is the fabrication of waveguides in glass substrate using ULI. As an investment into the AIP as a site of astrophotonic competence in Germany, an ULI system was procured. The ULI system at AIP is meant to close the gap in the development chain of ULI-fabricated waveguides and beam combiners. Once a suitable parameter space for the ULI system is found, the full chain of design, fabrication and characterization can be completed in house. In order to achieve this goal, first a literature study of similar ULI systems is necessary, followed by experimentally exploring the parameter space with the given capabilities of the ULI system at AIP.
Note that during initial stages of work leading up to this thesis, the laser was found to require realignments by a manufacturer's technician. This delayed the work on the ULI system itself during which work on CHARIOT was completed. Thus, the time available to work with the ULI system was limited. Moreover, preliminary trials employed the use of coreless fibers, which inherently exhibit distinctive focusing, heat diffusion, and edge effects. However, since this thesis aims to investigate the parameter space for the fabrication of waveguides in glass substrates, the results of the fiber tests are not part of this thesis. It is noteworthy, that throughout the course of the ULI work at AIP, a number of fruitful discussions were held with Dr. Alexandre Mermillod-Blondin of the Max Born Institute (MBI) in Berlin-Adlershof. During these discussions, he proposed the utilization of phase contrast microscopy (see *Ch.* 6.2) as a means of investigating the fabricated refractive index changes. Future collaborations are planned between the AIP and the MBI. In the next section, the ULI system at AIP and its capabilities will be introduced briefly.

6.1 ULI System at AIP

The ULI system at AIP is the commercial system FemtoFBG by MKS (see *Fig.* 53), which can be utilized for writing waveguides in glass substrates but also for fabricating FBGs. It consists of a femtosecond laser (Spirit One SPOne-8-SHG) operable at one of two wavelengths, namely at 1040 nm or its second-harmonic (frequency-doubled) wavelength at 520 nm. Currently, the system is fixed for a wavelength of 520 nm. The parameters of the laser for a wavelength of 520 nm are summarized in *Tab.* 17 together with other specifications of the ULI system in *Ch.* A.2. The

Figure 53: The ULI system at AIP is the commercial system FemtoFBG by MKS consisting of a femtosecond laser (Spirit One SPOne-8-SHG) (left), and an optics system as well as translational stages for the x- and y-axis (Newport, XMS100) and the z-axis (Newport, VP-5ZA) for automated waveguide writing. The ULI system is additionally equipped with a z-axis piezo stage (Piezosystem Jena, MIPOS 500). The femtosecond laser light is redirected to a vertical optics system hidden by the orange plate in the right image on the left side. The pulsed laser light is focused by a microscope objective, which can be mounted above the translational stages visible in the right image. Note that in the right image no microscope objective is currently inserted.

Table 14: Specifications of the microscope objectives usable in the ULI system. The values are taken from the data sheets, except for the spot diameter D_p, which is calculated according to *Eqs.* 11 and 14.

Parameters	0.5 NA Objective	0.75 NA Objective
Manufacturer	Zeiss	Zeiss
Model	EC Plan-NEOFLUAR	EC Plan-NEOFLUAR
Article Number	440340-9904-000	440350-9903-000
Numerical Aperture NA	0.5 (20x)	0.75 (40x)
Spot Diameter D_p	0.66 μm	0.44 μm

vertical optics system is placed behind the orange metal plate in *Fig.* 53 on the right. It consists of various redirection mirrors, beam shaping optics and a power control via a $\lambda/2$ waveplate. Once the light exits the vertical optics system, it is redirected to a microscope objective. An empty microscope objective holder is visible in *Fig.* 53 on the right. Currently, there are two microscope objectives available to be placed into the holder in the ULI system. Their properties are summarized in *Tab.* 14. Note that the experimental results presented in this thesis were obtained solely with the 0.5 NA microscope objective (Zeiss, EC Plan-NEOFLUAR 20x) in order to avoid too tight focusing properties. The microscope objective is placed above the translational stages, which are made up of translational stages for the x- and y-axis (Newport, XMS100) and the z-axis (Newport, VP-5ZA) for automated waveguide writing. The ULI system is additionally equipped with a z-axis piezo

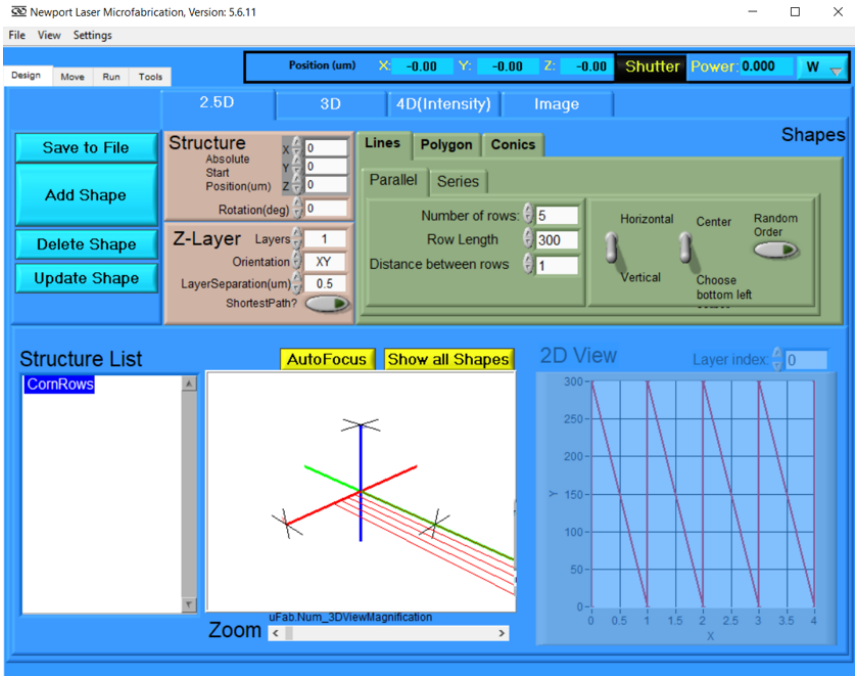

Figure 54: Screenshot of the "Design" tab in the μFAB software. In this software, the stages can be moved to align the sample, various designs can be made, loaded in via a file and started in the "Run" tab. The ULI system enables writing of simple line structures to complex structures (even images can be loaded).

stage (Piezosystem Jena, MIPOS 500) and a manual multi-axis tilt platform (Newport, M-37). An overview of the parameters of the translation stages can be found in *Tab.* 18 in *Ch.* A.2. Both, the laser and the translation stages can be controlled via software. A screenshot of the μFAB software used to write structures is shown in *Fig.* 54. It is possible to design and load files in the "Design" tab, while writing structures is done in the "Run" tab of the μFAB software. The software can be utilized to design simple or more complex structures. In principle, even images can be loaded and written into glass substrates. In the scope of this thesis, solely relatively simple line structures with different lengths, row numbers and repetitions were required to explore the parameter space of the system. The most important parameters for the ULI system at AIP are summarized in *Tab.* 15. For the experiments presented in this thesis, 1 cm × 2 cm × 1 mm borosilicate glass (Borofloat 33) samples by Schott were used. It should be noted that coupling light into and out of a ULI-written waveguide in a glass substrate is only possible if the facets are polished. For future tests, other materials and different glass dimensions will be ordered to enable an easier exchange and collaboration with the MBI and their ULI system. On top of the translation stages is a sample holder, which can fix fibers or microscope slides in place. For fabricating waveguides in smaller glass samples, a clamp is used together with some index matching gel to temporarily fix the smaller glass sample to a microscope slide. A preliminary sample holder was designed and

Table 15: Summary of important parameters of the ULI system at AIP limiting the explorable parameter space.

Parameters	ULI System at AIP
Laser Type	Yb-based
Wavelength λ_L	520 nm
Pulse Duration τ_p	260 fs
Repetition Rate R_p	500 kHz
Writing Speed v_s in x, y	$\leq$ 300 mm/s
Material	borosilicate samples
Substrate Name	Borofloat 33
Dimensions	1 cm × 2 cm × 1 mm
Manufacturer	Schott

3D printed, in which the smaller sample can be placed horizontally or vertically (see *Fig.* 55). Its design has to be adapted once new samples with different dimensions are ordered. A horizontal sample can be fixed with a metal clamp at the front of the 3D-printed sample holder in *Fig.* 55. At the back of the sample holder are two slits, which allow placing the sample vertically. The left slit in *Fig.* 55 allows the sample to be placed vertically along the long edge, while the right slit is for vertical placement along the short edge. Having both options (horizontal and vertical placement) allows looking at the top view, the side view and the cross-section or front view of the ULI-written structure under the phase contrast microscope. These view points are described in *Ch.* 6.4, where the experimental results are presented as well. In the next section, phase contrast microscopy is briefly introduced, which is used to qualitatively evaluate the written structures for varying parameter sets.

6.2 Phase Contrast Microscopy

Phase contrast microscopy is a frequently employed technique in biological research, particularly for the examination of objects with minimal to no intensity contrast, such as cells. A similar situation is present in structures made with ULI, where the transmission of light is hardly changed, making it difficult to see any structures using regular microscopes. ULI alters the refractive index within a transparent glass substrate, which modifies the phase of the light propagating through the written structures. Phase contrast microscopy transforms variations in phase into changes in amplitude, thus, making it a suitable technique to examine ULI-written structures. The principle layout of phase contrast microscopy is shown in *Fig.* 56 and explained in [101]. Differently to the commonly used bright-field microscopy, phase contrast microscopy utilizes an annular aperture in front of the condenser and a phase plate after the objective as shown in *Fig.* 56. For positive phase contrast mi-

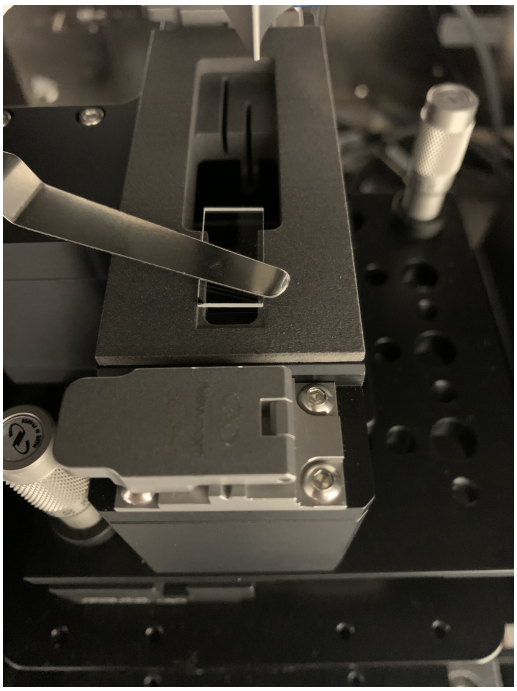

Figure 55: The image shows a first 3D-printed sample holder, which allows to fix a small glass sample horizontally and vertically. At the front, a horizontal sample can be fixed in place by a metal clamp, while at the back of the holder, it is possible to place a sample vertically. Adaptions and improvements of the sample holder are to be done once samples with different dimensions are purchased.

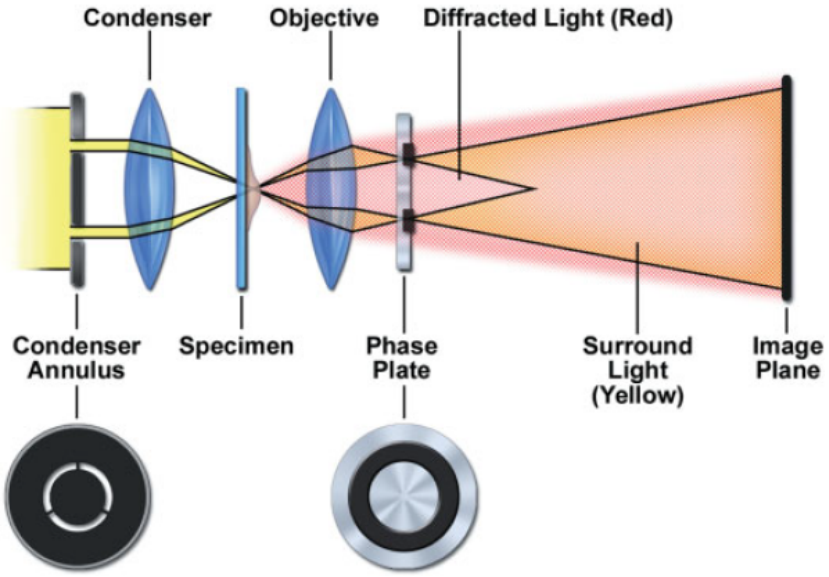

Figure 56: Schematic of the non-diffracted (surround wave) and the diffracted light beams within the phase contrast microscope. It consists of an annular aperture in front of the condenser and a phase plate after the objective. This image is taken from [101].

croscopy, the non-diffracted (surround) waves are shifted by $+\lambda/4$ in phase within the phase plate of the microscope setup. Diffracted beams experience a phase shift of $-\lambda/4$ within the phase contrast microscope. This results in an overall absolute phase difference of $\lambda/2$ enabling destructive interference in the image plane. Such an optical arrangement converts small phase changes in the sample into sensible intensity variations in the image plane. [101]. Positive phase contrast microscopy depicts higher refractive index regions as dark areas, while lower refractive index regions appear as bright areas.
An existing Axiovert A1 microscopy system at AIP has been updated to enable positive phase contrast microscopy. For that, an objective including a phase plate (Zeiss, 421351-9972-000, LD PN 20x/0, Korr Ph2 M27) and a condenser annulus (Zeiss, Ph 2/0,4) were added. The updated microscope for positive phase contrast microscopy is utilized for qualitatively analyzing ULI-written structures. For a structure written with type I modification, a positive refractive index change and with that a smooth dark area should be visible under the phase contrast microscope. In the case of negative refractive index changes, bright areas will be visible under the phase contrast microscope. Thus, for type II modifications on-axis damaged areas or negative refractive index changes are shown as bright regions, which are surrounded by dark positive refractive index change zones.
In order to find suitable starting values for the ULI system at AIP, literature discussing ULI systems with the same laser type were studied. An overview of this literature study and a range of possible starting values for the exploration of the parameter space is given in the following part.

6.3 Literature Study for Parameter Space

A literature study was performed with papers from a group at the Politecnico di Milano describing a ULI system with a similar laser to the one used at AIP. Scientists at the Politecnico di Milano already collaborated previously with the AIP in the context of beam combiner fabrication [83]. See *Tab.* 16 for a concise overview of the parameters for writing in (alumino-)borosilicate glass substrates from the literature study. The parameters for the ULI system at AIP are given in the same table, which were explored in initial experiments. The experimental results from the parameter space exploration are discussed in *Ch.* 6.4. Note that in [82, 83, 102, 103], the terms "alumino-borosilicate" and "borosilicate" are used interchangeably even when the exact same substrate material is used. Please refer to *Tab.* 19 in *Ch.* A.3 for a more detailed summary of the parameters from the literature study. It seems that the term "borosilicate" is used as a more generic term, while "alumino-borosilicate" is a more specific description for a substrate such as "Eagle XG". Furthermore, the available

Table 16: This table summarizes the ULI parameters from the literature study and from the initial parameter space exploration with the ULI system at AIP. A detailed overview of the literature parameters is given in *Tab.* 19 in *Ch.* A.3. In *Ch.* 6.4 the results from the parameter space exploration are discussed.

Parameters	Literature [82, 83, 102, 103] from Politecnico di Milano	ULI System at AIP
Laser Type	Yb:KYW	Yb-based
Wavelength λ_L [nm]	1030	520
Material Substrate Name Company	(alumino-)borosilicate Eagle XG or EAGLE2000 Corning	borosilicate Borofloat 33 Schott
Pulse Duration τ_p [fs]	300	260
Repetition Rate R_p [kHz]	1000	500
Numerical Aperture NA	0.6 (50x)	0.5 (20x)
Spot Diameter D_p [μm]	1.1	0.66
Writing Speed v_s [mm/s]	$20-40$	$10-50$
Number of Pulses $N_p^{v_s\neq 0}$	$27-55$	$8-33$
Pulse Energy E_p [nJ]	$330-620$	$30-1120$
Laser Power P_{ave} [mW]	$330-620$	$14-560$
RNF pro line $RNF_{M=1}$ [μJ/μm^2]	$10-20$	$0.7-27$
Total RNF RNF_M [μJ/μm^2]	$20-85$	$10-120$
Number of Scans M	$1-6$	$1-6$
Guided Wavelength λ_W [nm]	1550	/

substrate material at AIP is known under the name "Borofloat 33", which falls under the category of borosilicate glasses. According to data sheets available online for "Eagle XG" and "Borofloat 33", both materials have different compositions and properties. Hence, Eagle XG glass substrates will be purchased for the ULI system at AIP with the objective of establishing conditions that are more analogous to those described in the literature. Apart from the system at AIP, most ULI System have been setup by the groups themselves. Even commercially available systems are customizable, thus, a comparison to other ULI systems is inherently limited. It is therefore reasonable to narrow down the literature discussing ULI systems to systems with the same laser types (here, Yb-based lasers) and similar pulse durations τ_p. When comparing literature values to the parameters at AIP (see *Tab.* 16), it becomes clear that several values differ even though both laser types are Yb-based. This includes the laser wavelength λ_L, pulse duration τ_p, repetition rate R_p, the numerical aperture NA as well as the glass substrate material. In principle, the ULI system at AIP could achieve a closer wavelength to the literature, but for that a change in the setup is required. Nonetheless, the literature values presented in *Tab.* 16 were utilized as starting values for varying the writing speed v_s and pulse energy E_p within the same order of magnitude of the RNF (see the right column of *Tab.* 16). The results were qualitatively analyzed under the positive phase contrast microscope and are presented in the following section.

6.4 Experimental Results

Once the initial values were obtained from the literature, a series of writing speeds v_s and pulse energies E_p were investigated to achieve a comparable order of magnitude for the RNF as described in the literature. Structures can be written in horizontally or vertically placed glass substrates in order to view written structures from different points as depicted in *Fig.* 57. Different placements within the ULI system are required, because the working distance within the phase contrast microscope restricts the glass substrates to a flat (horizontal) placement. Thus, the structures under phase contrast microscope are viewed from an overhead perspective. The **Top View** can be observed when structures are written within a horizontal glass substrate. This case is depicted in blue in (a) and (b) in *Fig.* 57 and can be achieved in the front position of the sample holder seen in *Fig.* 55. In order to observe the **Cross-Section** or **Front View** depicted in red, and the **Side View** shown in green in *Fig.* 57, the sample must be placed vertically within the ULI system. Such a placement is achievable in the back of the sample holder as shown in *Fig.* 55. The three view points were investigated for the written single line structures discussed in *Ch.* 6.4.1. All experimentally tested parameter sets resulted

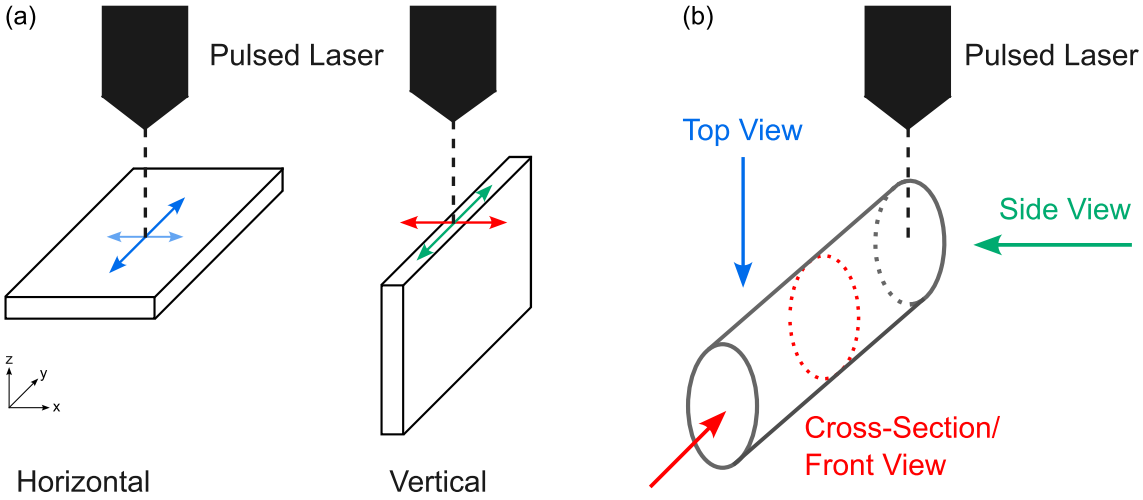

Figure 57: In (a), the writing directions and horizontal or vertical placement of glass substrates within the ULI system are illustrated. In *Fig.* 55 the sample holder is shown, allowing both placement options. The achievable view points are shown in the same colors in (b). The glass substrates have to be placed differently within the ULI system, because the glass plates can be placed solely horizontally (flat) into the phase contrast microscope. The **Top View** in blue is achieved for a horizontal glass substrate, while the **Cross-Section** or **Front View** in red, and the **Side View** in green require a vertical glass substrate placement.

in negative refractive index changes visible as bright areas under the phase contrast microscope. The on-axis bright negative refractive index changes are accompanied by off-axis positive refractive index changes noticeable as dark areas under the phase contrast microscope. Thus, all parameter sets lead to type II modification as defined in *Ch.* 5.3.2. This means, all written structures show bright on-axis negative refractive index changes, which are surrounded by stress fields of positive refractive index change. As a conclusion to this result, double line structures of various row distances d_R were tested in order to see if a sufficient structure with positive refractive index change can be created in between the double line structure. The results of this method are presented in *Ch.* 6.4.2. Furthermore, in *Ch.* A.4 additional phase contrast images can be found, which are not discussed in this chapter. The following section first discusses the top views of initial single line structure tests and performed pulse energy E_p ramps for different writing speeds v_s, followed by front and side view images of written structures.

6.4.1 Single Line Structures

When first starting to explore the parameter space of an ULI system, the written structures should be as simple as possible in order to reduce the amount of variable parameters. Thus, single line structures are a suitable choice, which can be repeated several times to increase the number of scans M. The most straightfor-

ward placement of the glass substrate within the ULI system is horizontal. Later, when a suitable parameter set is found, this placement is utilized for fabrication of waveguides and beam combiners.

6.4.1.1 Horizontal — Top View The initial values were the closest possible to the parameters utilized in the literature (see *Tab.* 16). In *Fig.* 58, images from the first tests using literature values are shown. When comparing *Figs.* 58a and 58b or *Figs.* 58c and 58d, it seems that the structures become more contrasted when increasing the number of scans M when all other parameters are the same. The higher contrast between bright and dark areas shows a larger phase-shift across the microstructure. Thus, repeating the same structure with the same RNF for a higher number of scans M result into stronger refractive index changes. While increasing the number of scans seems to increase only the magnitude of the refractive index change, varying the pulse energy E_p results in a difference in the written structure itself. In *Figs.* 58a and 58b, the structure for lower pulse energy values E_p consists of a bright line in the center with negative refractive index change and a smooth darker positive refractive index change region surrounding it. When comparing the situation to higher pulse energies E_p utilized in *Figs.* 58c and 58d, the structures look different. Besides the bright area of negative refractive index change in the center, there exists a surrounding pattern of alternating bright and dark areas. Hence, increasing the pulse energy E_p results in different material changes during the fabrication process, which cannot be described by a simple increase of the refractive index change as it is the case for an increased scan number M. Varying the writing speed v_s is shown in *Fig.* 59, while the pulse energy E_p is chosen as utilized in most of the literature. The writing speed was halved due to the repetition rate R_p being twice as low in the ULI system at AIP compared to the literature. Comparing *Figs.* 59a and 59b, the central bright negative refractive index region increases in width and has a higher contrast to the surrounding areas for a reduced writing speed v_s. Furthermore, for lower writing speeds v_s in *Fig.* 59b, the dark positive refractive index region is narrower than for higher writing speeds v_s in *Fig.* 59b. Overall, a lower writing speed v_s seems to increase the contrast and intensity of the refractive index changes. None of the initial experiments lead to a type I modification of the material. One potential explanation for the observed negative refractive index change occurring in conjunction with surrounding positive refractive index changes is the use of pulse energies that are too high. A way to experimentally investigate this hypothesis is to write single line structures without any repetitions, while varying the pulse energies E_p over a larger parameter space. A discussion of these experiments is provided in the following section.

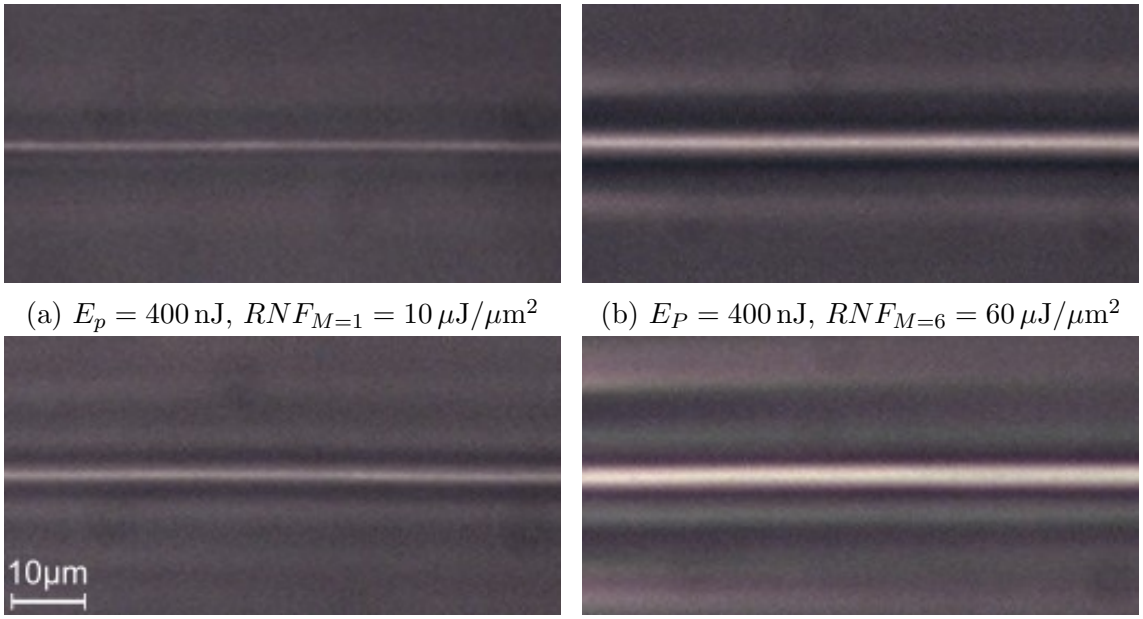

(a) $E_p = 400\,\mathrm{nJ}$, $RNF_{M=1} = 10\,\mu\mathrm{J}/\mu\mathrm{m}^2$

(b) $E_P = 400\,\mathrm{nJ}$, $RNF_{M=6} = 60\,\mu\mathrm{J}/\mu\mathrm{m}^2$

(c) $E_P = 830\,\mathrm{nJ}$, $RNF_{M=1} = 20\,\mu\mathrm{J}/\mu\mathrm{m}^2$

(d) $E_P = 830\,\mathrm{nJ}$, $RNF_{M=6} = 120\,\mu\mathrm{J}/\mu\mathrm{m}^2$

Figure 58: Top view. All structures were written with a writing speed of $v_s = 40\,\mathrm{mm/s}$ resulting in a number of pulses of $N_p^{v_s \neq 0} = 8$ per spot area, while the pulse energy E_p and the number of scans M was varied. In the lower left figure, a $10\,\mu\mathrm{m}$ scale is provided to facilitate the comparison of the structure sizes in all images in this figure. Similar scales can be found in other figures showing images from the phase contrast microscope. Note that the laser was incident perpendicular to the image plane.

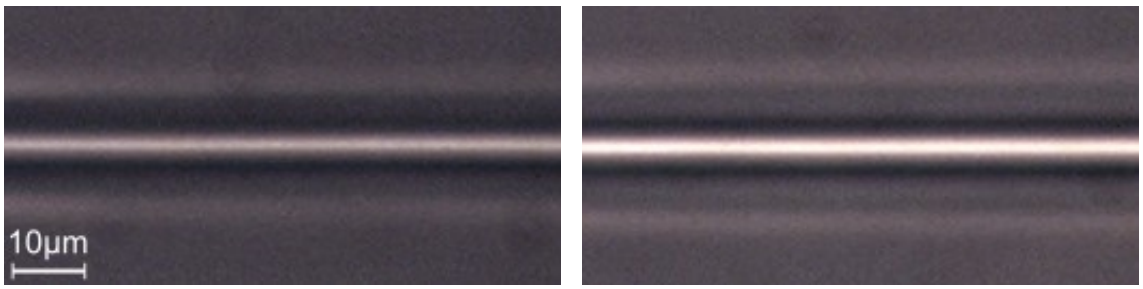

(a) $v_s = 40\,\mathrm{mm/s}$, $RNF_{M=6} = 60\,\mu\mathrm{J}/\mu\mathrm{m}^2$, $N_p^{v_s \neq 0} = 8$

(b) $v_s = 20\,\mathrm{mm/s}$, $RNF_{M=6} = 114\,\mu\mathrm{J}/\mu\mathrm{m}^2$, $N_p^{v_s \neq 0} = 17$

Figure 59: Top view. All structures were written with the same pulse energy $E_p = 400\,\mathrm{nJ}$ and numbers of scans $M = 6$, while the writing speed v_s was varied.

6.4.1.2 Pulse Energy Ramps for Different Speeds The term pulse energy ramp describes experiments, in which the pulse energy E_p (and with that the laser power P_{ave}) is varied over a wide range from low to high values. This was completed for different writing speeds v_s including 10 mm/s, 20 mm/s, 40 mm/s, and 50 mm/s. In this chapter, solely the pulse energy ramp for $v_s = 40\,\text{mm/s}$ is discussed and shown in *Fig.* 60, whereas the other pulse energy ramp images and brief discussions can be found in *Ch.* A.4.2. The structure in *Fig.* 60a is written with the lowest pulse energy of $E_p = 70\,\text{nJ}$ resulting in a net fluence as low as $RNF_{M=1} = 2\,\mu\text{J}/\mu\text{m}^2$. This structure mainly consists of a thin on-axis negative refractive index change with a barely visible area of positive refractive index change surrounding it. When increasing the pulse energy E_p further, the same effect as in *Fig.* 58 for an increase in pulse energy is visible. The alternating dark and bright off-axis areas are exceptionally visible in *Fig.* 60d. For even higher pulse energies in *Figs.* 60e and 60f, the brightest line in the center seems to have small spotty areas possibly due to damages. Similar results were found for other writing speeds v_s in *Ch.* A.4.2. To conclude the pulse energy ramp experiments, solely negative refractive index changes were observed even for low pulse energies E_p where the written structures were barely visible at all. For higher pulse energies E_p alternating dark and bright off-axis areas were visible and in a few cases small spotty areas within the brightest line of negative refractive index change potentially caused by mechanical damages within the material. Thus, a too high pulse energy E_p does not explain the reason why solely negative refractive index changes surrounded by positive refractive areas are observed within the material. In the case, that the refractive index change is not perfectly visible from the top view, a similar pulse energy ramp was performed exemplary in a vertically placed glass substrate in order to see the cross-section or front view and side view of the structures. The results of this test are discussed in the next part.

6.4.1.3 Vertical — Cross-Section or Front View and Side View As shown in *Fig.* 57, the samples have to be placed vertically in the sample holder within the ULI system (see *Fig.* 55) in order to enable an observation of the front view or cross-section and side view of a written structure. After the pulse energy ramp, this was done exemplary for a few selected pulse energy values E_p as depicted in *Fig.* 61. The images on the left show the cross-section or front view, while the right images show the side view of structures written with the same parameter set. In all front view images, the center of the structure has a bright negative refractive index area. For *Fig.* 61a, this is difficult so see as the alternating dark and bright rings around the central area have a much higher contrast. The aforementioned effect is most clearly discernible in *Fig.* 61c for a lower pulse energy compared to *Fig.* 61a. In *Fig.* 61e, the cross-section for the structure with the lowest pulse

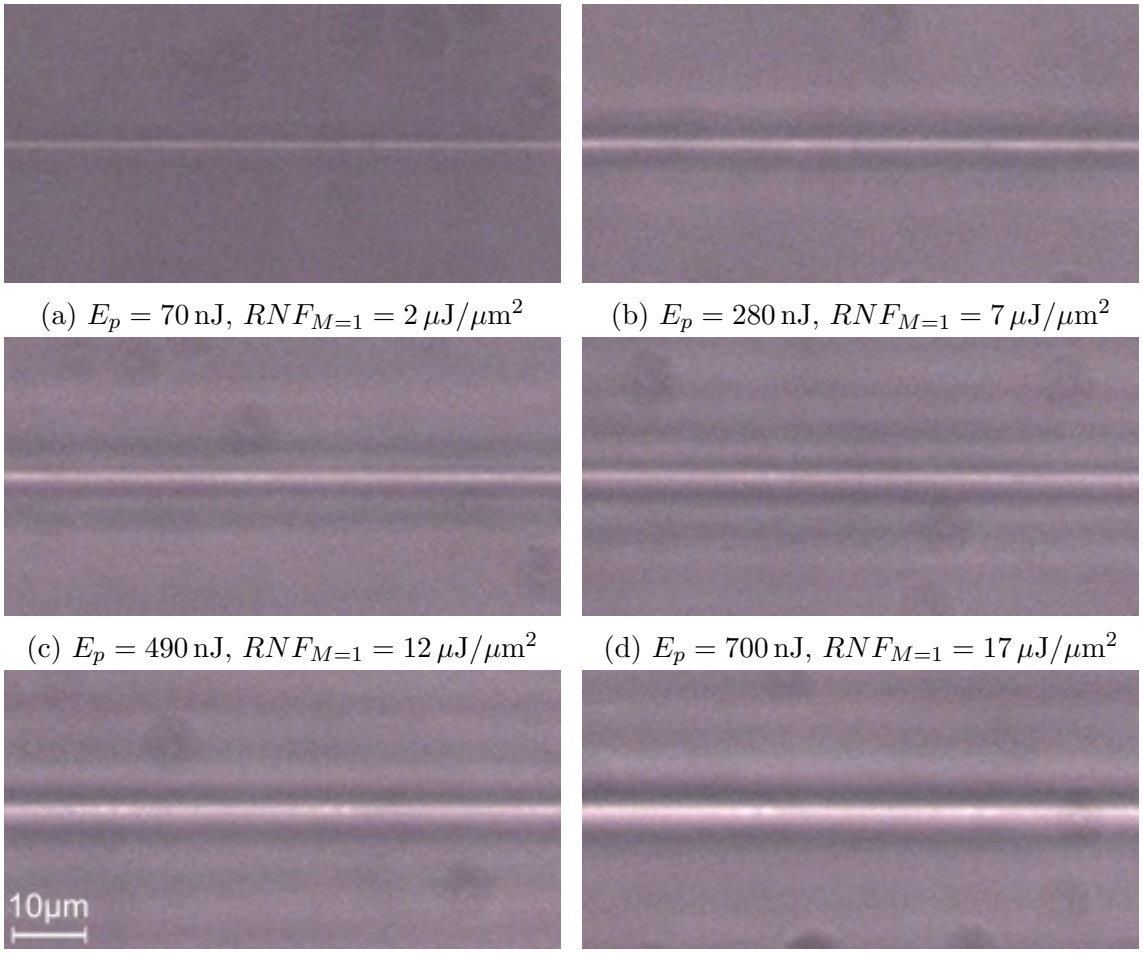

(a) $E_p = 70\,\mathrm{nJ}$, $RNF_{M=1} = 2\,\mu\mathrm{J}/\mu\mathrm{m}^2$ (b) $E_p = 280\,\mathrm{nJ}$, $RNF_{M=1} = 7\,\mu\mathrm{J}/\mu\mathrm{m}^2$

(c) $E_p = 490\,\mathrm{nJ}$, $RNF_{M=1} = 12\,\mu\mathrm{J}/\mu\mathrm{m}^2$ (d) $E_p = 700\,\mathrm{nJ}$, $RNF_{M=1} = 17\,\mu\mathrm{J}/\mu\mathrm{m}^2$

(e) $E_p = 910\,\mathrm{nJ}$, $RNF_{M=1} = 22\,\mu\mathrm{J}/\mu\mathrm{m}^2$ (f) $E_p = 1120\,\mathrm{nJ}$, $RNF_{M=1} = 27\,\mu\mathrm{J}/\mu\mathrm{m}^2$

Figure 60: Top view. All structures were written with the writing speed $v_s = 40\,\mathrm{mm/s}$ and number of scans $M = 1$ resulting into $N_p^{v_s \neq 0} = 8$ number of pulses per area, while the pulse energy E_p was varied.

energy of $E_p = 210\,\mathrm{nJ}$ has a dark positive refractive index change region right above the negative refractive index change zone below it in the center. The dark area is surrounded by negative refractive index changes. Nonetheless, the structure with the small positive index change region in the center in *Fig.* 61e is not large enough to enable light propagation of H- or K-band light, which requires a waveguide width of several μm. The multiscan technique [96] describes how writing several rows and layers with multiple repetitions can increase the width of the written structure (see *Fig.* 52). However, the positive refractive index change shown in *Fig.* 61e is completely surrounded by negative refractive index changes. Thus, when writing several rows and layers, the structure presumably would not result in one smooth large enough area of solely positive refractive index change. On the right side of *Fig.* 61, the side views of the structures written with the same parameter sets are visible. The side view does not show a clear positive or negative refractive index change in the center. This could be explained by the alternating dark and bright areas through which the light propagates in the phase contrast microscope when looking at the cross-sections. In the side views, lines with varying index changes are visible at the top and bottom of the structures. These could be explained by the light propagating through the structure where the cross-section is thinner than in the center. It can be concluded that, for these specific parameter sets, the side view is insufficient for determining the type of refractive index changes that occur within the material. However, the front view or cross-section provides a more comprehensive understanding of the index changes and structure sizes. Nonetheless, once a suitable parameter set is found, the ULI-written structures should be investigated from all sides for a complete understanding of the refractive index changes. When varying solely the number of scans M, again an enhancement of the contrast under the phase contrast microscope is visible as shown in *Fig.* 62 for the cross-section or front view of the written structure. Earlier in this chapter, the same effect was seen for the top view in *Fig.* 59. Because not a single parameter set was found, which created a smooth on-axis positive refractive index change over a large set of parameters, other options for creating waveguides should be investigated. One of these options could be the use of different materials for the glass substrate as each material inherently has different chemical compositions and properties, such as thermal conductivity. Furthermore, a microscope objective with a different numerical aperture NA could be purchased to increase the focusing spot size. Another option with the current conditions is the investigation of double line structures followed by experimenting with the multiscan technique [96]. As a first step, double line structures are discussed in the following section.

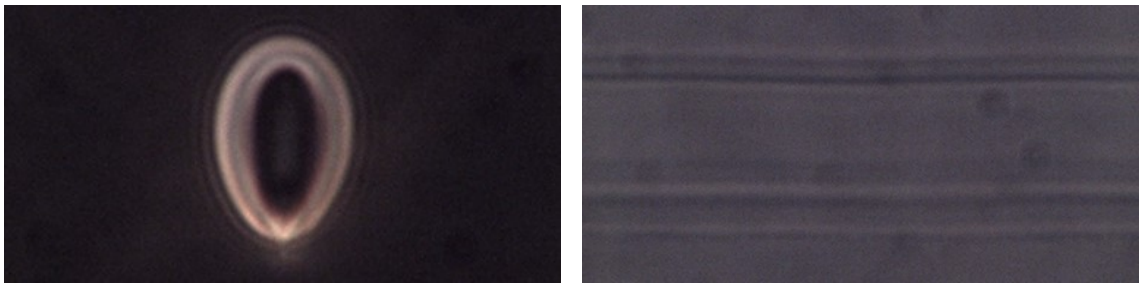

(a) $E_p = 830\,\mathrm{nJ}$, $RNF_{M=6} = 120\,\mu\mathrm{J}/\mu\mathrm{m}^2$ (b) $E_p = 830\,\mathrm{nJ}$, $RNF_{M=6} = 120\,\mu\mathrm{J}/\mu\mathrm{m}^2$

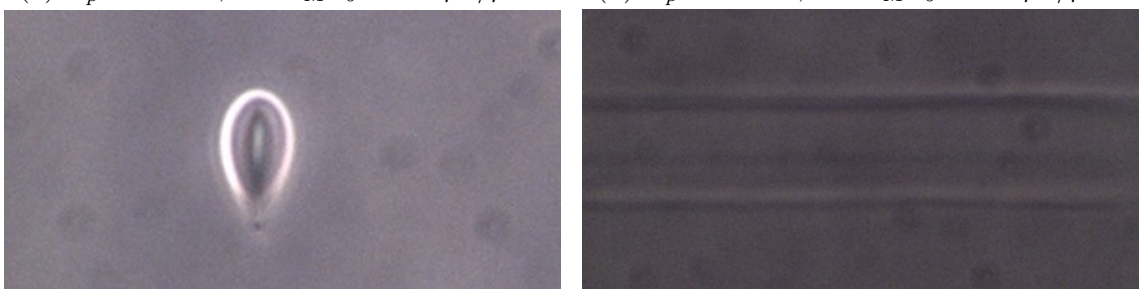

(c) $E_p = 400\,\mathrm{nJ}$, $RNF_{M=6} = 60\,\mu\mathrm{J}/\mu\mathrm{m}^2$ (d) $E_p = 400\,\mathrm{nJ}$, $RNF_{M=6} = 60\,\mu\mathrm{J}/\mu\mathrm{m}^2$

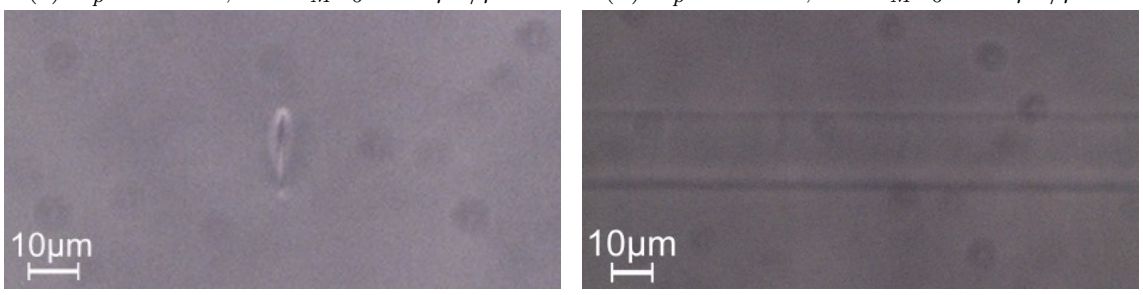

(e) $E_p = 210\,\mathrm{nJ}$, $RNF_{M=6} = 30\,\mu\mathrm{J}/\mu\mathrm{m}^2$ (f) $E_p = 210\,\mathrm{nJ}$, $RNF_{M=6} = 30\,\mu\mathrm{J}/\mu\mathrm{m}^2$

Figure 61: Left: Cross-Section or Front View. Right: Side View. All structures were written with the writing speed $v_s = 40\,\mathrm{mm/s}$ and number of scans $M = 6$ resulting into $N_p^{v_s \neq 0} = 8$ number of pulses per area per scan, while the pulse energy E_p was varied. Note that for all front view or cross-section and side view images, the structures were written with a laser incident from the top of the images.

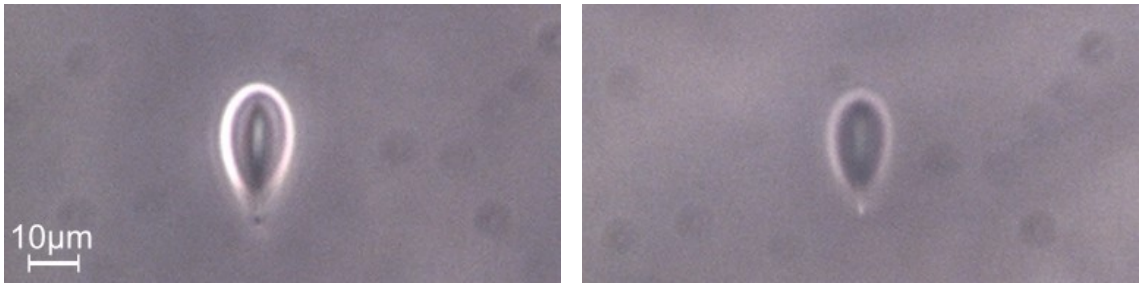

(a) $M = 6$, $RNF_{M=6} = 60\,\mu\mathrm{J}/\mu\mathrm{m}^2$ (b) $M = 1$, $RNF_{M=1} = 10\,\mu\mathrm{J}/\mu\mathrm{m}^2$

Figure 62: Cross-Section. Comparison of the cross-sections for the same writing speed $v_s = 40\,\mathrm{mm/s}$, pulse energy $E_p = 400\,\mathrm{nJ}$ and the same number of pulses per area per scan of $N_p^{v_s \neq 0} = 8\,\mathrm{pulses}$, while the number of scans M is varied.

6.4.2 Double Line Structures

In order to create a waveguide between two lines separated by the so-called row distance d_R, it is necessary to select a parameter set that exhibits a smooth negative refractive index change on-axis inside the focusing spot, while simultaneously displaying a strong and smooth positive refractive index change around it. For that, the pulse energy ramps for different writing speeds shown in *Fig.* 60 as well as *Figs.* 68, 69 and 70 in *Ch.* A.4 were compared. One suitable option was found for a writing speed of $v_s = 10\,\mathrm{mm/s}$ and a pulse energy of $E_p = 280\,\mathrm{nJ}$ as depicted in *Fig.* 68h. Other suitable parameters sets for future investigation can be found in the pulse energy ramp for a writing speed of $v_s = 50\,\mathrm{mm/s}$ according to the images in *Fig.* 70. In general, the exploration of the parameter space is an iterative process, in which different parameter sets are tested, and their results are employed to select new values. Thus, the parameter set for a writing speed of $v_s = 10\,\mathrm{mm/s}$ is utilized for an initial double line structure test with varying row distances d_R shown in *Fig.* 63. A row distance of $d_R = 1\,\mu\mathrm{m}$ as shown in *Fig.* 63a is barely visible at all. As stated earlier, a sufficient waveguide width for light propagation for NIR wavelengths is roughly $10\,\mu\mathrm{m}$. Thus, row separations up to $d_R = 10\,\mu\mathrm{m}$ were tested, however, for row separations closer to this value, the dark refractive index regions are not large enough and a bright negative refractive index change is visible between both lines (see *Figs.* 63h, 63i and 63j). Whereas, for row separations between $d_R = 2\,\mu\mathrm{m}$ and $d_R = 4\,\mu\mathrm{m}$, a smooth dark area of positive refractive index change is visible in between the ULI-written structures in the top view. As seen earlier, looking at the cross-section or front view enabled a more complete understanding of the fabricated structure. Thus, the cross-section or front view is analyzed in order to investigate the effect of varying the row separation d_R on the creation of a smooth positive refractive index region in between written structures. In *Fig.* 64, the top view and front view or cross-section are depicted for two row separations $d_R = 4\,\mu\mathrm{m}$ and $d_R = 8\,\mu\mathrm{m}$ as well as for varying number of scans M. The latter resulted in an enhancement of the contrast, which in turn led to an increase in the refractive index changes that were created. For a row separation of $d_R = 4\,\mu\mathrm{m}$, it is clearly visible that the positive refractive index change areas of both structures are overlapping. Especially in *Figs.* 64c and 64d, the higher scan number M enhances the recognizability of the overlapped region. However, in the cross-section or front view in *Figs.* 64d, it becomes clear that the dark positive refractive index change area is not large enough for efficient light propagation. When the row separation is doubled, the overlap of the dark regions is barely visible, especially for a single scan as shown in *Figs.* 64e and 64f. For a scan number of $M = 6$, a small overlap of the dark positive refractive index change regions is visible in the front view or cross-section (see

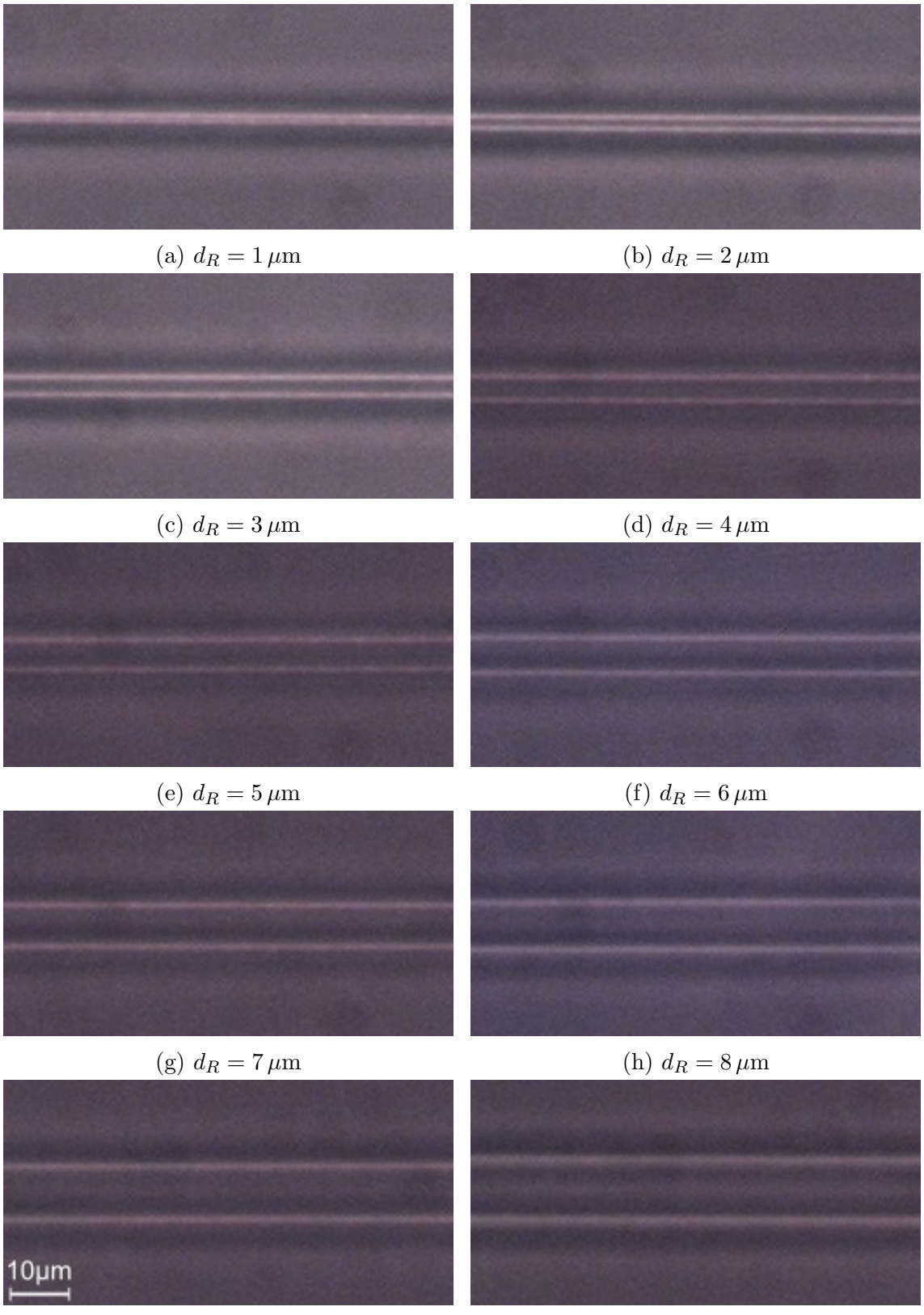

(a) $d_R = 1\,\mu\text{m}$ (b) $d_R = 2\,\mu\text{m}$

(c) $d_R = 3\,\mu\text{m}$ (d) $d_R = 4\,\mu\text{m}$

(e) $d_R = 5\,\mu\text{m}$ (f) $d_R = 6\,\mu\text{m}$

(g) $d_R = 7\,\mu\text{m}$ (h) $d_R = 8\,\mu\text{m}$

(i) $d_R = 9\,\mu\text{m}$ (j) $d_R = 10\,\mu\text{m}$

Figure 63: Top View. Double structures are two line structures written with the same parameter set but separated by a varied row distance d_R. All single lines were written with a writing speed of $v_s = 10\,\text{mm/s}$, a pulse energy of $E_p = 280\,\text{nJ}$, a scan number of $M = 1$ with $N_p^{v_s \neq 0} = 33$ pulses per spot area, which resulted into a net fluence of $RNF_{M=1} = 27\,\mu\text{J}/\mu\text{m}^2$.

Fig. 64h). These results are promising, indicating that a microstructure supporting waveguiding at optical frequencies can be fabricated with a similar parameter set and the multiscan technique. In future multiscan experiments, several layers with a layer separation d_L could be added besides two rows separated by a distance d_R. Investigation of other waveguide arrangements could be another option, such as the circular arrangement shown in *Fig.* 52.
The results presented in this chapter can be viewed as a first step in the iterative process of exploring the parameter space for a ULI system. Thus, there are many possible ways to continue the parameter space investigation. Firstly, different materials (e.g. alumino-borosilicate (Eagle XG) or fused silica) can be acquired and tested. It is important to acknowledge that the specific chemical composition of each material leads to distinct behaviors. Secondly, the existing microscope objective with a higher numerical aperture of 0.75 NA could be experimentally compared to the results accomplished and presented in this thesis with the 0.5 NA objective. However, the lower NA objective already resulted in a smaller spot size compared to the literature due to the shorter wavelength used in the ULI system at AIP. Thus, according to *Eq.* 11, a higher NA would result into an even smaller spot size, possibly leading to mechanical damages (e.g. microcracks or micro / macro pore formation) depending on the material. Nonetheless, testing the higher NA objective is another option for future experiments. Currently, one of the most promising options is utilizing multiscan techniques to create waveguides. For that, the ULI system at AIP does not necessarily require changes. A challenge of the multiscan technique is the addition of more variable parameters, such as overall structure arrangement as well as row and layer separation, d_R and d_L respectively. Another alternative could be the change of the ULI system to the longer wavelength of $\lambda = 1040\,\text{nm}$. Although this is not an easy to change variable as the setup itself has to be adapted, it would make the system more comparable to other systems described in the literature in *Tab.* 16. Furthermore, some ULI systems include beam shaping optics such as Spatial Light Modulators (SLMs) or slits at the entrance of the focusing microscope objectives. These beam shaping optics result in more symmetric beam shapes within the glass substrates [87, 90, 104]. In the future a slit could be implemented into the beam path of the ULI system at AIP.

To conclude the available options, as a first step the multiscan technique with the present conditions can be explored, while other materials are purchased. Once a variety of materials is available, experiments similar to the tests described in this thesis can be carried out. Furthermore, experiments with both objectives can be performed. All of these options potentially lead to the fabrication of waveguides with smooth positive refractive index changes as described for type I modifications.

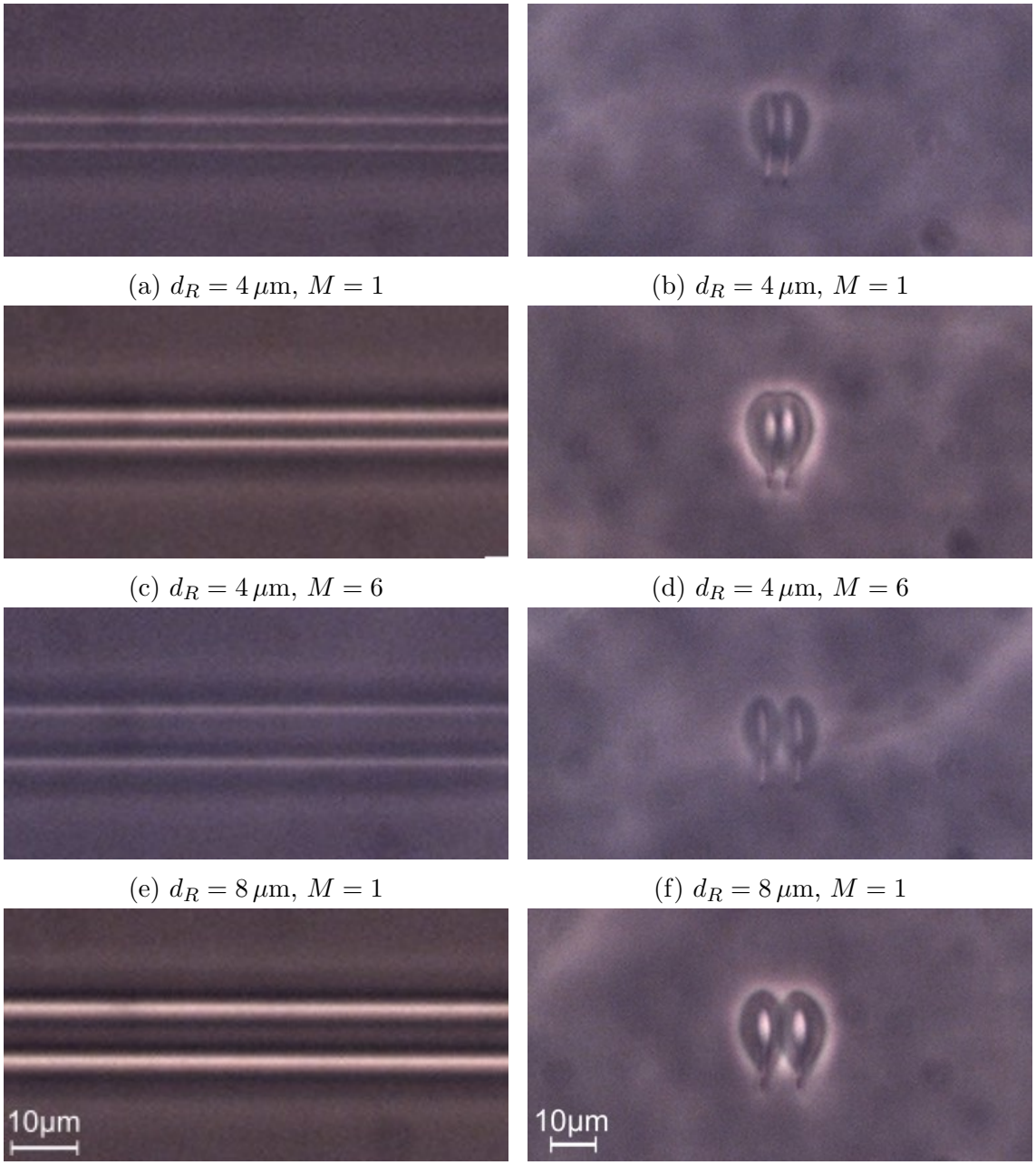

(a) $d_R = 4\,\mu$m, $M = 1$ (b) $d_R = 4\,\mu$m, $M = 1$

(c) $d_R = 4\,\mu$m, $M = 6$ (d) $d_R = 4\,\mu$m, $M = 6$

(e) $d_R = 8\,\mu$m, $M = 1$ (f) $d_R = 8\,\mu$m, $M = 1$

(g) $d_R = 8\,\mu$m, $M = 6$ (h) $d_R = 8\,\mu$m, $M = 6$

Figure 64: Left: Top View. Right: Cross-Section. Double structures are two line structures written with the same parameter set but separated by a varied row distance d_R. All single lines were written with a writing speed of $v_s = 10\,\text{mm/s}$, a pulse energy of $E_p = 280\,\text{nJ}$, a scan number of $M = 1$ or $M = 6$ with $N_p^{v_s \neq 0} = 33$ pulses per spot area per repetition, which resulted into a net fluence of $RNF_{M=1} = 27\,\mu\text{J}/\mu\text{m}^2$ or $RNF_{M=6} = 162\,\mu\text{J}/\mu\text{m}^2$.

Alternatively, a multiscan arrangement might be found to exploit the negative refractive index changes surrounded by positive refractive change regions. Another future option could be the implementation of beam shaping optics into the beam path of the ULI system at AIP. Overall, the experimental exploration of the parameter space is an iterative process, which will benefit from exchange with the MBI in Berlin-Adlershof and the Politecnico di Milano. As soon as a suitable parameter set is found — exploiting whatever modification type — different beam combination designs can be investigated. A few examples of ULI-written beam combination designs were briefly introduced in *Ch.* 5.2.
Exploring the parameter space is a critical step towards the goal of achieving a complete in house chain of design, fabrication and characterization of novel ULI-written astrophotonics at AIP. As ULI-written astrophotonic beam combiners are under constant development, laboratory and on-sky tests are required to further improve the overall throughput and coupling-losses of such components. CHARIOT will enable such lab and on-sky experiments once it is fully implemented, characterized and commissioned for the astronomy community worldwide. In *Ch.* 7 the most important conclusions and results from the work on CHARIOT and on the exploration of the parameter space for the ULI system at AIP are presented. Additionally, an outlook on both topics is provided.

7 Conclusions and Outlook

This thesis addresses two topics. The first concerns the CHARIOT setup for testing astrophotonic beam combiners. The second is an exploration of the parameter space of the ULI system at AIP, with the objective of enabling waveguide writing and thus future fabrication of astrophotonic beam combiners that could be tested in CHARIOT. This chapter presents the most significant conclusions and results achieved during the course of this thesis and provides an outlook for future work.

In the context of high angular resolution interferometry with several telescopes, astrophotonic beam combiners can provide space-saving solutions compared to bulk optics, since they have small footprints (typically on the cm-scale). In addition, astrophotonics can increase the temperature- and vibrational stability of an interferometric instrument compared to bulk optics. Their compact and stable design also make astrophotonic devices promising for space-based interferometers. Their suitability for future missions is currently under investigation [5, 105], one example is the proposed mid-infrared nulling interferometer LIFE (Large Interferometer For Exoplanets) [106].
Developing astrophotonics requires characterizing them in the laboratory, potentially followed by an optimization step and iterative refinement, and to verify them in on-sky tests. The latter is important to ensure functionality within a real interferometric array environment with imperfect conditions, such as atmospheric turbulence effects, humidity, and low signal strength. In this context, the goal of the CHARIOT setup is twofold. Firstly, the currently installed beam combiner is meant to be verified in on-sky tests. Secondly, CHARIOT has been prepared to enable future adaptation to become a plug-and-play laboratory- and on-sky testbench of novel astrophotonic 2D and 3D fiber-connectorized beam combiners in the future. More specifically, CHARIOT is planned to be a fully characterized 4-beam (nulling) beam combiner instrument covering the J-, H-, and K-bands at the CHARA Array accessible for the worldwide interferometry community. As first steps towards this goal, CHARIOT has been designed as a setup for four beams. Following this design and taking into account the positioning of additional components and beam paths, the 2-beam redirection subsystem was aligned together with a preliminary output imaging subsystem as part of this thesis in order to create a fully functional 2-beam CHARIOT setup. Achieving fringes with CHARIOT and the astrophotonic beam combiner in the CHARA BCL using a calibration source has been an important milestone on the path to on-sky verification. For that, it was crucial to fully compensate the OPD between all beams. This was taken into account in the planning of the 4-beam CHARIOT setup and in the alignment of the 2-beam redirection sub-

system as well. A significant portion of this thesis focused on the precise optical alignment of both beam paths (see *Ch.* 4.4). This was accomplished through the use of a range of tools, including various light sources, a pentaprism, a theodolite, and other standard tools. However, small path differences can be introduced during positioning of the optics. Especially for long path length of around 5 m from the start of BCL to the fiber-coupler and several optical components within each beam path, small OPD on the order of mm − cm between the two beams can be expected. Verification of the correctly aligned beam paths with fully corrected OPD was only feasible once the output imaging subsystem was available for detecting temporal interference fringes within the coherence length of the signal. These tests revealed a small OPD offset of approximately $\sim 4.8\,\mathrm{mm}$, which is less than one thousandth of the total beam path length. Placing the static stage $\sim 2.4\,\mathrm{mm}$ from its zero position allowed to compensate this OPD offset due to the double pass introduced by $M1$ and $M2$. This indicates that both beams are precisely aligned according to the planned CHARIOT layout. Additional tests were conducted using the 2-beam setup and the ULI K-band fiber-connectorized beam combiner, fabricated by a group at the Heriot-Watt University. For example, interferometric measurements with different bandwidths were performed, to identify suitable filters for laboratory optimization and for on-sky tests and to characterize the filters themselves using their measured coherence length. For the *K2101* filter ($\lambda^{K2101} = (2.101 \pm 0.010)\,\mu\mathrm{m}$) with a small bandwidth, the largest coherence length of $l^{K2101}_{\mathrm{coh,\,meas}} = (66.7 \pm 0.6)\,\mu\mathrm{m}$ was measured. While for the K' filter and no filter (*empty*), shorter coherence lengths of $l^{\mathrm{K'}}_{\mathrm{coh,\,meas}} = (15.89 \pm 0.09)\,\mu\mathrm{m}$ and $l^{\mathrm{empty}}_{\mathrm{coh,\,meas}} = (10.21 \pm 0.12)\,\mu\mathrm{m}$ were acquired experimentally. Differences between measured coherence lengths and those expected from the bandwidth given in the documentation are suspected to arise from the shape of the transmission curve, which is not an ideal "top-hat" function. A more detailed discussion on these measurements can be found in *Ch.* 4.6.1.1.

As part of the latest measurement campaign, the first on-sky fringes were successfully recorded with the achromatic fiber-connectorized K-band ULI-written beam combiner in the 2-beam CHARIOT setup at the CHARA Array with the 34 m $S1 - S2$ baseline on May 2nd 2024. The CHARIOT team present at CHARA during the observation night is shown celebrating the milestone of CHARIOT's first fringes in *Fig.* 46. The first fringes were obtained on AW CVn (HD 120933) in standard weather conditions (~ 1 arcsecond seeing). Even fainter sources down to a magnitude K~ 4 were recorded. This result was obtained by researchers from the NAIR-2 / APREXIS team including the AIP, University of Cologne, the Heriot-Watt University, the Durham University with strong support from GSU CHARA staff. Some results of CHARIOT were published and presented during the SPIE Astronomical Telescopes + Instrumentation conference 2024 in Yokohama, Japan

and can be found in [4, 5].
During the laboratory characterization, the output imaging subsystem was found to introduce aberrations and reduce the signal strength of off-axis outputs significantly. This may be due to vignetting within the output imaging subsystem. Thus, a redesign and adaption of the output imaging subsystem is of the highest importance for future work on CHARIOT. Other possible future upgrades to CHARIOT include adding two more beam paths, expanding the setup to include J-, H-bands besides the K-band, and implementing plug-and-play interfaces. Furthermore, replacing the magnetic mounts of the pick-off mirrors $M0$ with motorized mounts would allow automated insertion and removal of the pick-off mirrors $M0$ into and out of the beam path without the loss of mirror alignment. Additionally, the replacement of the pick-off mirrors $M0$ with dichroics would enable the utilization of the MIRC-X instrument as a fringe tracker in the H-band simultaneously with scientific measurements conducted by CHARIOT in the K-band. In later upgrades for CHARIOT, the implementation of a cryostat for the beam combiner is planned to reduce thermal noise. However, initial upgrades should include the installation of an output imaging subsystem with high throughput, plug-and-play interfaces, and a fully automated setup as these changes are crucial to facilitate the utilization of CHARIOT as an accessible instrument for on-sky testing of astrophotonic devices for the interferometry community.

Such on-sky experiments are crucial for the development of novel astrophotonics, in addition to the design, fabrication and characterization process of the devices themselves. As a first step towards waveguide writing and the fabrication of astrophotonic beam combiners with the ULI System at AIP, different settings were used to modify glass samples, thereby exploring a subset of the vast parameter space. Discussions with Dr. Alexandre Mermillod-Blondin of the MBI in Berlin-Adlershof led to the use of phase-contrast microscopy for the qualitative analysis of ULI-written structures in glass substrates. As a starting point, values were extracted from references as part of a literature study. Note that due to the differences between the systems, each group might find a unique set of parameters. Here, we found that the system by Politecnico di Milano is comparably close to the ULI system at AIP, with differences, e.g. in repetition rate R_p, numerical aperture NA, and used material. However, a large parameter space for a range of writing speeds v_s and pulse energies E_p were experimentally tested in borosilicate glass substrates (Borofloat 33, Schott) with a 0.5 NA microscope objective. In order to achieve different viewpoints, the glass substrates were positioned in both horizontal and vertical orientations within the ULI system as schematically shown in *Fig.* 57. Initially, single-line structures were examined to prevent the introduction of additional variables resulting from the

multiscan technique. All written structures resulted in on-axis negative refractive index changes, which were surrounded by stress fields with positive refractive index changes. This type of modification can be described with type II modification as defined in *Ch.* 5.3.2. No smooth solely positive refractive index change (type I modification) was accomplished so far. Nevertheless, some conclusions can be drawn from the exploration of the parameter space for single line structures. In particular, insight can be gained by investigating the influence on the fabricated structure when a single parameter is varied, such as number of scans M, pulse energy E_p and writing speed v_s.

1. Higher **number of scans** M result in stronger refractive index changes.

2. A variation in **pulse energy** E_p changes the characteristics of the structure. Higher energies lead to the formation of alternating off-axis dark and bright areas of positive and negative refractive index changes. While lower pulse energies E_p show a single on-axis negative refractive index change line surrounded by a zone of positive refractive index change on either side. Reducing pulse energies further resulted in a decrease of contrast. Thus, too high pulse energies might not be the reason for the negative refractive index changes alone.

3. Changes in the **writing speed** v_s are visible through a varied contrast and intensity properties. A lower writing speed $v_s = 20\,\mathrm{mm/s}$ compared $v_s = 40\,\mathrm{mm/s}$ seems to increase the contrast and intensity of the refractive index changes.

Similar results as above were visible but from the front view showing negative refractive index changes in the center of the written structure surrounded by dark and bright areas. The side view did not give additional information as this viewpoint integrates the refractive index changes through the full width of the structure, making it difficult so investigate zones of different refractive indices. From these results and the strong positive refractive index off-axis stress fields, it was concluded that multiscan techniques might be a possible solution for fabricating light-guiding waveguides. Thus, in a first attempt, double line structures for a writing speed of $v_s = 10\,\mathrm{mm/s}$ and a pulse energy of $E_p = 280\,\mathrm{nJ}$ were written with different number of scans M and row separations d_R. An overlap of the dark positive refractive index regions is visible for a single scan at row distances up to $d_R = 4\,\mu\mathrm{m}$, while for six scans an overlap is created for separations up to $d_R = 8\,\mu\mathrm{m}$. The initial double-line structure results are encouraging, and further investigation of different parameter sets and multiscan techniques may facilitate the fabrication of a light-guiding waveguide. Future experiments could include adding several layers with a so-called layer separation d_L taking into account the elongation of the spot in z-direction. Additionally,

more complex circular writing arrangements could be tested to achieve structures with positive refractive index change, which are large enough ($\sim 10\,\mu$m) to guide NIR light. If this does not lead to sufficient results with the current conditions of the ULI system, there are a range of other possibilities to explore:

1. Purchasing and testing different materials, such as alumino-borosilicate glasses (Eagle XG, Corning) or fused silica glass substrates. Each material has different chemical compositions and properties, which lead to different changes within the material.

2. Utilizing the microscope objective with higher numerical aperture of 0.75 NA. Such a microscope objective was not used so far in glass substrates as the higher NA leads to an even tighter focusing spots than it is already the case for the lower NA objective. Another possibility is to purchase a new microscope objective with a different NA.

3. Changing the ULI system at AIP to use the longer wavelength of $\lambda = 1040\,$nm instead of $\lambda = 520\,$nm of the laser. This adaptation requires a change of the ULI system itself and can not be done on a regular basis.

4. Implementation of beam shaping optics in the beam path of the ULI system in order to achieve a more circular beam shape within the material.

Some of the above suggestions might already lead to the fabrication of waveguides sufficient for guiding NIR light. Once this is achieved, different beam combiner types as discussed in *Ch.* 5.2 can be explored. Finding a suitable parameter space is crucial for the goal of having the complete chain of design, fabrication and characterization of beam combiners in house at AIP. Developments in astrophotonics are critical to achieving lower coupling losses and higher throughput. The future goal of CHARIOT is to serve this purpose by making laboratory and on-sky testing accessible with automated setup and plug-and-play interfaces.

This concludes the numerous results achieved during the planning of the 4-beam, the installation of the fully functional 2-beam CHARIOT setup, and the initial exploration of the parameter space for the ULI system at AIP. Both objectives can be viewed as bracketing the topic of developing novel astrophotonic beam combiners. The work completed as part of this thesis provides a foundation for the goal of fabricating ULI-written astrophotonic beam combiners at AIP, as well as verifying them in on-sky tests using the CHARIOT instrument. Continuing the experiments for the parameter space exploration as well as implementing upgrades to the existing 2-beam CHARIOT setup are necessary for successful development of astrophotonic beam combiners.

8 References

1. Monnier, J. D. Optical interferometry in astronomy. *Reports on Progress in Physics* **66,** 789–857. https://doi.org/10.1088/0034-4885/66/5/203 (2003).

2. Glindemann, A. *Principles of Stellar Interferometry* ISBN: 978-3-642-15027-2 (Springer Science & Business Media, 2011).

3. Scott, N. J. *First science with JouFLU* PhD thesis (Georgia State University, Jan. 2015).

4. Mayer, A. V. *et al. Chara Array integrated optics testbench (CHARIOT) for on-sky experiments* in *Optical and Infrared Interferometry and Imaging IX* (eds Kammerer, J., Sallum, S. & Sanchez-Bermudez, J.) **13095** (SPIE, 2024), 130951V. https://doi.org/10.1117/12.3019140.

5. Dinkelaker, A. N. *Astrophotonic technologies* in *Optical and Infrared Interferometry and Imaging IX* (eds Kammerer, J., Sallum, S. & Sanchez-Bermudez, J.) **13095** (SPIE, 2024), 130950R. https://doi.org/10.1117/12.3029483.

6. Padovani, P. & Cirasuolo, M. The Extremely Large Telescope. *Contemporary Physics* **64,** 47–64. ISSN: 1366-5812. http://dx.doi.org/10.1080/00107514.2023.2266921 (Jan. 2023).

7. Dalcanton, J. J. 18 years of science with the Hubble Space Telescope. *Nature* **457,** 41–50. ISSN: 1476-4687. https://doi.org/10.1038/nature07621 (Jan. 2009).

8. Kalirai, J. Scientific discovery with the James Webb Space Telescope. *Contemporary Physics* **59,** 251–290. eprint: https://doi.org/10.1080/00107514.2018.1467648. https://doi.org/10.1080/00107514.2018.1467648 (2018).

9. Ten Brummelaar, T. A. *et al.* First Results from the CHARA Array. II. A Description of the Instrument. *The Astrophysical Journal* **628,** 453. https://dx.doi.org/10.1086/430729 (July 2005).

10. *The Center for High Angular Resolution Astronomy (CHARA) Array by Geogia State University* https://www.chara.gsu.edu/. (Accessed: 22 May 2024).

11. GRAVITY Collaboration *et al.* First light for GRAVITY: Phase referencing optical interferometry for the Very Large Telescope Interferometer. *Astronomy & Astrophysics* **602,** A94. https://doi.org/10.1051/0004-6361/201730838 (2017).

12. Blind, N. *et al. GRAVITY: the VLTI 4-beam combiner for narrow-angle astrometry and interferometric imaging* 2015. arXiv: astro-ph.IM/1503.07303. https://arxiv.org/abs/1503.07303.

13. Le Bouquin, J.-B. *et al.* PIONIER: a 4-telescope visitor instrument at VLTI. *Astronomy & Astrophysics* **535.** https://doi.org/10.1051/0004-6361/201117586 (Nov. 2011).

14. Rains, A. D., Ireland, M. J., White, T. R., Casagrande, L. & Karovicova, I. Precision angular diameters for 16 southern stars with VLTI/PIONIER. *Monthly Notices of the Royal Astronomical Society* **493,** 2377–2394. ISSN: 0035-8711. eprint: https://academic.oup.com/mnras/article-pdf/493/2/2377/32743320/staa282.pdf. https://doi.org/10.1093/mnras/staa282 (Mar. 2020).

15. Anugu, N. *et al.* The Great Dimming of the Hypergiant Star RW Cephei: CHARA Array Images and Spectral Analysis. *The Astronomical Journal* **166,** 78. https://dx.doi.org/10.3847/1538-3881/ace59d (July 2023).

16. Anugu, N. *et al.* Time Evolution Images of the Hypergiant RW Cephei during the Rebrightening Phase Following the Great Dimming. *The Astrophysical Journal Letters* **973,** L5. https://dx.doi.org/10.3847/2041-8213/ad736c (Sept. 2024).

17. Jadlovský, D. *et al.* The Great Dimming of Betelgeuse: The photosphere as revealed by tomography over the past 15 yr. *Astronomy & Astrophysics* **685,** A124. ISSN: 1432-0746. http://dx.doi.org/10.1051/0004-6361/202348846 (May 2024).

18. Boyajian, T. S. *et al.* Stellar Diameters and Temperatures. I. Main-Sequence A, F, and G Stars. *The Astrophysical Journal* **746,** 101. https://dx.doi.org/10.1088/0004-637X/746/1/101 (Jan. 2012).

19. Boyajian, T. S. *et al.* Stellar Diameters and Temperatures. II. Main-Sequence K- and M-Stars. *The Astrophysical Journal* **757,** 112. https://dx.doi.org/10.1088/0004-637X/757/2/112 (Sept. 2012).

20. Boyajian, T. S. *et al.* Stellar Diameters and Temperatures. III. Main-Sequence A, F, G, And K Stars: Additional High-Precision Measurements and Empirical Relations. *The Astrophysical Journal* **771,** 40. https://dx.doi.org/10.1088/0004-637X/771/1/40 (June 2013).

21. Roettenbacher, R. *et al.* No Sun-like dynamo on the active star ζ Andromedae from starspot asymmetry. *Nature* **533,** 217–220. ISSN: 0028-0836 (May 2016).

22. Kral, Q. *et al.* Exozodiacal clouds: hot and warm dust around main sequence stars. *Astronomical Review* **13,** 69–111. ISSN: 2167-2857. https://doi.org/10.1080/21672857.2017.1353202 (Apr. 2017).

23. von Braun, K. & Boyajian, T. *Extrasolar Planets and Their Host Stars* ISBN: 9783319611983. http://dx.doi.org/10.1007/978-3-319-61198-3 (Springer International Publishing, 2017).

24. Marboeuf, U., Bonsor, A. & Augereau, J.-C. Extrasolar comets: The origin of dust in exozodiacal disks? *Planetary and Space Science* **133,** 47–62. ISSN: 0032-0633. https://www.sciencedirect.com/science/article/pii/S003206331530101X (Nov. 2016).

25. Ertel, S., Absil, O., Defrère, D., Augereau, J.-C. & Mennesson, B. Prospects for the characterisation of exo-zodiacal dust with the VLTI. *Experimental Astronomy* **46,** 401–411. ISSN: 1572-9508. https://doi.org/10.1007/s10686-018-9600-7 (Dec. 2018).

26. Minardi, S., Harris, R. J. & Labadie, L. Astrophotonics: astronomy and modern optics. *The Astronomy and Astrophysics Review* **29,** 6. ISSN: 1432-0754. https://doi.org/10.1007/s00159-021-00134-7 (Sept. 2021).

27. Absil, O. *et al.* Circumstellar material in the Vega inner system revealed by CHARA/FLUOR. *Astronomy & Astrophysics* **452,** 237–244. https://doi.org/10.1051/0004-6361:20054522 (2006).

28. Nuñez, P. D. *et al.* A near-infrared interferometric survey of debris-disc stars - VI. Extending the exozodiacal light survey with CHARA/JouFLU. *Astronomy & Astrophysics* **608,** A113. https://doi.org/10.1051/0004-6361/201730859 (Dec. 2017).

29. Eisenhauer, F., Monnier, J. D. & Pfuhl, O. Advances in Optical/Infrared Interferometry. *Annual Review of Astronomy and Astrophysics* **61,** 237–285. ISSN: 1545-4282. https://www.annualreviews.org/content/journals/10.1146/annurev-astro-121622-045019 (2023).

30. Roettenbacher, R. M. *et al.* No Sun-like dynamo on the active star ζ Andromedae from starspot asymmetry. *Nature* **533,** 217–220. ISSN: 1476-4687. https://doi.org/10.1038/nature17444 (May 2016).

31. Anugu, N. *et al.* MIRC-X: A Highly Sensitive Six-telescope Interferometric Imager at the CHARA Array. *The Astronomical Journal* **160,** 158. arXiv: astro-ph.IM/2007.12320 (Oct. 2020).

32. Anugu, N. *et al. MIRC-X/CHARA: sensitivity improvements with an ultra-low noise SAPHIRA detector* in *Optical and Infrared Interferometry and Imaging VI* (eds Creech-Eakman, M. J., Tuthill, P. G. & Mérand, A.) **10701** (July 2018), 1070124. arXiv: astro-ph.IM/1807.03809.

33. Ibrahim, N. *et al.* Imaging the Inner Astronomical Unit of the Herbig Be Star HD 190073. *The Astrophysical Journal* **947,** 68. https://dx.doi.org/10.3847/1538-4357/acb4ea (Apr. 2023).

34. Buscher, D. F. & Longair, M. *Practical Optical Interferometry: Imaging at Visible and Infrared Wavelengths* (Cambridge University Press, 2015).

35. Labeyrie, A., Lipson, S. G. & Nisenson, P. *An Introduction to Optical Stellar Interferometry* (Cambridge University Press, 2006).

36. Léna, P., Rouan, D., Lebrun, F., Mignard, F. & Pelat, D. *Observational astrophysics; 3rd ed.* https://cds.cern.ch/record/1433748 (Springer, Berlin, 2012).

37. Goodman, J. W. *Statistical optics* (John Wiley & Sons, 2000).

38. Millour, F. *All you ever wanted to know about optical long baseline stellar interferometry, but were too shy to ask your adviser* working paper or preprint. 2008. https://hal.archives-ouvertes.fr/hal-00273465.

39. Lawson, P. *Principles of long baseline stellar interferometry* in (JPL, 2000).

40. Nave, C. R. (*HyperPhysics* Last Accessed: 2024-09-06. 2017. http://hyperphysics.phy-astr.gsu.edu/hbase/phyopt/dslit.html.

41. The Event Horizon Telescope Collaboration *et al.* First M87 Event Horizon Telescope Results. II. Array and Instrumentation. *The Astrophysical Journal Letters* **875,** L2. ISSN: 2041-8205. https://doi.org/10.3847/2041-8213/ab0c96 (Apr. 2019).

42. The Event Horizon Telescope Collaboration *et al.* First M87 Event Horizon Telescope Results. I. The Shadow of the Supermassive Black Hole. *The Astrophysical Journal Letters* **875,** L1. ISSN: 2041-8205. https://doi.org/10.3847/2041-8213/ab0ec7 (Apr. 2019).

43. Setterholm, B. R. *et al. MYSTIC: a high angular resolution K-band imager at CHARA* in *Optical and Infrared Interferometry and Imaging VIII* (eds Mérand, A., Sallum, S. & Sanchez-Bermudez, J.) **12183** (SPIE, 2022), 121830B. https://doi.org/10.1117/12.2629437.

44. Monnier, J. D. *et al. MYSTIC: Michigan Young STar Imager at CHARA* in *Optical and Infrared Interferometry and Imaging VI* (eds Creech-Eakman, M. J., Tuthill, P. G. & Mérand, A.) **10701** (SPIE, 2018), 1070122. https://doi.org/10.1117/12.2312762.

45. GRAVITY Collaboration *et al.* First light for GRAVITY: Phase referencing optical interferometry for the Very Large Telescope Interferometer. *Astronomy & Astrophysics* **602,** A94. https://doi.org/10.1051/0004-6361/201730838 (2017).

46. Dolan, M. M. *et al.* Evolutionary tracks for Betelgeuse. *The Astrophysical Journal* **819,** 7. ISSN: 1538-4357. http://dx.doi.org/10.3847/0004-637X/819/1/7 (2016).

47. Anugu, N. *et al.* Betelgeuse scope: single-mode-fibers-assisted optical interferometer design for dedicated stellar activity monitoring. *Interferometry XX.* http://dx.doi.org/10.1117/12.2568900 (2020).

48. Michelson, A. A. & Pease, F. G. Measurement of the Diameter of Alpha-Orionis by the Interferometer. *Proceedings of the National Academy of Sciences* **7,** 143–146. ISSN: 0027-8424. https://www.pnas.org/content/7/5/143 (1921).

49. Du Foresto, V. C. *et al. FLUOR fibered instrument at the IOTA interferometer* in *Astronomical Interferometry* (ed Reasenberg, R. D.) **3350** (SPIE, 1998), 856–863. https://doi.org/10.1117/12.317153.

50. Guyon, O. Extreme Adaptive Optics. *Annual Review of Astronomy and Astrophysics* **56,** 315–355. ISSN: 1545-4282. https://www.annualreviews.org/content/journals/10.1146/annurev-astro-081817-052000 (2018).

51. Ellis, S. C., Bland-Hawthorn, J. & Leon-Saval, S. G. General coupling efficiency for fiber-fed astronomical instruments. *J. Opt. Soc. Am. B* **38,** A64–A74. https://opg.optica.org/josab/abstract.cfm?URI=josab-38-7-A64 (July 2021).

52. Ten Brummelaar, T. A. *et al.* The Classic/Climb Beam Combiner at the CHARA Array. *Journal of Astronomical Instrumentation* **2,** 1340004 (Dec. 2013).

53. Ten Brummelaar, T. The CLASSIC/CLIMB Data Reduction: The Software. *European Astronomical Society Publications Series* **70,** 101–131 (2014).

54. Ten Brummelaar, T. The CLASSIC/CLIMB Data Reduction: The Math. *European Astronomical Society Publications Series* **70,** 75–99 (2014).

55. Ireland, M. J. *et al. Sensitive visible interferometry with PAVO* in *Optical and Infrared Interferometry* (eds Schöller, M., Danchi, W. C. & Delplancke, F.) **7013** (July 2008), 701324.

56. Mourard, D. *et al.* SPICA, Stellar Parameters and Images with a Cophased Array: a 6T visible combiner for the CHARA array. *J. Opt. Soc. Am. A* **34,** A37–A46. https://opg.optica.org/josaa/abstract.cfm?URI=josaa-34-5-A37 (May 2017).

57. Pannetier, C. *et al. Progress of the CHARA/SPICA project* in *Optical and Infrared Interferometry and Imaging VII* (eds Tuthill, P. G., Mérand, A. & Sallum, S.) **11446** (Dec. 2020), 114460T. arXiv: astro-ph.IM/2101.10926.

58. Pannetier, C. *et al. SPICA-FT: the new fringe tracker of the CHARA array* in *Optical and Infrared Interferometry and Imaging VIII* (eds Mérand, A., Sallum, S. & Sanchez-Bermudez, J.) **12183** (SPIE, 2022), 1218309. https://doi.org/10.1117/12.2628897.

59. Mourard, D. *et al.* VEGA: Visible spEctroGraph and polArimeter for the CHARA array: principle and performance. *Astronomy & Astrophysics* **508,** 1073–1083 (Dec. 2009).

60. Anugu, N. *et al.* CHARA/Silmaril Instrument Software and Data Reduction Pipeline: Characterization of the Instrument in the Lab and On-Sky. *arXiv e-prints,* arXiv:2406.17886. arXiv: astro-ph.IM/2406.17886 (June 2024).

61. Lanthermann, C. *et al. Design of the new CHARA instrument SILMARIL: pushing for the sensitivity of a 3-beam combiner in the H- and K-bands* in *Optical and Infrared Interferometry and Imaging VIII* (eds Mérand, A., Sallum, S. & Sanchez-Bermudez, J.) **12183** (Aug. 2022), 121830N. arXiv: astro-ph.IM/2208.12963.

62. Coudé Du Foresto, V. *et al. FLUOR fibered beam combiner at the CHARA array* in *Interferometry for Optical Astronomy II* (ed Traub, W. A.) **4838** (SPIE, 2003), 280–285. https://doi.org/10.1117/12.459942.

63. Scott, N. J. *et al.* Jouvence of Fluor: Upgrades of a Fiber Beam Combiner at the CHARA Array. *Journal of Astronomical Instrumentation* **2,** 1340005. https://doi.org/10.1142/S2251171713400059 (Dec. 2013).

64. Coudé du Foresto, V. & Ridgway, S. T. *Fluor - a Stellar Interferometer Using Single-Mode Fibers* in *European Southern Observatory Conference and Workshop Proceedings* (eds Beckers, J. M. & Merkle, F.) **39** (Mar. 1992), 731.

65. Franzen, A. ComponentLibrary: a free vector graphics library for optics. *Licensed under a Creative Commons Attribution-NonCommercial 3.0 Unported License.* https://www.gwoptics.org/ComponentLibrary/ (2009).

66. Siliprandi, J. *et al.* Fiber-connectorized ultrafast-laser-inscribed K-band integrated optics beam combiner for the CHARA telescope array. *Appl. Opt.* **63,** 159–166. https://opg.optica.org/ao/abstract.cfm?URI=ao-63-1-159 (Jan. 2024).

67. Benoît, A. *et al.* Ultrafast laser inscription of asymmetric integrated waveguide 3 dB couplers for astronomical K-band interferometry at the CHARA array. English. *Journal of the Optical Society of America B: Optical Physics* **38,** 2455–2464. ISSN: 0740-3224 (Sept. 2021).

68. Hecht, E. *Optik* (Walter de Gruyter, June 2023).

69. Smith, W. J. *Modern Optical Engineering* (McGraw-Hill Professional Publishing, Jan. 2000).

70. Deumlich, F. & Faig, W. *Surveying Instruments* (Walter de Gruyter GmbH, Berlin/Boston, GERMANY, 1982).

71. Gillen, G. D. *Laser Laboratory Beam Alignment Skills: Course Package* 2024. arXiv: physics.ed-ph/2404.16225. https://arxiv.org/abs/2404.16225.

72. Ellis, S., Bland-Hawthorn, J. & Leon-Saval, S. *Principles of Astrophotonics* eprint: https://www.worldscientific.com/doi/pdf/10.1142/q0391. https://www.worldscientific.com/doi/abs/10.1142/q0391 (WORLD SCIENTIFIC (EUROPE), 2023).

73. Jovanovic, N. *et al.* 2023 Astrophotonics Roadmap: pathways to realizing multi-functional integrated astrophotonic instruments. *Journal of Physics: Photonics* **5,** 042501. https://dx.doi.org/10.1088/2515-7647/ace869 (Oct. 2023).

74. Dinkelaker, A. N. *et al.* Astrophotonics: introduction to the feature issue. *Appl. Opt.* **60,** AP1–AP6. https://opg.optica.org/ao/abstract.cfm?URI=ao-60-19-AP1 (July 2021).

75. Scott, N. J. *et al. CMAP: a mobile 7th telescope at the CHARA Array* in *Optical and Infrared Interferometry and Imaging IX* (eds Kammerer, J., Sallum, S. & Sanchez-Bermudez, J.) **13095** (SPIE, 2024), 130951U. https://doi.org/10.1117/12.3018516.

76. Koehler, R. *et al. Integrating a mobile telescope into the CHARA array* in *Optical and Infrared Interferometry and Imaging IX* (eds Kammerer, J., Sallum, S. & Sanchez-Bermudez, J.) **13095** (SPIE, 2024), 1309504. https://doi.org/10.1117/12.3020620.

77. Artigau, É. *et al. NIRISS aperture masking interferometry: an overview of science opportunities* in *Space Telescopes and Instrumentation 2014: Optical, Infrared, and Millimeter Wave* (eds Jr., J. M. O., Clampin, M., Fazio, G. G. & MacEwen, H. A.) **9143** (SPIE, 2014), 914340. https://doi.org/10.1117/12.2055191.

78. Soulain, A. *et al. The James Webb Space Telescope aperture masking interferometer* in *Optical and Infrared Interferometry and Imaging VII* (eds Tuthill, P. G., Mérand, A. & Sallum, S.) **11446** (SPIE, 2020), 1144611. https://doi.org/10.1117/12.2560804.

79. Cooper, R. A. *et al. Commissioning and calibration of the JWST Aperture Masking Interferometry mode* in *Optical and Infrared Interferometry and Imaging IX* (eds Kammerer, J., Sallum, S. & Sanchez-Bermudez, J.) **13095** (SPIE, 2024), 130952R. https://doi.org/10.1117/12.3019153.

80. Yilbas, B. S., Al-Sharafi, A. & Ali, H. in *Self-Cleaning of Surfaces and Water Droplet Mobility* (eds Yilbas, B. S., Al-Sharafi, A. & Ali, H.) 45–98 (Elsevier, 2019). ISBN: 978-0-12-814776-4. https://www.sciencedirect.com/science/article/pii/B9780128147764000033.

81. Perraut, K. *et al.* Single-mode waveguides for GRAVITY. I. The cryogenic 4-telescope integrated optics beam combiner. *Astronomy & Astrophysics* **614,** A70. https://doi.org/10.1051/0004-6361/201732544 (June 2018).

82. Nayak, A. S. *et al.* First stellar photons for an integrated optics discrete beam combiner at the William Herschel Telescope. *Appl. Opt.* **60,** D129–D142. https://opg.optica.org/ao/abstract.cfm?URI=ao-60-19-D129 (July 2021).

83. Dinkelaker, A. N. *et al.* Six-telescope integrated optics beam combiner fabricated using ultrafast laser inscription for J- and H-band astronomy. *Appl.*

Opt. **62,** 7596–7610. https://opg.optica.org/ao/abstract.cfm?URI=ao-62-29-7596 (Oct. 2023).

84. Minardi, S. & Pertsch, T. Interferometric beam combination with discrete optics. *Opt. Lett.* **35,** 3009–3011. https://opg.optica.org/ol/abstract.cfm?URI=ol-35-18-3009 (Sept. 2010).

85. Davis, K. M., Miura, K., Sugimoto, N. & Hirao, K. Writing waveguides in glass with a femtosecond laser. *Opt. Lett.* **21,** 1729–1731. https://opg.optica.org/ol/abstract.cfm?URI=ol-21-21-1729 (Nov. 1996).

86. Glezer, E. N. *et al.* Three-dimensional optical storage inside transparent materials. *Opt. Lett.* **21,** 2023–2025. https://opg.optica.org/ol/abstract.cfm?URI=ol-21-24-2023 (Dec. 1996).

87. Ghafur, O., Jürgens, P., Rammelt, L. & Mermillod-Blondin, A. in *Ultrafast Laser Nanostructuring: The Pursuit of Extreme Scales* (eds Stoian, R. & Bonse, J.) 759–786 (Springer International Publishing, Cham, 2023). ISBN: 978-3-031-14752-4. https://doi.org/10.1007/978-3-031-14752-4_21.

88. Valle, G. D., Osellame, R. & Laporta, P. Micromachining of photonic devices by femtosecond laser pulses. *Journal of Optics A: Pure and Applied Optics* **11,** 013001. https://dx.doi.org/10.1088/1464-4258/11/1/013001 (Dec. 2008).

89. Gross, S. & Withford, M. J. *Nanophotonics* **4,** 332–352. https://doi.org/10.1515/nanoph-2015-0020 (2015).

90. Osellame, R., Hoekstra, H., Cerullo, G. & Pollnau, M. Femtosecond laser microstructuring: an enabling tool for optofluidic lab-on-chips. *Laser & Photonics Reviews* **5,** 442–463. eprint: https://onlinelibrary.wiley.com/doi/pdf/10.1002/lpor.201000031. https://onlinelibrary.wiley.com/doi/abs/10.1002/lpor.201000031 (2011).

91. Lee, D., Thomson, R. R. & Cunningham, C. R. *Performance of volume phase gratings manufactured using ultrafast laser inscription* in *Modern Technologies in Space- and Ground-based Telescopes and Instrumentation II* (eds Navarro, R., Cunningham, C. R. & Prieto, E.) **8450** (SPIE, 2012), 84502X. https://doi.org/10.1117/12.926108.

92. Piacentini, S. *et al.* Advanced photonic and optofluidic devices fabricated in glass via femtosecond laser micromachining *Invited*. *Opt. Mater. Express* **12,** 3930–3945. https://opg.optica.org/ome/abstract.cfm?URI=ome-12-10-3930 (Oct. 2022).

93. MacLachlan, D. G. *et al. Development of photonic technologies for astronomical instruments using ultrafast laser inscription* PhD thesis (Heriot-Watt University, 2017).

94. Gross, S., Dubov, M. & Withford, M. J. On the use of the Type I and II scheme for classifying ultrafast laser direct-write photonics. *Opt. Express* **23,** 7767–7770. https://opg.optica.org/oe/abstract.cfm?URI=oe-23-6-7767 (Mar. 2015).

95. Corrielli, G., Crespi, A. & Osellame, R. *Nanophotonics* **10,** 3789–3812. https://doi.org/10.1515/nanoph-2021-0419 (2021).

96. Brown, G., Thomson, R. R., Kar, A. K., Psaila, N. D. & Bookey, H. T. Ultrafast laser inscription of Bragg-grating waveguides using the multiscan technique. *Opt. Lett.* **37,** 491–493. https://opg.optica.org/ol/abstract.cfm?URI=ol-37-4-491 (Feb. 2012).

97. Shah, L., Arai, A. Y., Eaton, S. M. & Herman, P. R. Waveguide writing in fused silica with a femtosecond fiber laser at 522 nm and 1 MHz repetition rate. *Opt. Express* **13,** 1999–2006. https://opg.optica.org/oe/abstract.cfm?URI=oe-13-6-1999 (Mar. 2005).

98. Rajesh, S. & Bellouard, Y. Towards fast femtosecond laser micromachining of fused silica: The effect of deposited energy. *Opt. Express* **18,** 21490–21497. https://opg.optica.org/oe/abstract.cfm?URI=oe-18-20-21490 (Sept. 2010).

99. Guan, J., Liu, X., Salter, P. S. & Booth, M. J. Hybrid laser written waveguides in fused silica for low loss and polarization independence. *Opt. Express* **25,** 4845–4859. https://opg.optica.org/oe/abstract.cfm?URI=oe-25-5-4845 (Mar. 2017).

100. Will, T., Guan, J., Salter, P. S. & Booth, M. J. Trimming laser-written waveguides through overwriting. *Opt. Express* **28,** 28006–28016. https://opg.optica.org/oe/abstract.cfm?URI=oe-28-19-28006 (Sept. 2020).

101. Murphy, D. B. & Davidson, M. W. in *Fundamentals of Light Microscopy and Electronic Imaging* 115–133 (John Wiley & Sons, Ltd, 2012).

102. Piacentini, S., Vogl, T., Corrielli, G., Lam, P. K. & Osellame, R. Space Qualification of Ultrafast Laser-Written Integrated Waveguide Optics. *Laser & Photonics Reviews* **15,** 2000167. eprint: https://onlinelibrary.wiley.com/doi/pdf/10.1002/lpor.202000167. https://onlinelibrary.wiley.com/doi/abs/10.1002/lpor.202000167 (2021).

103. Flamini, F. *et al.* Thermally reconfigurable quantum photonic circuits at telecom wavelength by femtosecond laser micromachining. *Light: Science & Applications* **4,** e354–e354. ISSN: 2047-7538. https://doi.org/10.1038/lsa.2015.127 (Nov. 2015).

104. McArthur, S. R. *et al.* Ultrafast laser inscription of efficient volume Bragg gratings deep in fused silica using active wavefront shaping. *Opt. Mater. Express* **12,** 3589–3599. https://opg.optica.org/ome/abstract.cfm?URI=ome-12-9-3589 (Sept. 2022).

105. Labadie, L. *et al. Astronomical photonics in the context of infrared interferometry and high-resolution spectroscopy* in *Optical and Infrared Interferometry and Imaging V* (eds Malbet, F., Creech-Eakman, M. J. & Tuthill, P. G.) **9907** (SPIE, Aug. 2016), 990718. http://dx.doi.org/10.1117/12.2230889.

106. Glauser, A. M. *et al. The Large Interferometer For Exoplanets (LIFE): a space mission for mid-infrared nulling interferometry* in *Optical and Infrared Interferometry and Imaging IX* (eds Kammerer, J., Sallum, S. & Sanchez-Bermudez, J.) **13095** (SPIE, 2024), 130951D. https://doi.org/10.1117/12.3019090.

A Appendix

A.1 Procedure Table Height Correction for CHARIOT

A self leveling laser level was used as seen in *Fig.* 65 with a free hanging laser hat leveled by gravity for the correction of the CHARIOT table height and the corresponding beam height of 6.5".

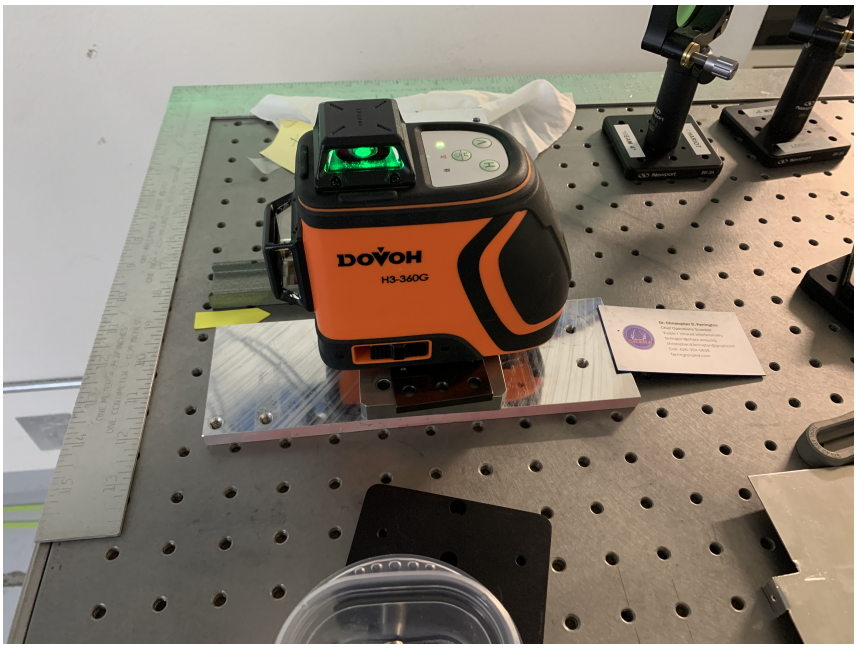

Figure 65: Image of the Dovoh H3-360G self-leveling green laser level used for table and beam height corrections.

As a first step, the green laser level was put on the pick-off table. The laser level emits several beams (horizontal and vertical). The important beam for the alignment of the beam height is the horizontal 360 degrees beam. Before the beam height alignment can start, a very important step is to align the height of the horizontal laser level beam with a reference. In this case, the targets from the MIRC-X/MYSTIC table were used. These targets are aligned with the CHARA beams and are therefore suitable as a reference. At the start, the suitability of the chosen reference (in our case the MIRC-X/MYSTIC targets) was verified. This can be done by shining both the laser level beam as well as the CHARA green laser beams onto the MIRC-X/MYSTIC target and precisely matching the height (the center) of the laser level beam with the center of the CHARA beams on the targets. The correct height of the laser level was achieved by using mechanical components, thin sheets or cardboard to put on top of the pick-off table and below the laser level. Here, a metal base and a paper card was utilized as a short term solution. For the future, this could be improved by using an adjustable mount at roughly the correct height. The matching

of the green laser level and the MIRC-X/MYSTIC target can be seen in *Fig.* 66. Now, the laser level beam height can be used as a reference for positioning various

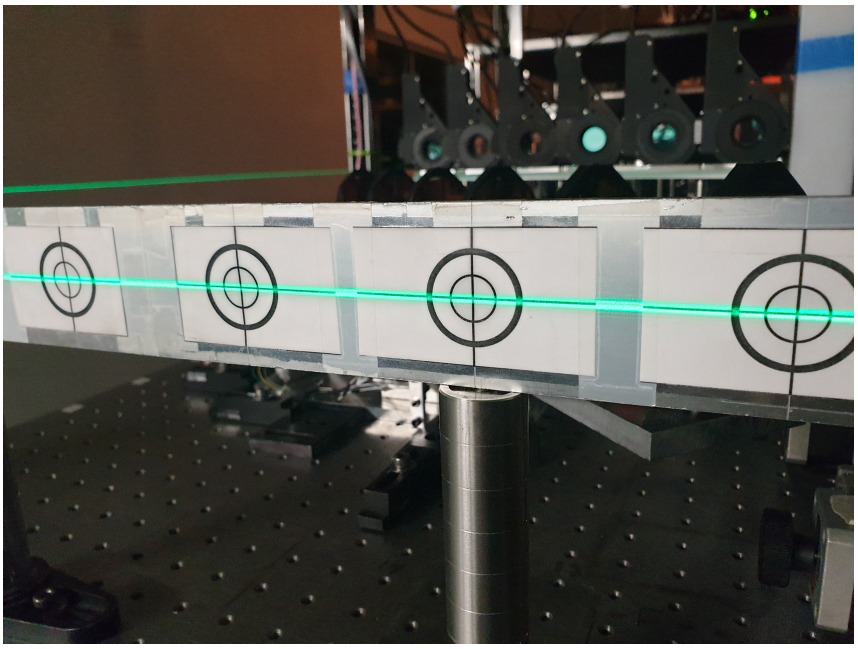

Figure 66: Alignment of the green laser level with the MIRC-X / MYSTIC targets to ensure the correct beam height.

targets and pinholes and optical components on the CHARIOT table. The laser level horizontal beam covers large parts of the CHARIOT optical table (everywhere where it is not blocked by other components, tables, etc.). In the next step, the beam height is marked using the center of the horizontal laser level beam on several positions of the CHARIOT optical table. This can be achieved by using tape on different walls and corners of the table or by utilizing the center of flipable targets in the front and in the back of the beam path. By using a ruler on a base or stand, the beam height from the CHARIOT optical table can be measured at different parts of the table (this is also a way to measure the flatness of the optical table).
With this procedure, the beam height after relocating the CHARIOT optical table was measured to be 6.375" ($\sim$ 16.2 cm), instead of the previous 6.5" ($\sim$ 16.5 cm) before relocating the optical table. As most optical components and mounts in the setup were designed for a beam height of 6.5", the height of the optical table had to be adjusted in order to match the design height. The complete CHARIOT table was lowered and leveled to achieve a beam height of 6.5". Changing the height of the CHARIOT optical table was done by pumping up the table to enable a rotation of the table feet, and thus changing their length. To lower the CHARIOT table to the correct position and to achieve a level surface, the adjustments were made while the alignment laser was switched on and aimed at different targets. Once the table legs are changed to the correct height and the jacks are lowered, the table

height should be checked using the self standing target on various locations on the table. If the table height is slightly off, special tools can be utilized for precise table height corrections. After the CHARIOT table height is changed to the correct beam height, a range of targets should be made as precisely as possible, because these are used to align the CHARA green laser beam throughout the optical path on the table. For that, the laser level was kept running and at the same position as during the table adjustment process. Targets were printed on paper (consisting of one horizontal and vertical line crossing in the middle with circles of different radii around it). The CHARIOT front target consists of a metal plate with four 1" holes separated by 6" as seen with paper targets on the right in *Fig.* 14b. This plate was put on larger posts for stability. The CHARIOT front target for the four beams of the CHARIOT setup is used for daily alignment of the CHARA green laser beams. Additional targets and pinholes were brought to the correct height while the green laser level was still on as seen in *Fig.* 14b.

A.2 Parameters of the ULI System at AIP

The laser parameters for a wavelength of $\lambda = 520\,\text{nm}$ are summarized in *Tab.* 17. *Tab.* 18 summarizes the parameters for the translation stages used in the ULI system.

Table 17: Laser (Spirit One SPOne-8-SHG) parameters for a central wavelength of $\lambda = 520\,\text{nm}$, taken from the report that was delivered with the laser.

Parameter	Unit	Specification	Measurement
Pulse Repetition Rate: Setting	kHz		500.0
Pulse Repetition Rate	kHz	$\pm 5.0\%$	498.7
Average Output Power	W	≥ 2.0	4.5
Output Pulse Energy	μJ	≥ 4.0	9.1
Output Pulse Duration	fs	≤ 400	260
Power Stability (RMS)	%	≤ 1.00	0.37
Central Wavelength	nm	520 ± 3.0	521.3
FWHM Bandwidth	nm	≤ 3	1.5
Beam Quality Factor $M^2\,X$		≤ 1.20	1.01
Beam Quality Factor $M^2\,Y$		≤ 1.20	1.02
Beam Diameter at Laser Exit X	mm	2.00 ± 0.20	2.11
Beam Diameter at Laser Exit Y	mm	2.00 ± 0.20	2.00
Divergence (full angle) X	mrad	≤ 0.50	0.36
Divergence (full angle) Y	mrad	≤ 0.50	0.36
Beam Ellipticity at Laser Exit	%	≤ 15	6
Astigmatism	%	≤ 20	16
Waist Diameter X	mm	1.90 ± 0.30	1.86
Waist Diameter Y	mm	1.90 ± 0.30	1.87

Table 18: Parameters for the x- and y-axis (Newport, XMS100) and the z-axis (Newport, VP-5ZA) translational stages according to the data sheets.

Parameter	Unit	Specification
Laser Wavelength Compatibility	nm	520 or 1040
Beam Entrance Height	mm	127
Total Travel Distance XYZ	mm	100 x 100 x 4.8
Typical Accuracy XY	μm	± 0.3
Speed XY	mm/s	300
Typical Accuracy Z	μm	± 0.6
Speed Z	mm/s	5
Laser System Set Temperature	$^\circ C$	25.0$\pm$2.0

A.3 ULI Literature Study

The writing parameters from the literature study are summarized in *Tab.* 19.

Table 19: This table is a detailed overview of the parameters from the literature study of systems with similar parameters compared to the ULI system at AIP. The values written in cursive are calculated from other given parameters according to the equations described in *Ch.* 5.3.4. Unknown values are denoted as / in the table.

Parameters	[83]	[82]	[102]	[103]	[90]
Laser Type	Yb:KYW	Yb:KYW	Yb:KYW	Yb:KYW	Yb:KYW
Wavelength λ_L [nm]	1030	1030	1030	1030	515 (second harmonic)
Material Substrate Name Company	borosilicate Eagle XG Corning	alumino-borosilicate Eagle XG Corning	borosilicate Eagle XG Corning	alumino-borosilicate EAGLE2000 Corning	fused silica
Pulse Duration τ_p [fs]	300	300	300	300	350
Repetition Rate R_p [kHz]	1000	1000	1000	1000	1000
Numerical Aperture NA	0.6 (50x)	0.6 (50x)	0.6 (50x)	0.6 (50x)	0.6 (50x)
Spot Diameter D_p [μm]	*1.093*	*1.093*	*1.093*	*1.093*	*0.546*
Writing Speed v_s [mm/s]	40	40	40	20	0.1
Number of Pulses $N_p^{v_s \neq 0}$	*27*	*27*	*27*	*55*	*14*
Pulse Energy E_p [nJ]	440	*620*	370 & 480	330	*90* (up to 1000)
Laser Power P_{ave} [mW]	*440*	620	*370 & 480*	*330*	90
RNF pro line $RNF_{M=1}$ [μJ/μm^2]	*12.82*	*18.06*	*10.78 & 13.98*	*19.22*	*5.24*
Total RNF RNF_M [μJ/μm^2]	*64.1*	*108.36*	*53.9 & 83.88*	*19.22*	*5.24*
Number of Scans M	5	6	5 & 6	/	/
Waveguide Width D_W [μm]	6.5(3)x7.0(3)	8.5(3)x9.0(3)	/	13.5	11
Notes	Thermal Annealing	Thermal Annealing	Thermal Annealing	Gold Layer Deposition & Patterning	/ /
Guided Wavelength λ_W [nm]	1310	1550	850& 1550	1550	1550

A.4 Experimental ULI Results

In this chapter, additional images from the phase contrast microscope for different parameter sets are given. Furthermore, the appearance of the structures for focus changes are briefly explained in the next section.

A.4.1 Focus Change of the Phase Contrast Microscope

In *Fig.* 67 the change in the appearance of the structure is exemplary shown under the phase contrast microscope. When comparing both figures, it becomes clear that the repeatable image of the structure in focus in *Fig.* 67a is altered when the focus is changed (see *Fig.* 67b). Thus, for analyzing images from structures under the phase contrast microscope, it is crucial to achieve the correct focus, because otherwise the conclusions cannot be correctly derived.

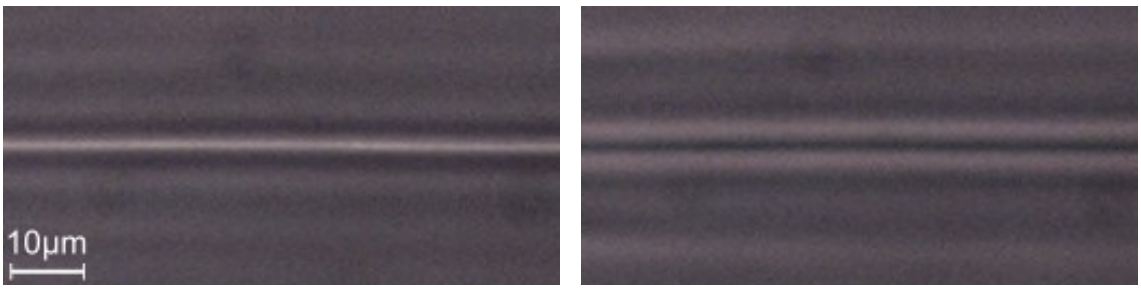

(a) Structure is in focus. (b) Structure is slightly defocused.

Figure 67: Both images show the same structure written with a writing speed of $v_s = 40\,\mathrm{mm/s}$, pulse energy of $E_p = 830\,\mathrm{nJ}$, number of pulses per spot area and per line of $N_p^{v_s \neq 0} = 8$ and a number of $M = 1$ scans. This results in a total net fluence of $RNF_{M=1} = 20\,\mu\mathrm{J}/\mu\mathrm{m}^2$. In (a) the structure is in the focus of the phase contrast microscope, while (b) shows a slightly defocused image.

A.4.2 Pulse Energy Ramps for Different Speeds

In this chapter, additional images for pulse energy ramp experiments with varying writing speeds are presented. In *Fig.* 68 the pulse energy E_p is varied for a writing speed of $v_s = 10\,\mathrm{mm/s}$. Whereas in *Fig.* 69 a pulse energy ramp for a writing speed of $v_s = 20\,\mathrm{mm/s}$ can be found. The highest writing speed of $v_s = 50\,\mathrm{mm/s}$ was investigated for a wide range of pulse energies E_p. The results can be found in *Fig.* 70.

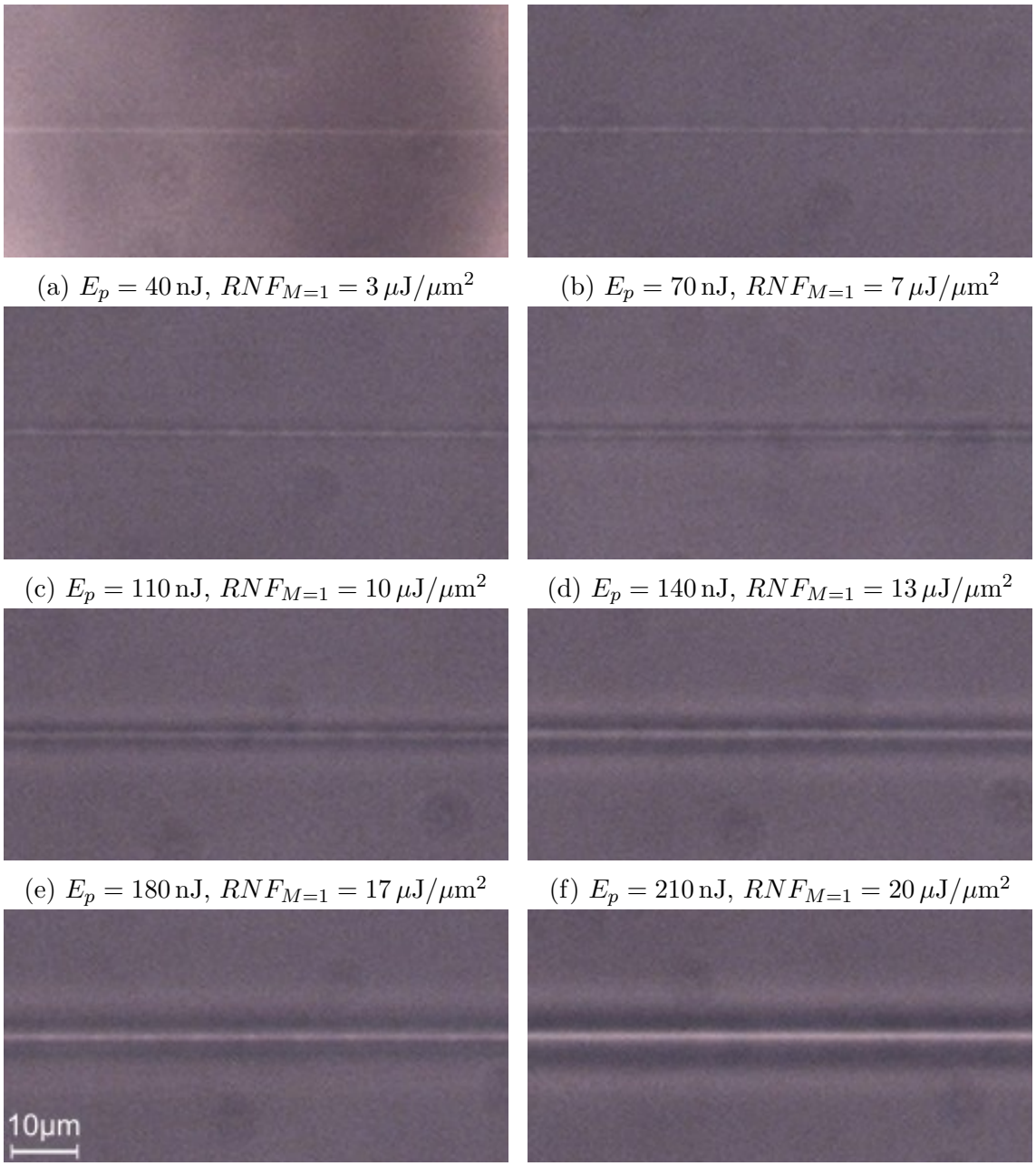

(a) $E_p = 40\,\mathrm{nJ}$, $RNF_{M=1} = 3\,\mu\mathrm{J}/\mu\mathrm{m}^2$

(b) $E_p = 70\,\mathrm{nJ}$, $RNF_{M=1} = 7\,\mu\mathrm{J}/\mu\mathrm{m}^2$

(c) $E_p = 110\,\mathrm{nJ}$, $RNF_{M=1} = 10\,\mu\mathrm{J}/\mu\mathrm{m}^2$

(d) $E_p = 140\,\mathrm{nJ}$, $RNF_{M=1} = 13\,\mu\mathrm{J}/\mu\mathrm{m}^2$

(e) $E_p = 180\,\mathrm{nJ}$, $RNF_{M=1} = 17\,\mu\mathrm{J}/\mu\mathrm{m}^2$

(f) $E_p = 210\,\mathrm{nJ}$, $RNF_{M=1} = 20\,\mu\mathrm{J}/\mu\mathrm{m}^2$

(g) $E_p = 250\,\mathrm{nJ}$, $RNF_{M=1} = 24\,\mu\mathrm{J}/\mu\mathrm{m}^2$

(h) $E_p = 280\,\mathrm{nJ}$, $RNF_{M=1} = 27\,\mu\mathrm{J}/\mu\mathrm{m}^2$

Figure 68: Top view. All structures were written with the writing speed $v_s = 10\,\mathrm{mm/s}$ and number of scans $M = 1$ resulting into $N_p^{v_s \neq 0} = 33$ number of pulses per area, while the pulse energy E_p was varied.

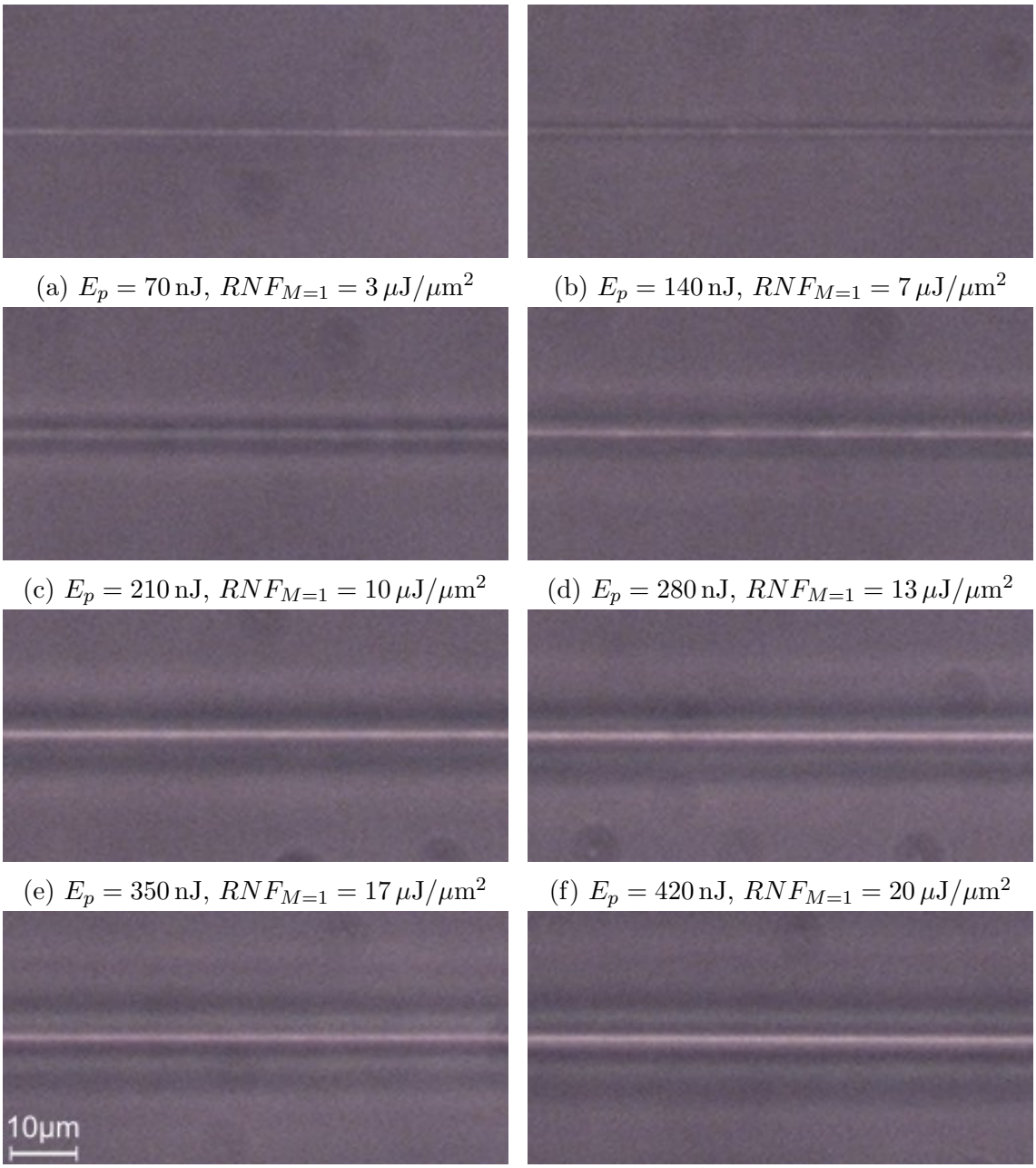

(a) $E_p = 70\,\mathrm{nJ}$, $RNF_{M=1} = 3\,\mu\mathrm{J}/\mu\mathrm{m}^2$

(b) $E_p = 140\,\mathrm{nJ}$, $RNF_{M=1} = 7\,\mu\mathrm{J}/\mu\mathrm{m}^2$

(c) $E_p = 210\,\mathrm{nJ}$, $RNF_{M=1} = 10\,\mu\mathrm{J}/\mu\mathrm{m}^2$

(d) $E_p = 280\,\mathrm{nJ}$, $RNF_{M=1} = 13\,\mu\mathrm{J}/\mu\mathrm{m}^2$

(e) $E_p = 350\,\mathrm{nJ}$, $RNF_{M=1} = 17\,\mu\mathrm{J}/\mu\mathrm{m}^2$

(f) $E_p = 420\,\mathrm{nJ}$, $RNF_{M=1} = 20\,\mu\mathrm{J}/\mu\mathrm{m}^2$

(g) $E_p = 490\,\mathrm{nJ}$, $RNF_{M=1} = 24\,\mu\mathrm{J}/\mu\mathrm{m}^2$

(h) $E_p = 560\,\mathrm{nJ}$, $RNF_{M=1} = 27\,\mu\mathrm{J}/\mu\mathrm{m}^2$

Figure 69: Top view. All structures were written with the writing speed $v_s = 20\,\mathrm{mm/s}$ and number of scans $M = 1$ resulting into $N_p^{v_s \neq 0} = 17$ number of pulses per area, while the pulse energy E_p was varied.

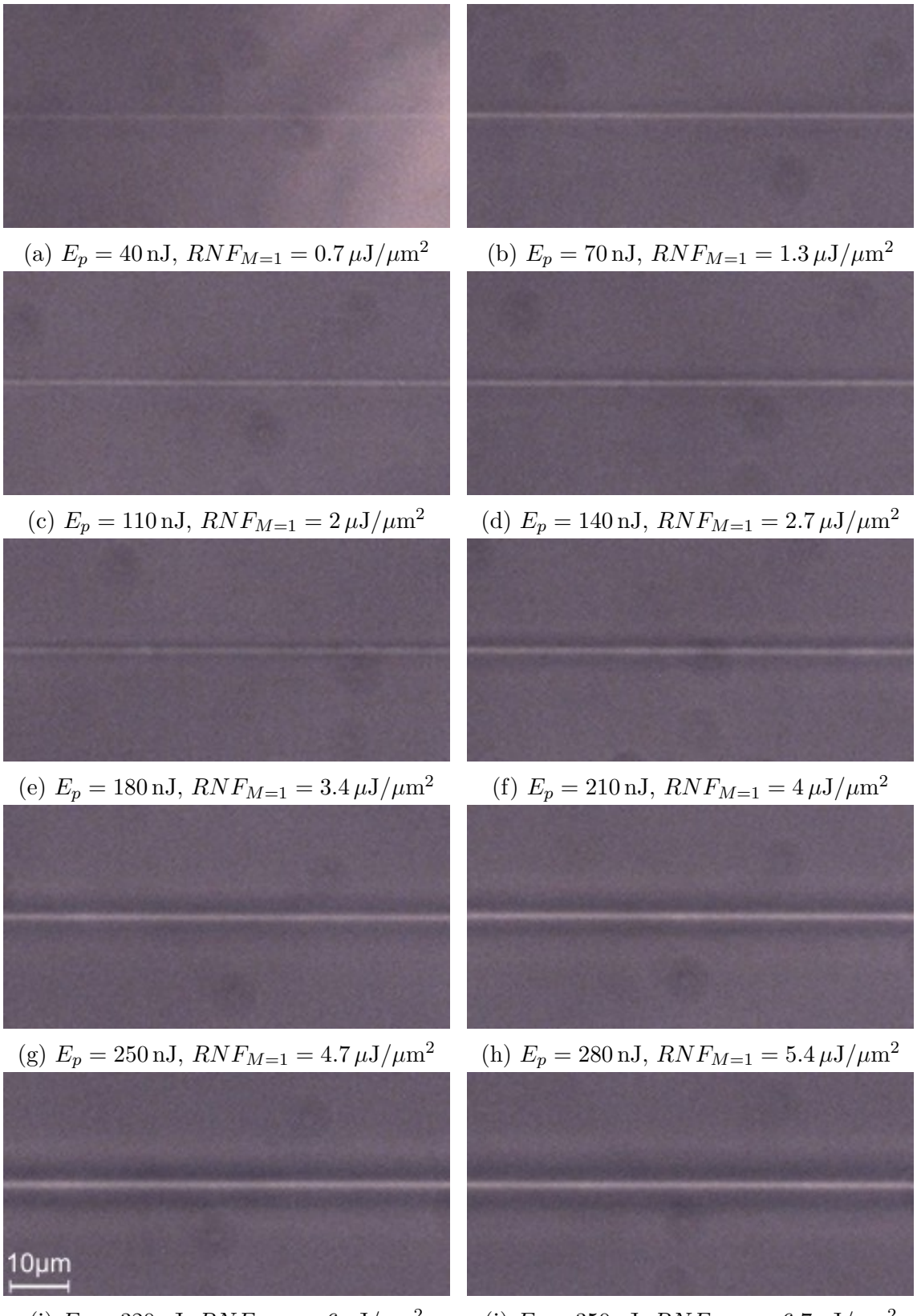

(a) $E_p = 40\,\mathrm{nJ}$, $RNF_{M=1} = 0.7\,\mu\mathrm{J}/\mu\mathrm{m}^2$

(b) $E_p = 70\,\mathrm{nJ}$, $RNF_{M=1} = 1.3\,\mu\mathrm{J}/\mu\mathrm{m}^2$

(c) $E_p = 110\,\mathrm{nJ}$, $RNF_{M=1} = 2\,\mu\mathrm{J}/\mu\mathrm{m}^2$

(d) $E_p = 140\,\mathrm{nJ}$, $RNF_{M=1} = 2.7\,\mu\mathrm{J}/\mu\mathrm{m}^2$

(e) $E_p = 180\,\mathrm{nJ}$, $RNF_{M=1} = 3.4\,\mu\mathrm{J}/\mu\mathrm{m}^2$

(f) $E_p = 210\,\mathrm{nJ}$, $RNF_{M=1} = 4\,\mu\mathrm{J}/\mu\mathrm{m}^2$

(g) $E_p = 250\,\mathrm{nJ}$, $RNF_{M=1} = 4.7\,\mu\mathrm{J}/\mu\mathrm{m}^2$

(h) $E_p = 280\,\mathrm{nJ}$, $RNF_{M=1} = 5.4\,\mu\mathrm{J}/\mu\mathrm{m}^2$

(i) $E_p = 320\,\mathrm{nJ}$, $RNF_{M=1} = 6\,\mu\mathrm{J}/\mu\mathrm{m}^2$

(j) $E_p = 350\,\mathrm{nJ}$, $RNF_{M=1} = 6.7\,\mu\mathrm{J}/\mu\mathrm{m}^2$

Figure 70: Top view. All structures were written with the writing speed $v_s = 50\,\mathrm{mm/s}$ and number of scans $M = 1$ resulting into $N_p^{v_s \neq 0} = 7$ number of pulses per area, while the pulse energy E_p was varied.

Acknowledgements and Thanks

This work is part of "NAIR-APREXIS", funded by the Deutsche Forschungsgemeinschaft (grant no. 506421303), part of this work was completed during an Erasmus+ funded internship. The research leading to these results has received funding from the European Union's Horizon 2020 research and innovation programme under Grant Agreement 101004719 (ORP).

A big thank you to everyone who supported me:

Prof. Kurt Busch: For your support and guidance as my supervisor and for having such a great and welcoming group.

Aline N. Dinkelaker: For your guidance, feedback, and unwavering support. I am incredibly grateful to have you as my supervisor, as a mentor and as an inspiring female role model in science.

Kalaga Madhav, Martin Roth & the Astrophotonics group at AIP: For all the support you gave me and for making the work at AIP so enjoyable.

Sonja Sautter: For being always kind and your incredible support regarding the huge amount of paper work.

Kévin Barjot: For your amazing feedback and your great Paris recommendations.

Alexandre Mermillod-Blondin: For collaborating with us on ULI, suggesting phase contrast microscopy and answering all our questions.

CHARA group: *Gail Schaefer*, for enabling this great opportunity; *Nic Scott*, for always helping me; *Karolina Kubiak*, for supporting me with the alignment, your feedback, and for the nice hikes with you and *Rainer Köhler*; *Victor Castillo*, for your brilliant solutions; *Norm Vargas* and *Becky Flores* for letting me shadow your operations and our enjoyable conversations. I am truly grateful for the opportunity to work with and learn from all of you.

NAIR-2 / APREXIS team: For your valuable feedback and overall help.

Julian J. Rypalla: For being my friend and such a great coworker, and for your helpful feedback.

Julien (Eve) Kluge: For always helping me, and for providing valuable feedback that never fails to make me laugh. Most importantly, thank you for being part of my life, and for all the adventures we share together.

Thank you to all of my friends — I could not be happier to have every single one of you in my life! And finally, thank you to my family, especially my parents, my brothers and my nieces and nephews for always being there for me.
Danke für alles!

Humboldt-Universität zu Berlin
Faculty of Mathematics and Natural Sciences
Department of Physics

Surname	Mayer
First name	Alyssa Valerie

Declaration of authorship

I hereby declare that my master thesis with the title

> *CHara ARray Integrated Optics Testbench (CHARIOT) for ultra-fast laser written astrophotonic beam combiners*

is the result of my own work which has been written only with the help of the indicated sources.

I especially confirm that without any exception, I have fully cited all sources referring to direct quotations of other authors' statements or tables, graphs, quotations as well as all indirect quotations or modified tables, graphics and citations from the internet.
This thesis, in same or similar form, has not been submitted to any other institution.

Berlin, 30th September 2024

Alyssa Valerie Mayer